Computational Modelling Studies on Discharge Products of Advanced Lithium-Sulphur Batteries.

By

Mallang Cliffton Masedi

THESIS

Submitted in fulfilment of the requirements for the degree of

Doctor of Philosophy (PhD)

in

Physics

in the

Faculty of Science and Agriculture,

(School of Physical and Mineral Sciences)

at the

UNIVERSITY OF LIMPOPO

SUPERVISOR: Prof. P.E. NGOEPE

Co-SUPERVISOR: Dr. H.M. SITHOLE

2018

Declaration

I declare that the thesis hereby submitted to the University of Limpopo (Turfloop Campus) for the degree of Doctor of Philosophy (PhD) has not been previously submitted by me for a degree at this or any other university; that this is my work in design and in execution, and that all material contained herein has been duly acknowledged.

---------- ----------

Masedi M.C. **Date:**

Abstract

Beyond conventional intercalation chemistry, reaction of lithium with sulphur and oxygen (so-called “Li-air” batteries) have the potential to provide 2 to 5 times the energy density of current Li-ion battery systems. However, both Li/S and Li/O_2 systems suffer from cycling performance issues that impede their commercial applications: Li/O_2 cycling is limited by electrolyte decomposition and large cell polarization; Li/S suffers from the low conductivity of S and the solubility of intermediary polysulfide species during cycling. It has been reported that Se and mixed Se_xS_y represent an attractive new class of cathode materials with promising electrochemical performance in reactions with both Li and Na ions. Notably, unlike existing Li/S batteries that only operate at high temperature, these new Se and Li/Se_xS_y electrodes are capable of room temperature cycling.

Initially, stabilities of insoluble discharge products of oxygen and sulphur in the Li-S and $Li\text{-}O_2$ batteries were investigated using density functional theory within the generalized gradient approximation, and these were deduced from their structural, electronic and mechanical properties. The structural properties are well reproduced and agree to within 3% with the available experimental data. Li_2S, Li_2O and Li_2O_2 and Li_2S_2 structures all have negative heats of formations indicating that they are stable, however, that of Li_2S_2 structure was relatively high compared to others. Calculated phonon dispersion and elastic properties revealed that Li_2O, Li_2S and Li_2O_2 structures are mechanically stable and great agreement with experimental work. The Li_2S_2 structure displayed soft modes associated mainly with sulphur atoms vibrations in the a-b plane, hence it is not mechanically stable in agreement with the negative C_{13}. Stable

Li_2S_2 polymorphs were extracted from soft modes of calculated phonon dispersions along the gamma direction in the Brillioun zone.

Temperature is known to have a significant impact on the performance, safety, and cycle lifetime of lithium-ion batteries (LiB). In order to explore properties of discharge products associated with Li/S and Li/Se batteries at different temperatures, molecular dynamics and cluster expansion methods were employed. The former was achieved by firstly deriving empirical interatomic potentials of Li_2S and Li_2Se which were fitted to experimental and DFT calculated data. The potentials were validated against available experimental and calculated structure, elastic properties and phonon spectra. In addition, complex high temperature transformations and melting of Li_2S and Li_2Se were reproduced, as deduced from molecular dynamics simulations. Both Li_2S and Li_2Se were found to withstand high temperatures, up to 1250K each which is a desirable in future advanced battery technologies.

Furthermore, cluster expansion and Monte-Carlo simulations were employed to determine phase changes and high temperature properties of mixed Li_2S-Se. The former generated 42 new stable multi-component Li_2S-Se structures and ranked metastable structures by enthalpy of formation. Monte Carlo simulations produced thermodynamic properties of Li_2S-Se system for the entire range of Se concentrations obtained from cluster expansion and it demonstrated that Li_2S-Se is a phase separating system at 0K but changes to mixed system at approximately 350K which was confirmed by constructed by phase diagram of Li_2S-Se system. It was finally demonstrated that molecular dynamics and Monte Carlo simulations techniques yield consistent results on phase separation and high temperature behavior of Li_2S-Se at 50% of sulphur and selenium.

Acknowledgements

I would like to thank my supervisor, Professor P.E. Ngoepe and co-supervisor Doctor H.M Sithole, for the support, patience and guidance throughout this project. Thanks must also go to my colleagues at the Materials Modelling Centre (University of Limpopo), and some members of Center for High Performance Computing (CHPC) for the help and fruitful discussions during my visits. I would like to acknowledge the Council for Scientific and Industrial Research (CSIR) and National Research Foundation (South Africa) for their financial support. The Centre for High Performance Computing (CHPC) is acknowledged for the provision of computer resources.

Studying for PhD is not always easy. Many times the excitement of getting new encouraging results comes with many failed efforts. Hard work, dedication and persistence are not really enough. With stress, tiredness and sense of giving up taking its toll, it is important to get the support, encouragement and understanding. I was fortunate that my family and friends provided these in abundance. To all of them I am grateful. Finally, my wife *Thandeka*, son *Clinton* and daughter *Theola* who unknowingly allowed me to be away from them for extended periods and also their mom for taking care of them.

Dedications

Dedicated:

To my wife: *Thandeka*

My son and daughter: *Clinton and Theola*

My mother and father: *Johanna and Elias*

My 5 brothers:

Marcus

Emmanuel

Joel

Josias

Klaas

Table of contents

List of Figures

List of Tables

Chapter 1: Introduction

1.1. General Background

Lithium is the lightest element that is metallic under normal conditions and, together with its fellow alkali metals, has served for many decades as a model “nearly free electron” system. In addition, lithium metal finds application in the battery industry for the high energy density primary lithium batteries as well as in the pharmaceutical industry as a metal ion or reducing reagent. However, although lithium in its pure form is a soft, silver white metal, it tarnishes and oxidizes very rapidly in air and water. Furthermore, lithium reacts easily in water and does not occur freely in nature.

Lithium was discovered in the mineral petalite ($LiAl(Si_2O_5)_2$) by Johann August Arfvedson in 1817. It was first isolated by William Thomas Brande and Sir Humphrey Davy through the electrolysis of lithium oxide (Li_2O). Today, larger amounts of the metal are obtained through the electrolysis of lithium chloride (LiCl). Lithium is not found free in nature and makes up only 0.0007% of the earth's crust. Many uses have been found for lithium and its compounds.

Lithium has the highest specific heat of any solid element and is used in heat transfer applications. It is used to make special glasses and ceramics, including the Mount Palomar telescope's 200 inch mirror. Lithium is the lightest known metal and can be alloyed with aluminium, copper, manganese, and cadmium to make strong, lightweight metals for aircraft. Lithium hydroxide (LiOH) is used to remove carbon dioxide from the atmosphere of spacecraft. Lithium stearate ($LiC_{18}H_{35}O_2$) is used as a general

purpose and high temperature lubricant. Lithium carbonate (Li_2CO_3) is used as a drug to treat manic depression disorder.

Lithium is a highly interesting metal, in part due to the increasing interest in lithium-ion batteries. Several recent studies have used different methods to estimate whether the lithium production can meet an increasing demand, especially from the transport sector, where lithium-ion batteries are the most likely technology for electric cars. The reserve and resource estimates of lithium vary greatly between different studies and the question whether the annual production rates of lithium can meet a growing demand is seldom adequately explained [1].

1.2. Literature Review

Several studies have been conducted on discharge products formed in Li–S and Li–O_2 batteries and they have been predominantly experimental; computational work has been scarce. The following sections review some previous studies on discharge products formed in Li–S and Li–O_2 batteries, using computational work.

1.2.1. Rechargeable Li-S and Li-O Batteries

Energy storage will be more important in the future than at any time in the past. Among the myriad energy-storage technologies, lithium batteries will play an increasingly important role because of their high specific energy (energy per unit weight) and energy density (energy per unit volume). Since their introduction in 1991, Li-ion batteries have transformed portable electronic devices [2, 3, 4, 5]. New generations of such batteries will electrify transport and find use in stationary electricity storage [6]. However, even when fully developed, the highest energy storage that Li-ion batteries can deliver is too

low to meet the demands of key markets, such as transport, in the long term. Reaching beyond the horizon of Li-ion batteries is a formidable challenge; it requires the exploration of new chemistry, especially electrochemistry, and new materials [7] [1]. There are few options. Two, based on lithium, rechargeable Li–air (hereafter referred to as Li–O_2 as O_2 is the fuel) and Li–S batteries [8]. Other options, especially Zn–air, have been reviewed in detail recently elsewhere [9, 10, 11].

Although Li–O_2 and Li–S share the same anode, and have active cathode components (O_2 and S) that are nearest neighbours in group 16 of the periodic table, there are important differences related to the different chemistry of O and S and the different states of matter of their cathodes. Li–S has been investigated since the 1940s; the problems are formidable and extensive efforts have been made to address them over the intervening 70 years. Important advances have made recently, but significant challenges remain, [12, 13].In comparison, Li–O_2, especially with a non-aqueous electrolyte, has received much less attention until recently [14, 15]. As in the case of Li–S, major challenges will have to be solved if Li–O_2 batteries are to succeed. The renaissance of interest in Li–S and the upsurge of interest in Li–O_2, based on aqueous and non-aqueous electrolytes, reflects the need for electrochemical energy-storage devices that can offer a leap forward; for example, delivering electric vehicles with a driving range approaching the goal of ~500 km between charging. In the limited space available, we cannot hope to review all the excellent work that has taken place on these two battery technologies. Instead, we shall begin by considering the energy that can be stored in Li–O_2 and Li–S cells, and then examine each system, how it operates, and the challenges facing research that attempts to advance Li–O_2 and Li–S batteries.

The theoretical specific energies (gravimetric energy densities) for Li–S and Li–O_2 are given in Table 1, where they are compared with those for Li-ion and Zn–air. The values are based on the cell reactions in column 1, that is, the energy obtained per unit mass or per unit volume of the active components of the anode and cathode. Often a value around 1000 Wh kg−1 is quoted for the Li–O_2 cell; however this is based on the mass of Li alone. All metal–air cells gain mass (O_2) as they discharge, so the mass of O_2 should be included, as it is in Table 1. The leap forward in theoretical specific energy on migrating from Li-ion to Li–S and then Li–O_2 is clear. It arises because Li_2S, Li_2O_2 and LiOH in the cathode store more Li, and hence charge, than $LiCoO_2$ per unit mass, and Li metal stores more charge per unit mass than a graphite (C_6Li) anode. The theoretical energy density is also greater for Li–O_2 and Li–S than Li-ion.

The discovery of new electrode materials is key to realizing safe and efficient electrochemical energy storage systems essential to enabling future green energy technologies. Beyond conventional intercalation chemistry, reaction of lithium with sulphur and oxygen have the potential to provide 2 to 5 times the energy density of current commercial systems [16]. However, both Li/S and Li/O systems suffer from cycling performance issues that impede their commercial applications: Li/O cycling is limited by electrolyte decomposition and large cell polarization; Li/S suffers from the low conductivity of S and the solubility of intermediary polysulfide species during cycling [17].

Here we explore the potential of selenium, a d-electron containing member of group 16 with high electrical conductivity, as an electrode material for rechargeable batteries [18]. We show that Se and mixed SexSy [19] represent an attractive new class of cathode materials with promising electrochemical performance in reactions with Li ions

using cluster expansion and Monte Carlo simulation techniques. Much has not been done in literature on high temperature properties and phases generations of mixed Li/SSe system.

Table 1: Different Rechargeable batteries materials with their gravimetric energy densities and prices [20].

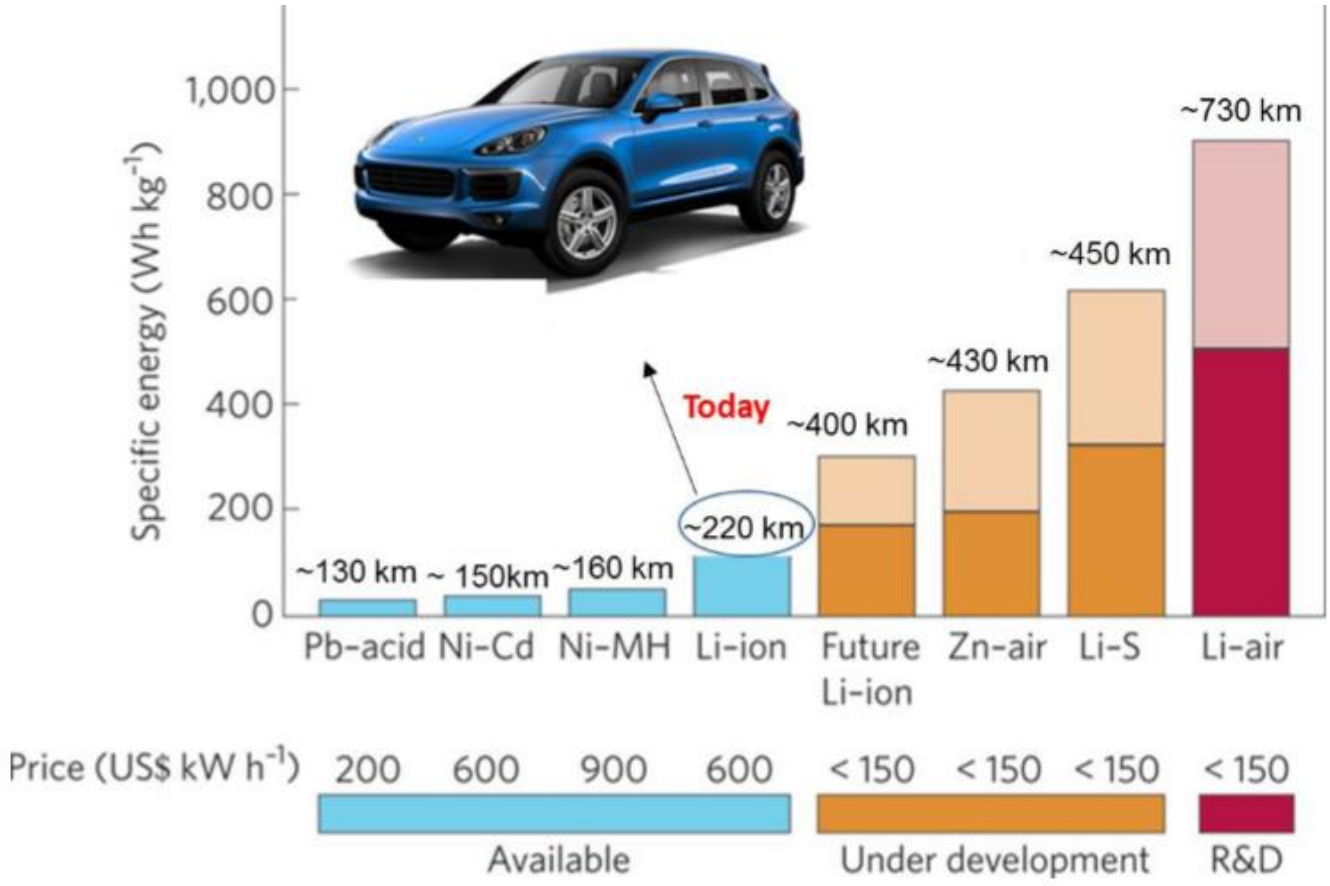

In this work we will firstly focus on the insoluble discharge products (i.e., Li_2O, Li_2S, Li_2O_2 and Li_2S_2) of oxygen and sulphur in Li–S and Li–O_2 batteries. The structural, electronic, mechanical and vibrational properties will be determined using *ab-initio* method. Cluster expansions will be employed to generated new phases of Li/SSe

system. Monte Carlo and molecular dynamics will be utilized to investigate the high temperature properties Li/SSe system.

1.3. Structural Properties

In figure.1 we show the crystal structures of Li_2S, Li_2O, Li_2O_2 and Li_2S_2. The crystal structures of Li_2S and Li_2O has the same space group Fm-3m (225), while Li_2O_2 and Li_2S_2 have the same space group of P_{63}/mmc (194). The crystal structures Li_2S, Li_2O and Li_2O_2 have been observed experimentally, but Li_2S_2 has not been reported experimentally. However, the structure was generated using the VASP code from Li_2O_2 by substituting the oxygen atom with sulphur atom, for the purpose of the study.

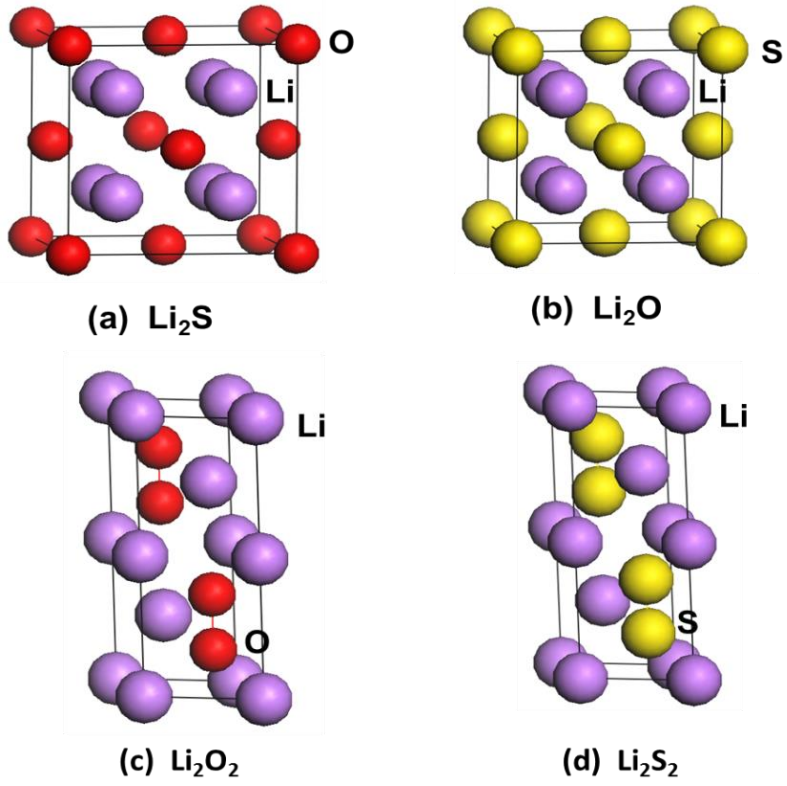

Figure 1: Crystal structures of (a) Li_2S, (b) Li_2O, (c) Li_2O_2 and (d) Li_2S_2, the red atom represent O, yellow atom is S and purple atom is Li.

Table 2: The lattice constant, symmetry, volume and density of Li_2S, Li_2O, Li_2O_2 and Li_2S_2

Crystal structures	Symmetry	Space group number	Lattice constants Å	Volume $Å^3$	Density Mg/m^3
Li_2S [21]	Fm-3m	225	a=b=c=5.72	187.15	1.631
Li_2O [22] [23]	Fm-3m	225	a=b=c=4.63	99.42	1.996
Li_2O_2 [24] [25]	P_{63}/mmc	194	a=b=3.16 c=7.69	66.67	2.285
Li_2S_2	P_{63}/mmc	194	a=b=4.13 c=10.52	155.50	1.666

Lithium peroxide, Li_2O_2, is a kind of lithium oxides whose structure was first suggested by *Féher et al.* [26] based on their X-ray diffraction data, and then *Föppl et al.* [27] also proposed their structure based on a systematic study of several alkali peroxides through their own X-ray diffraction data. Despite these two structures being both hexagonal with the space group of P6 their lattice constants are different. Moreover, due to the fact that lithium is a poor X-ray scatterer, the interpretation of X-ray diffraction data is not thoroughly suitable to lithium compounds. Therefore, Cota et al. [24] reinvestigated the structure of Li_2O_2 using density-functional theory, reported this structure as belonging to the space group (P_{63}/mmc) and the improved cell parameters (a= 3.1830 Å, c= 7.7258 Å). Nevertheless, no report of the physical properties such as thermodynamic properties of this compound about this structure exists, to our knowledge.

Lithium oxide (Li_2O) is one of the simplest ionic oxides. At ambient pressure it exists in the anti-fluorite structure with space group O_h^5 (*Fm*-3*m*), characterized by oxygen ions (O^{2-}) arranged in an fcc sub lattice with lithium ions (Li^+) in tetrahedral interstitial sites. In lithium oxide, Li ions are the diffusing species while oxygen ions constitute the rigid framework [22].

On the technological side there are many applications for Li_2O ranging from possibilities for hydrogen storage (in combination with Li_3N) and use as a blanket breeding material for thermonuclear reactors to convert energetic neutrons to usable heat and to breed the tritium necessary to sustain deuterium–tritium reactions [22]. Because of its high Li atomic density and high melting temperature, Li_2O has been considered as a potential candidate blanket breeding material for future thermal nuclear reactors and understanding the mechanical behaviour (elastic constants, bulk modulus etc.) of Li_2O for high temperatures and pressures is very useful for these applications [28].

Lithium sulphide (Li_2S) crystallizes in the face-centered cubic anti-fluorite structure with group O_h^5 (*Fm*-3*m*). The cations form a simple cubic Bravais lattice and the anions occupy the center of one in every two cubes. This structure is antimorphous to the fluorite structure and therefore some similarity of the chemical and physical properties is expected [29].

A most fascinating feature is the fact that both structures can undergo at high temperatures (but well below their melting point) a diffuse phase transition to a fast-ion-conducting region. This was first observed for the fluorite evidence that a similar transition does indeed occur also in anti-fluorite alkali sulphide compounds. Ionic conductivity experiments performed shows undoubtedly the presence of this transition

at around 1250 K in Li_2S [30]. Only recently, high-temperature experimental investigations and theoretical studies were performed on the compound Li_2S [31]. On the other hand, the practical capacity of a Li-O battery does not correspond to theoretical capacities of oxygen and Li metal owing to various reasons.

In the Li_2Se compounds, the metal atoms (Li) are located at (0.25; 0.25; 0.25) and (0.75; 0.75; 0.75) and the selenium atoms (Se) are located at (0; 0; 0). Unlike the oxide and sulphide compounds of this crystal family, the selenides of alkali metals have received less investigative attention from researchers towards their electronic and optical traits. Most of the research work for alkali metal selenides has been confined to studying the structural properties of these materials [32] [33] . However, no theoretical and experimental account of the electronic and optical properties of these materials was available in literature until recently when Eithiraj et al. [34] utilized the Tight-Binding Linear Muffin-Tin Orbitals (TB-LMTO) method to investigate ground-state and under compression electronic behaviour of selenides and tellurides of Li, Na and K.

1.4. Background on the Properties to be Investigated

ab initio calculations refer to an approach where properties of materials i.e. structural, electronic, optical, etc. can be determined using quantum mechanical methods. Some of the properties including heats of formation, elastic properties, phonon dispersions and the density of states will be reviewed below as they are appropriate for the current study.

1.4.1. Heats of Formation

It has become quite common place for electronic structural calculations, of varying rigor, to yield the total energy of a solid. This offers a prospect of estimating the stabilities of structures which are either unavailable or inaccessible experimentally. Heats of formation from *ab initio* calculations have been successfully used to predict the stability of discharge products formed in Li-S and Li-O_2 batteries.Previous X-ray diffraction studies by Chan et.al [25] of Li_2O_2 where the assessed higher energy diffraction in the process checking the heats of formation for the structure and Duan et.al [23] performed DFT calculations on Li_2O to check how stable the structure in using the heats of formations. In this work we will use the heats of formation to predict the stability of the Li_2S, Li_2O, Li_2O_2 and Li_2S_2 structures.

1.4.2. Elastic Constants

Elastic constants in materials science are any numbers that quantify the response of a material to elastic or springy deflection. When tensile stress is applied to a material, the resulting strain is determined by Young's modulus, a constant defined as the ratio of the stress in a body to the corresponding strain. *ab initio* calculations for the determination of elastic constants are more complex than the calculations of bulk properties (i.e. lattice constants, heats of formation, etc.). The application of strain on the lattice implies a lowering of symmetry from that of bulk crystal and the strain energy involved is small. Bertheville *et al.* [31] calculated the elastic constants of alkali metal sulphides Li_2S and Na_2S using *ab initio* methods. Mjwara *et al.* [35] performed an experimental study on Li_2S at high temperature elastic constants using brillouin scattering. P. Goel *et al.* [28] performed a lattice dynamics and molecular dynamics study on Li_2O to confirm that

the structure is mechanically stable. The problem of ductile versus brittle response of crystals requires the fracture strength in addition to their deformability. Pugh [36] introduced the quotient of bulk modulus to shear modulus, B/C' as an indication of the extent of fracture range in metals. A high value of B/G is associated with ductility and a low value with brittleness. In this study we note that the lowest heat of formation is associated with ductility whereas the highest value is associated with the brittleness of the structure. This stipulates the relationship between the heat of formations and the elastic constants in terms of stability.

1.4.3. Phonon Dispersions

In physics, a phonon is a quasiparticle representing the quantization of the modes of lattice vibrations of periodic, elastic crystal structures of solids. Phonons play a major role in many of the physical properties of solids, including a material's thermal and electrical conductivities. Thus, the study of phonons is an important part of solid state physics. In classical mechanics these are known as normal modes. These normal modes are important because any arbitrary lattice vibration can be considered as a superposition of these *elementary* vibrations (cf. Fourier analysis). While normal modes are wave-like phenomena in classical mechanics, they have particle-like properties in the wave–particle duality description of quantum mechanics. The phonon spectrum of a solid is important in evaluating physical quantities such as specific heat, thermal expansion coefficient and electron-phonon interactions [37]. With the advent of computational techniques, calculations of phonon frequencies within the local density approximation (LDA) became possible [38]. Palacios *et al* [39] also calculated the phonon dispersion of $Ti_xGa_nAs_m$ and $Ti_xGa_nP_m$ using the *ab initio* method.

The phonon spectra and effective charges of the group-IV semiconductors (Si and Ge diamond structure) and of the zinc-blende structure III-V semiconductors GaAs, GaSb, AlAs and AlSb were calculated by Giannozzi *et al.* [40]. Duan et.al [23] and P. Goel *et.al* [28] performed first principle calculation on phonon dispersion of Li_2O to confirm that all modes are nondegenerate at a gamma point.

1.4.4. Electronic Density of States

In solid-state and condensed matter physics, the density of states (DOS) of a system describes the number of states per interval of energy at each energy level that are available to be occupied by electrons. Unlike isolated systems, like atoms or molecules in gas phase, the density distributions are not discrete like a spectral density but continuous. A high DOS at a specific energy level means that there are many states available for occupation.

A DOS of zero means that no states can be occupied at that energy level. In general a DOS is an average over the space and time domains occupied by the system. Local variations, most often due to distortions of the original system, are often called local density of states (LDOS). If the DOS of an undisturbed system is zero, the LDOS can locally be non-zero due to the presence of a local potential.

Similarly the heats of formation, elastic constants and phonon dispersion, density of states (DOS) can be used to predict the stability of the structures. There is experimental evidence that links the electronic structure to the stability for a broad class metal sulphides [41] This can be observed where the Fermi level hits the pseudogap of the density of states plot. Rajagopalan and Sundareswari *et al* [42] calculated the density of states of rhodium based intermetallics and Ghosh *et al* [43] also did calculations of

density of states on the FePd and $FePd_3$ intermetallics the results were in good agreement with the experiment. Duan *et.al* [23] performed DFT calculations on Li_2O at high pressure with DOS spectra obtained and confirming that the structure is stable.

1.4.5. Cluster Expansion

Cluster expansion [44] is a method describing the energy (or a similar scalar property) of a system as a function of occupation variables for each lattice position. On such a lattice the atom configuration, that is the distribution of the atomic species (including vacancies), is varied and the energies of the resulting configurations are swiftly predicted. Cluster expansion technique has been used other material such as VN_2 [45] , FeCr [46], there is no study reported for Li_2S-Se structure in literature or theory.

1.4.6. Atomistic Simulations Potential Models

Deriving interatomic potentials or force fields is one of the main challenges when using the force fields methods. The derivation of model parameters is critical to any successful classical simulations [47]. There are a number of potential models in the literature for other materials, i.e. TiO_2 [48], FeS_2 [49], MnO_2 [50], but to the best of my knowledge, they are no reported interatomic potentials for the Li_2S and Li_2Se structures.

1.5. Rationale of the Study

Li-ion batteries have transformed portable electronics and will play a key role in the electrification of transport and grid applications. However, the highest energy storage possible for Li-ion batteries is insufficient for the long-term needs of society. Here we consider a study on rechargeable lithium−sulfur (Li−S) batteries which hold great potential for high-performance energy storage systems because they have a high

theoretical specific energy, low cost, and are eco-friendly. This work employs computational modelling methods to explore stability, structural and electronic properties of discharge products formed in the Li-S-Se (Li_2S, Li_2S_2 (checked against Li_2O and Li_2O_2) and Li_2Se) battery, especially Li_2S-Se, which has potential to offer higher theoretical specific energy and remedies the challenges that Li-S battery encounters.

Computational modelling methods, including *ab-initio* and atomistic simulation techniques, have shed valuable insights on a wide variety of materials. Such methods individually play unique roles along time and length scales of modelling. Although *ab-initio* methods tend to be more accurate, they are however, confined to smaller systems and currently do not address thermal properties of systems effectively. Atomistic simulations, on the other hand, are based on interatomic potentials that are not always transferable to other metal sulphides. They are, however, more appropriate for handling properties of bulk, surfaces and nanostructures consisting of a large number of atoms; and in addition, they enable high temperature studies. Atomistic simulations have not been carried out on Li_2S-Se structures before, since related interatomic potentials are not available. There is, consequently, a necessity for deriving such potentials for Li_2S-Se, validating them and using them to predict bulk and nanostructural properties at ambient and high temperatures.

Cluster expansion and Monte Carlo simulations will be utilized for the first time on Li_2S-Se to generate new stable phases of Li_2S-Se. Monte Carlo simulations will determine concentration and temperature ranges in which systems mix and undergo phase separation. Such features will be validated by high temperature molecular dynamics simulations on the $Li_2S_{0.5}Se_{0.5}$ system.

1.6. Objectives of the Study

In this thesis we investigate the stabilities of discharge products of oxygen and sulphur (Li_2S, Li_2O, Li_2O_2 and Li_2S_2 structures) using the first principles density functional theory (DFT).

Furthermore we determine the equilibrium lattice parameters and the heats of formation of all structures. The results are compared with the available experimental data in order to validate the methodologies employed in the current study. We will investigate the stability of the structures by comparing their heats of formation. It should be emphasised that the Li_2O and Li_2O_2, which are discharge products of lithium air batteries have been extensively studied. Li_2O has been included in the initial part of the study since it is isostructural to Li_2S and Li_2Se. In particular Li_2O_2 will give guidance on structures that can be adopted by Li_2S_2 since the structure of the latter has not been fully resolved.

A further objective of the study is to derive the interatomic potential model that can adequately describe structural and thermodynamic properties of the Li_2S-Se system. The bulk structural properties of Li_2S and Li_2Se will be calculated and compared with the available experimental and other data from literature, validating the newly derived potential model. We will employ molecular dynamics (MD) simulations, which will be used in conjunction with the derived interatomic potentials, to simulate Li_2S and Li_2Se and mixed Li_2S-Se system at various temperatures. A cluster expansion technique will generate new stable phases of Li_2S-Se system and Monte Carlo simulations will determine concentration and temperature ranges in which the systems mix

1.7. Outline of the Study

Chapter 1 contains the general background of the Li_2S, Li_2S_2, Li_2O_2, Li_2O structures. The major experimental and computational are reviewed. The structural aspects of the Li_2S, Li_2S_2, Li_2O_2, Li_2O structures are discussed in this chapter. The rationale and objectives of the study are also outlined. Chapter 2 discusses the theoretical aspects and methodology used throughout this work, in particular the computational techniques, such as energy minimisation, molecular dynamics and electronic structure methods.

In Chapters 3, 4 and 5 we outline the main results obtained in the present study. Chapter 3 discusses the ab initio results on Li_2S, Li_2S_2, Li_2O_2, Li_2O structures. Chapter 4, the derivation of the interatomic potential model of the Li_2S and Li_2Se and mixed Li_2S/Se systems are discussed, together with its validation. In addition the molecular dynamics of Li_2S and Li_2Se and mixed Li_2S/Se system. Chapter 5 cluster expansion and Monte Carlo results on phase stability. Chapter 6 provides details on the comparisons of techniques used in chapter 4 and chapter 5. Finally Chapter 7 we give summary of the main results presented in this thesis and several recommendations for future research are also listed.

Chapter 2: Theoretical Studies and Computational Methods

2.1. Introduction

We will be using computer simulation techniques which offers an alternative way of investigating properties of materials (using computers), whereby the simulator builds a model of a real system and explores its behaviour. The mathematical model is physically based with the exploration being done on a computer. In many ways these simulation studies share the same mentality as experimental investigations. However, in a simulation there is absolute control and access to detail and given enough computer power, exact answers for the model. The commonly known computational technique is based on *ab initio* method.

ab initio is a group of methods in which properties of materials i.e. the values of the fundamental constants and the atomic numbers of the atoms present can be calculated using Schrödinger equation. These methods include density functional theory (DFT), Hartree-Fock (HF) methods and post-Hartree-Fock (PHF) methods. In the current study, we will only focus on the density functional theory for predicting the ground-state energy of many-body system.

Several factors have contributed to the present success of *ab initio* calculations for real materials systems. The first is the availability of modern high speed computers. This has made it possible to carry out calculations on real materials in interesting situations with sufficient accuracy that there can be meaningful detailed comparison with

experimental measurements. The second is the advent of density functional theory (DFT) and continuing development of approximations to the DFT formalism for electron exchange and correlation. The third is the refinement in band structure calculation techniques and the invention of the *ab initio* pseudopotentials [51], which have led to rapid computation of total energies. The density functional method has made it feasible to calculate the ground state energy and charge density with remarkably accurate results for real solids. This is the starting point for almost all current first-principle calculations of total energies of solids. Finally, there have been significant new developments in experimental techniques and materials preparation that are making it possible to probe the structure of matter in ways which were never realized before. One advance is the ability to create high pressures and explore the properties of matter over a wide range of densities [52]. This is an ideal experimental tool to provide information that can be compared directly with current theoretical calculations.

Computational methods are now a central technique in solid state science [43]. The field has changed qualitatively in recent years with the focus moving from reproduction (and illumination) of experimental data to detailed predictive calculations on highly complex systems. The methodology used in this thesis is computational, and in this chapter we will introduce electronic structure and atomistic simulation approaches. Energy minimisation and molecular dynamics techniques applicable in both approaches will be introduced. Levy [53] and Wimmer [54] also mentioned that for the past decades, computational materials science has made major strides in becoming a predictive; impacting fundamental science as well as the development programs of industrial materials.

2.2. Density Functional Theory

Density functional theory (DFT) was formulated by Hohenberg and Kohn [55] Sham in the 1960's to provide the foundation for accurate calculations. In DFT, the total electron density is decomposed into one-electron densities,

$$E = E[\rho] \tag{2-1}$$

which are constructed from one-electron wavefunctions.

The idea of using the electron density as the fundamental entity of a quantum mechanical theory of matter originates in the early days of quantum mechanics in the 1920's, especially by the work of Thomas [56] and Fermi [56]. However, in the subsequent decades, it was rather the Hartree-Fock approach [57], which was developed and applied to small molecular systems. Calculations on realistic solid state systems were then out of reach. In 1951, Slater [58] used ideas from the electron gas with the intention to simplify Hartree-Fock theory to a point where electronic structure calculations on solids became feasible. Slater's work, which led to the so-called $X\alpha$ method, has contributed tremendously to the development of electronic structure calculations. In solid-state systems, molecules and atoms, the electron density is a scalar function defined at each point *r* in real space,

$$\rho = \rho(\mathrm{r}). \tag{2-2}$$

The electron density and the total energy depend on the type and arrangements of the atomic nuclei. Therefore, one can write

$$E = E[\rho(r), \{R_\alpha\}] \tag{2-3}$$

where the set $\{R_\alpha\}$ denotes the positions of all atoms, α, in the system under consideration. Equation (2-3) is the key to the atomic-scale understanding of electronic,

structural and dynamic properties of matter. If one has a way of evaluating expression (2-3), one can, for example, predict the equilibrium structure of solid, one can predict the reconstruction of surfaces and the equilibrium geometry of molecules adsorbed on surfaces. Furthermore, the derivative of the total energy (2-3) with respect to the nuclear position of an atom gives the force acting on that atom. This enables the efficient search for stable structures and, perhaps more importantly, the study of dynamical processes such as diffusion or the reaction of molecules on surfaces. Most of the considerations discussed here are based on the Born-Oppenheimer approximation in which it is assumed that the motions of the electrons are infinitely faster than those of the nuclei. In practice this means that the electronic structure is calculated for a fixed atomic arrangement and the atoms are then moved according to classical mechanics. This is a fairly good approximation for heavy atoms like tungsten (W), but may cause errors for light atoms such as hydrogen (H) or lithium (Li).

In density functional theory, the total energy (2-1) is decomposed into three contributions, a kinetic energy and a Coulomb energy due to classical electrostatic interactions among all charged particles in the system and a term called the exchange-correlation energy that captures all many-body interactions,

$$E = T_0 + U + E_{xc}. \tag{2-4}$$

The most straightforward term is the Coulomb energy *U*. It is purely classical and contains the electrostatic energy arising from the Coulomb attraction between electrons and nuclei, the repulsion between all electronic charges and the repulsion between nuclei

$$U = U_{en} + U_{ee} + U_{nn} \quad , \tag{2-5}$$

With

$$U_{en} = -e^2 \sum_{\alpha} Z_{\alpha} \int \frac{\rho(r)}{|r - R_{\alpha}|} dr \quad , \tag{2-6}$$

$$U_{ee} = e^2 \iint \frac{\rho(r)\rho(r')}{|r - r'|} dr dr' \quad , \tag{2-7}$$

$$U_{nn} = e^2 \sum_{\alpha\alpha'} \frac{Z_{\alpha} Z_{\alpha'}}{|R_{\alpha} - R_{\alpha'}|} \quad , \tag{2-8}$$

where e is the elementary charge of a proton and Z_{α} is the atomic number of atom α. The summations extend over all atoms and the integrations over all space. Once the electron density and the atomic numbers and positions of all atoms are known, expression (2-6) to (2-8) can be evaluated by using the techniques of classical electrostatics.

The kinetic energy term, T_0, is more subtle. In density functional theory, the "real" electrons of a system are replaced by "effective" electrons with the same charge, mass and density distribution. However, effective electrons move as independent particles in an effective potential, whereas the motion of a "real" electron is correlated with those of all other electrons. T_0 is the sum of the kinetic energies of all effective electrons moving as independent particles. Often, one does not explicitly make this distinction between real and effective electrons.

If each effective electron is described by a single particle wave function, ψ_i, then the kinetic energy of all effective electrons in the system is given by

$$T_0 = \sum n_i \int \psi_i^*(r) \left[-\frac{\hbar^2}{2m} \nabla^2 \right] \psi_i(r) dr \quad . \tag{2-9}$$

Expression (9) is the sum of the expectation values of one-particle kinetic energies; n_i denotes the number of electrons in state *i*. By construction, dynamical correlations between the electrons are excluded from T_0.

The third term of Eq. (2-5), called exchange-correlation energy, E_{xc}, includes all remaining complicated electronic contributions to the total energy. The Hohenberg-Kohn-Sham theorem, which is a central part of density functional theory, states that the total energy is at its minimum value for the ground state density and that the total energy is stationary with respect to first-order variations in the density, i.e.

$$\left.\frac{\partial E[\rho]}{\partial \rho}\right|_{\rho=\rho_0} = 0 \qquad . \tag{2-10}$$

In conjunction with the kinetic energy, we have introduced one-particle wave functions $\psi_i(r)$, which generate the electron density

$$\rho(r) = \sum_i n_i |\psi_i(r)|^2 \tag{2-11}$$

where n_i denotes the occupation number of the eigenstate *i*, which is represented by the one-particle wave function ψ_i. By construction, $\rho(r)$ in Eq. (2-11) is the exact many-electron density.

The goal of the next step is the derivation of equations that can be used for practical density functional calculations. The variational condition (2-10) can be used to derive the conditions for the one-particle wavefunctions that lead to the ground state density. To this end, one substitutes Eq. (2-11) in expression (2-10) and varies the total energy with respect to each wave function. This procedure leads to the following equations:

$$\left[-\frac{\hbar^2}{2m}\nabla^2 + V_{eff}(r)\right]\psi_i(r) = \varepsilon_i\psi_i(r) \quad , \tag{2-12a}$$

with

$$V_{eff}(r) = V_C(r) + \mu_{xc}[\rho(r)] \quad . \tag{2-12b}$$

Equations (2-12) are called the Kohn-Sham equations. The electron density, which corresponds to these wavefunctions, is the ground state density which minimizes the total energy.

As a consequence of the partitioning of the total energy (2-4), the Hamiltonian operator in the Kohn-Sham equations (2-12) contains three terms, one for the kinetic energy, the second for the Coulomb potential and the third for the exchange-correlation potential.

The kinetic energy term is the standard second-order differential operator of one-particle Schrödinger equations and its construction does not require specific knowledge of a system. In contrast, the Coulomb potential operator, $V_C(r)$ and the exchange-correlation potential operator, μ_{xc}, depend on the specific electron distribution in the system under consideration.

The Coulomb or electrostatic potential $V_C(r)$ at point r is generated from the electric charges of all nuclei and electrons in the system. It can be evaluated directly in a real space,

$$V_C(r) = -e^2\sum_\alpha \frac{Z_\alpha}{|r - R_\alpha|} + e^2\int \frac{\rho(r')}{|r - r'|}dr' \quad . \tag{2-13}$$

In condensed systems it is more convenient to use Poisson's equation

$$\nabla^2 V_C(r) = -4\pi e^2 q(r) \tag{2-14}$$

to calculate the electrostatic potential. Here, $q(r)$ denotes both the electronic charge distribution $\rho(r)$ and the positive point charges of the nuclei at positions R_α.

The exchange-correlation potential is related to the exchange-correlation energy by

$$\mu_{xc}(r) = \frac{\partial E_{xc}[\rho(r)]}{\partial \rho(r)} \tag{2-15}$$

Equation (2-15) is formally exact in the sense that it does not contain any approximations to the complete many-body interactions.

Therefore, from the above discussions, the Kohn-Sham total energy functional can be expressed as

$$E = \frac{1}{2}\sum_{occ}\varepsilon_i + U_{nn} - \frac{e^2}{2}\iint \frac{\rho(r)\rho(r')}{|r-r'|}drdr' + E_{xc}[\rho(r)] - \int \rho(r)\mu_{xc}dr$$

In practice however, the exchange-correlation energy (and thus the exchange-correlation potential) is not known and one has to make approximations which will be discussed in the next section.

2.3. Approximation Methods

2.3.1. Local Density Approximation

Several different schemes have been developed for obtaining approximate forms for the functional; for the exchange-correlation energy. The simplest accurate approximation, for non-magnetic systems is to assume that the exchange-correlation energy is dependent only on the local electron density d(r) around each volume element. Local density approximation (LDA) gives the correct sum rule for the exchange correlation hole [59].

In the local density approximation given by

$$E_{xc}[\rho] \approx \int \rho(r)\varepsilon_{xc}^{0}[\rho(r)]dr \qquad (2\text{-}16)$$

the exchange-correlation energy is taken from the known results of the many-electron interactions in an electron system of constant density (homogeneous electron gas). The LDA amounts to the following picture: at each point in a molecule or solid there exists a well-defined electron density; it is assumed that an electron at such a point experiences the same many-body response by the surrounding electrons as if the density of these surrounding electrons had the same value throughout the entire space as at the point of the reference electron. The exchange-correlation energy of the total molecule or solid is then the integral over the contributions from each volume element.

A large number of total energy calculations have shown that the LDA gives interatomic bond lengths within ±0.05 Å of experiment or better for a great variety of solids, surfaces and molecules. However, the following systematic trends are found: (i) most lattice parameters predicted with LDA are too short (figure 2.1), (ii) weak bonds are noticeably too short, for example the Ni-C bond in the Ni carbonyl $Ni(CO)_4$, the bond between two magnesium atoms (which are closed shell systems) and the length of hydrogen bonds such as that in the water dimmer H-O-H---OH_2; (iii) the binding energies calculated with the LDA are typically too large, sometimes by as much as 50% in strongly bound systems and even more in weakly bound materials .Comparison with experiment shows that the LDA predicts densities, which are mostly too high (bond distances are too short) while the GGA improves the agreement with experiment.

2.3.2. Generalized Gradient Approximation

Gradient-corrected density functionals as suggested by Perdew [60], Becke [61], Perdew and Wang [62] and Perdew, Burke and Ernzerhof [63] offer a remedy to the

LDA discussed above. The basic idea in these schemes is the inclusion of terms in the exchange-correlation expressions that depend on the gradient of the electron density and not only on its value at each point in space. Therefore, these corrections are also sometimes referred to as "non-local" potentials. As example, Table 3 gives the form suggested by Becke (1988) for the exchange part and Perdew (1986) for the correlation. Energies are given in Hartree atomic units; the units for the electron and spin densities are number of electrons / (Bohr radius)^3. The constant b in Becke's formula is a parameter fitted to the exchange energy of inert gases. The explicit form of the functions f and g in Perdew's expression for the correlation energy is given in the original paper by Perdew [63]. While dissociation energies calculated with these corrections rival in accuracy the best post-Hartree-Fock quantum chemistry methods, gradient corrected density functional calculations are computationally much less demanding and more general. Gradient corrected density functionals have been studied extensively for molecular systems, for example by Andzelm and Wimmer [64].The results are very encouraging and this

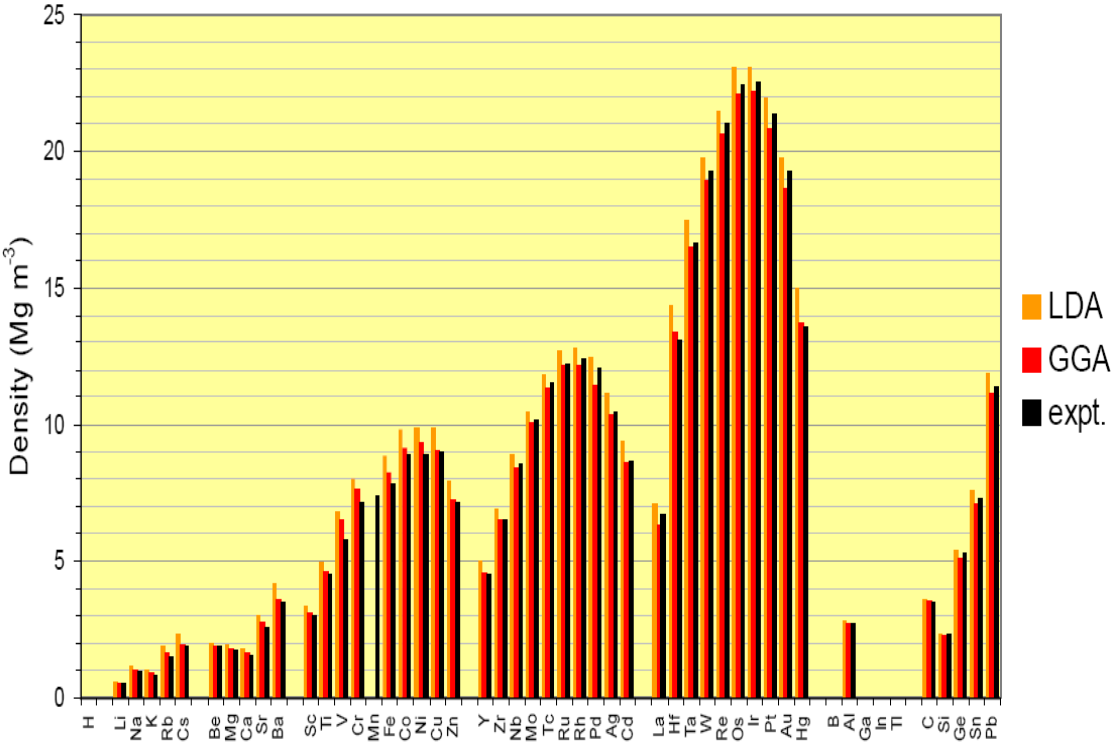

Figure 2: Density of selected elements computed with the local density approximation (LDA) and the generalized gradient approximation (GGA).

Table 3: Gradient-correction to the total energy for exchange by Becke and correlation by Perdew.

	$E_{GGA} = E_{LSD} + E_x^G + E_c^G$
Becke (1988) Gradient-corrected exchange	$E_x^G = b\sum_\sigma \int \frac{\rho_\sigma x^2{}_\sigma}{1+6bx_\sigma \sinh^{-1} x_\sigma} dr$ $x_\sigma = \frac{\lvert\nabla\rho\rvert}{\rho_\sigma{}^{4/3}} \qquad \sigma = \uparrow or \downarrow$
Perdew (1986) Gradient-corrected correction	$E_c^G = \int f\left(\rho_\uparrow, \rho_\downarrow\right) e^{-g(\rho)\lvert\nabla\rho\rvert} \lvert\nabla\rho\rvert^2 dr$

approach could turn out to be of great value in providing quantitative thermochemical data. The one-particle eigenvalues obtained from gradient-corrected exchange-correlation potentials are not significantly different from the LDA eigenvalues. Therefore, these potentials do not (and are not intended to) remove the discrepancy between calculated and measured energy band gaps. Figure 2 gives a comparison of LDA and GGA with experiments. The use of GGA has little influence on local properties and tends to overestimate the bond lengths and cell parameters, but does lead usually to a significant improvement in global changes in the total energy, such as those that result when two atoms combine to make a molecule. In this work, we used the PBE form of the GGA [60], which was designed to be more robust and accurate than the original GGA formulation [62]. The method used was employed because of its robustness for metallic systems.

2.4. Planewave Pseudopotential method

2.4.1. Planewaves and Pseudopotentials

Planewaves and pseudopotentials are hallmark of the method and they form a very natural alliance. They are so fundamental that their strength and weakness deserve special attention. In PW pseudopotential method, the model system is constructed in 3D periodic supercell which allows Bloch's theorem to be applied to the electron wavefunctions:

$$\psi_{n,k}(r) = u_{n,k}(r)\exp(ik.r) \tag{2-17}$$

The function $u(r)$ has the periodicity of supercell. It can be of any suitable mathematical form and usually one chooses a series expansion in terms of a set of basis

function. In PW pseudopotential, planewaves are used for this expansion, so that each single-electron wavefuntion $\psi_{n,k}$ is written as

$$\psi_{n,k}(r) = \sum u_{n,k}(G)\exp(i(k+G).r) \tag{2-18}$$

The $\mu_{n,k}$ are the expansion coefficients. The wavevectors G' are such that the planewaves are commensurate with the supercell. Both the number of G-vectors in the sum and the number of k's considered should in principle be infinite. The exponential term is a planewaves of wavevector k which must be commensurate with the entire system (i.e. not just the periodically-replicated cell). For an infinite system there is an infinite number of k vectors, at each of which solutions for $\psi_{n,k}$ exist. This simply reflects the fact that the number of electrons is infinite. However, a great simplification comes about when one realises that the change in $\psi_{n,k}$ with k becomes negligible for k-points that are close together. This means that one may calculate at a finite number of k-points. We speak of this idea as k-point sampling. The set of vectors $\{G\}$, on the other hand, should in principle be infinite to obtain an exact representation of the wavefunction. This is never necessary because summing over a finite number of G's will yield sufficient accuracy. Planewaves basis set has many advantages:

- It is unbiased, so all space is treated the same
- It is complete
- There is a single convergence criterion
- Planewaves are mathematically simple and their derivatives are products in k-space
- Planewaves do not depend on atomic positions

and its disadvantage is that (i) the number of planewaves needed is determined by the greatest curvature of the wavefunction and (ii) empty space has the same quality of representation and cost a regions of interest.

The advantages speak for themselves i.e the first three mean that one can always ensure that the basis set is adequate for a calculation by increasing the number of planewaves until the quantity of interest stops changing. In other words, the quality of the basis set depends on a single parameter, usually expressed as the energy of free electron whose wavefunction has the same wavevector as the largest wavevector in the planewave basis,

$$E_c = \frac{\hbar^2 (G+k)^2}{2m}. \tag{2-19}$$

All planewaves of 'energy' less than the cutoff energy E_c are used in the expansion. The mathematical simplicity of planewaves means the method is easier to implement, crucially so for the calculation of ionic forces which adds little complexity or cost to the calculation. Equally important in this context is the originless nature of planewaves. Their independence from atomic positions means that the forces do not depend on the basis set—there are no 'Pulay' or 'wavefunction' forces [65]. Even more important, new developments are easiest in planewave codes. An idea to calculate a property is most rapidly realised in a planewave basis and even if other methods catch up in time, the planewave approach remains as the reference. From a computational viewpoint the first of the disadvantages appears to be very serious.

2.4.2. Pseudopotential Approximation

The rapid oscillations of the wavefunctions near to the nucleus, due to the very strong potential in the region and the orthogonality condition between different states, mean that a very large cutoff energy and hence basis set, would be necessary. Fortunately, the study of Physics and Chemistry shows that the core electrons on different atoms are almost independent of the environment surrounding the atom and that only the valence electrons participate strongly in interactions between atoms. Thus, the core electron states may be assumed to be fixed and a pseudopotential may be constructed for each atomic species which takes into account the effects of the nucleus and core electrons [66].

The pseudopotential approximation allows the electronic wavefunctions to be expanded using a much smaller number of planewave basis states. It is well known that most physical properties of solids are dependent on the valence electrons to a much greater extent than on the core electrons. The pseudopotential approximation exploits this by removing the core electrons and replacing the strong ionic potential by a weaker pseudopotential that acts on a set of pseudo wavefunctions rather than the true valence wavefunctions. An ionic potential, valence wave function and corresponding pseudopotential and pseudo wave function are illustrated in figure 3. The valence wavefunctions oscillate rapidly in the region occupied by the core electrons due to the strong ionic potential in this region. These regions maintain the orthogonality between the core wavefunctions and the valence wavefunctions, which is required in the Pauli's exclusion principle.

The pseudopotential is constructed in such a way that its scattering properties or phase shifts for the pseudo wavefunctions are identical to the scattering properties of the ion

and the core electrons for the valence wavefunctions, but in such a way that the pseudo wavefunctions have no radial nodes in the core region. The phase shift produced by the ion core is different for each angular momentum component of the valence wave function and so the scattering from the pseudopotential must be angular momentum dependent. The most general form for pseudopotential is

$$V_{NL} = \sum_{lm} |lm\rangle V_l \langle lm| \tag{2-20}$$

Where $\langle lm|$ are the spherical harmonics and V_l is the pseudopotential for angular momentum l. Acting on the electronic wave function with this operator decomposes the wave function into the spherical harmonics, each of which is the multiplied by the relevant pseudopotential V_l.

A pseudopotential that uses the same potential for all the angular momentum components of the wave function is called a local pseudopotential. Pseudopotential is a function only of the distance from the nucleus. It is possible to produce arbitrary, predetermined phase shifts for each angular momentum state with a local potential, but there are limits to the amount that the phase shifts can be adjusted for the different angular momentum states, while maintaining the crucial smoothness and weakness of the pseudopotential. Without a smooth, weak pseudopotential it becomes difficult to expand the wavefunctions using a reasonable number of planewaves basis states.

2.5. K-Sampling

Electronic states are allowed only at a set of k-points determined by the boundary conditions that apply to the bulk solid. The density of allowed k-points is proportional to the volume of the solid. The infinite numbers of electrons in the solid are accounted

for by an infinite number of k-points and only a finite number of electronic states are occupied at each k-point.

The Bloch theorem changes the problem of calculating an infinite number of electronic wavefunctions to one of calculating a finite number of k-points. The occupied states at each k-point contribute to the electronic potential in the bulk solid so that in principle an infinite number of calculations are needed to compute this potential. However the electronic wavefunctions at k-points that are very close are identical. Hence it is possible to represent the electronic wavefunctions over a region of k space by the wavefunctions at the single k-point. In this case the electronic states at only a finite number of k-points are required to calculate the electronic potential and hence determine the total energy of the solid.

Methods have been devised for obtaining very accurate approximations to the electronic potential from a filled electronic band by calculating the electronic wavefunctions at special sets of *k*-points. The two most common methods are those of Chadi and Cohen [67] and Monkhorst and Pack [68]. Using these methods, the electronic potential and the total energy of an insulator can be obtained by calculating the electronic states at a very small number of k-points. A denser set of k-points are required to calculate the electronic potential and the total energy of a metallic system in order to define the Fermi surface precisely.

However, the computational cost of performing a very dense sampling of k space increase linearly with the number of k-points in the Brillouin zone (BZ). Density functional codes approximate these k space integrals with a finite sampling of k-points. Special k-points schemes have been developed to use the fewest possible k-points for

a given accuracy, thereby reducing the computational cost. The most commonly used scheme is that of Monkhorst and Pack [68].

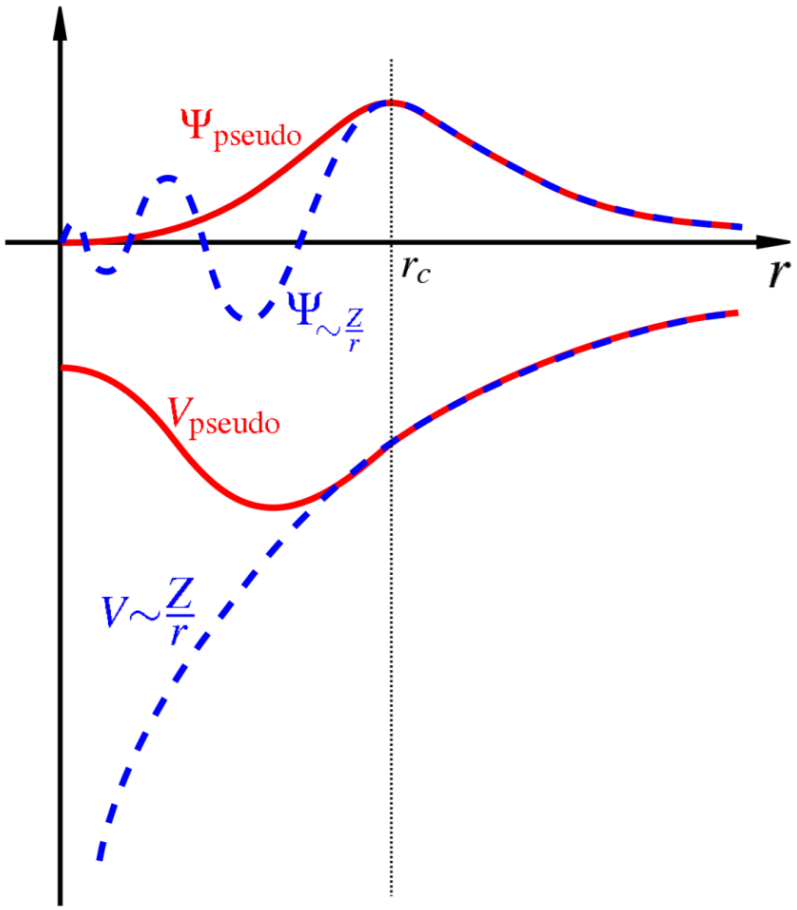

Figure 3: Comparison of a wavefunction in the Coulomb potential of the nucleus (blue) to the one in the pseudopotential (red). The real and the pseudowavefunction and potentials match above a certain cutoff radius rc.

2.6. Planewave Pseudopotential Code VASP

In this thesis we have employed one planewave pseudopotential code i.e. VASP [69]. In section 2.6.1 below we give a brief explanation of the code. The VASP code has been used to determine the equilibrium lattice parameters, the heats of formation, the elastic constants and the phonon dispersions for the Li_2S, Li_2O, Li_2O_2 and Li_2S_2

structure. We have also calculated the density of states using VASP and will present all the results calculated in chapter 3 and 4.

2.6.1. VASP Code

Vienna Ab-initio Simulation Package (VASP) is a package for performing ab-initio quantum-mechanical molecular dynamics (MD) using pseudopotentials and a planewaves basis set. The approach VASP is based on a finite-temperature local-density approximation (with the free energy as variational quantity) and an exact evaluation of the instantaneous electronic ground state at each MD-step using efficient matrix diagonalization schemes and efficient Pulay mixing. These techniques avoid all problems occurring in the original Car-Parrinello method which is based on simultaneous integration of electronic and ionic equations of motion. The interaction between ions and electrons is described using ultrasoft Vanderbilt pseudopotentials (US-PP) or the projector augmented wave method (PAW) [70]. Both techniques allow a considerable reduction of the necessary number of planewaves per atom for transition metals and first row elements. Forces and stresses can be easily calculated with VASP and used to relax atoms into their instantaneous ground state.

The projector-Augmented wave implemented in VASP reconstructs the full all-electron density and avoids the necessity of nonlinear core-corrections. VASP use efficient matrix diagonalisation schemes and an efficient Pulay/Broyden charge density mixing, these techniques avoid all problems occurring in the original Car- Parinello method, which is based on the simultaneous integration of electronic and ionic equations of motion.

2.7. Heats of Formation

For the study of the discharge products of sulphur and oxygen formed in Li-S and Li-O_2 batteries, it is convenient to consider the heats of formation which is calculated as follows:

$$\Delta H_f = E_c - \sum_i x_i E_i \tag{2-21}$$

where E_c is the calculated total energy of the compound, E_i is the calculated total energy of element i in the compound. The equilibrium total energies of the discharge products of sulphur and oxygen formed in Li-S and Li-O_2 batteries are calculated using VASP. The lower the heat of formation of the structures, the more stable they become.

2.8. Elastic Properties

2.8.1. Theory of Elasticity

From the perspective of materials physics, the elastic constants C_{ij} contain some of the more important information that can be obtained from ground-state total-energy calculations. A given crystal structure cannot exist in a stable or metastable phase unless its elastic constants obey certain relationships. The C_{ij} also determines the response of the crystal to external forces, as characterized by the bulk modulus, shear modulus, Young's modulus and Poisson's ratio and so play an important role in determining the strength of a material [71].

First-principles calculations that use periodic boundary conditions assume the existence of a single crystal, so all elastic constants can be determined by direct computation. The calculated C_{ij} can then be used to check the experimental bulk and shear moduli, if

available and to calibrate model calculations. In addition, the elastic constants can be used to check the phase stability of proposed compounds [72]. First-principles calculations can thus be used to predict the existence and properties of new materials.

2.8.2. Definition of Elastic Constants

To determine the elastic constants of a crystal, a deformation of the unit cell is created by changing the Bravais lattice vectors **R = (a, b, c)** of the undisturbed unit cell to **R′ = (a', b', c')** using a strain matrix **e**

$$R' = R.\begin{pmatrix} 1+e_{xx} & \frac{1}{2}e_{xy} & \frac{1}{2}e_{xz} \\ \frac{1}{2}e_{yx} & 1+e_{yy} & \frac{1}{2}e_{yz} \\ \frac{1}{2}e_{zx} & \frac{1}{2}e_{zy} & 1+e_{zz} \end{pmatrix}. \qquad (2\text{-}22)$$

The deformation leads to a change of the total energy of the crystal

$$U = \frac{E_{tot} - E_0}{V_0} = \frac{1}{2}\sum_{i=1}^{6}\sum_{j=1}^{6} C_{ij} e_i e_j \ , \qquad (2\text{-}33)$$

where E_0 is the total energy of the unstrained lattice, V_0 is the volume of the undistorted cell and the C_{ij} are the elements of the elastic constant matrix with a notation that follows standard convention. Both *i* and *j* run from 1…6 in the sequence {xx, yy, zz, yz, xz, xy}. The tensor of elasticity has 36 elements, the elastic constants, but maximally 21 of these are independent.

2.8.3. Calculation of Elastic Constants

The simplest case by far is the cubic system where there are only three independent constants, C_{11}, C_{12} and C_{44}. We use this case to illustrate the manner in which the stiffness matrix elements may be determined from strain fields of the form (2-22). If the applied strain is exx = e with all other ei equal to zero, the energy change is $U = C_{11}e^2/2$. This allows a unique determination of C_{11}. If $e_{yz} = e_{zy} = e/2$, with all other strain components zero, then $U = C_{44}e^2/2$ and we have an independent determination of C_{44}. The bulk modulus, B, is the response to a uniform compression so applying the strain field $e_{xx} = e_{yy} = e_{zz} = e$ allows the computation of B via the relation $U = Be^2/2$. Similarly, the shear modulus can be calculated by using the strain field $e_{zz} = e; e_{xx} = e_{yy} = -e/2$, whereupon $U = 3C'e^2/2$. Finally, the off-diagonal stiffness matrix element C_{12} can be calculated using one or other of the relations

$$B = \frac{1}{2}(C_{11} + 2C_{12}) \qquad (2\text{-}24)$$

$$C' = \frac{1}{2}(C_{11} - C_{12}) \qquad (2\text{-}25)$$

Using both of these relations provides a useful independent check on the accuracy of the computation. A symmetry-general formulation of the calculation of elastic constants from total energy calculations is given by Le Page and Saxe [73].

2.8.4 Elastic Constant Stability Conditions

The accurate calculation of elasticity is essential for gaining an insight into the mechanical stability and elastic properties of solids. For the cubic, tetragonal and

orthorhombic crystals, the are three (C_{11}, C_{12}, C_{44}), six (C_{11}, C_{12}, C_{13}, C_{33}, C_{44}, C_{66}) and thirteen (C_{11}, C_{22}, C_{33}, C_{12}, C_{13}, C_{23}, C_{44}, C_{55}, C_{66}, C_{15}, C_{25}, C_{35}, C_{46}) independent elastic constants. Applying two kinds of strains (ε_1 and ε_4) can give stresses relating to these three elastic coefficients, yielding an efficient method for obtaining elastic constants for the cubic system. This method has been successfully used to study the elastic properties of a range of materials including metallic systems [71]. The mechanical stability criteria of cubic systems as outlined elsewhere [74] are given as follows:

$$C_{44} > 0, C_{11} > |C_{12}| \quad \text{and} \quad C_{11} + 2C_{12} > 0, \tag{2.8.4.1}$$

where C_{11}, C_{12} and C_{44} are the only three independent elastic constants. Based on three independent single crystal elastic constants of a cubic crystal, C_{11}, C_{12}, C_{44}, the elastic moduli are determined using the following expressions:

$$B = \left(\frac{C_{11} + 2C_{12}}{3} \right), \; C' = \frac{C_{11} - C_{12}}{2}, \; A = \frac{(2C_{44} + C_{12})}{C_{11}}, \tag{2.8.4.2}$$

where B is the bulk modulus, C' tetragonal shear modulus and anisotropic factor A. It is acknowledged that the bulk modulus B is a measure of resistance to volume changed by applied pressure, whereas the elastic anisotropy A has an important implication in engineering science since it is highly correlated with the possibility of inducing micro-cracks in materials [74]. If the material is completely isotropic, the value of A will be 1, while values smaller or larger than 1 measure the degree of elastic anisotropy. The positive C' indicates the mechanical stability of the crystal, otherwise unstable.

The corresponding mechanical stability criterion for hexagonal crystal reads as

$$C_{11}>0,\ C_{11}-C_{12}>0,\ C_{44}>0, C_{11}-C_{12})-C_{33}-2C_{13}^2>0 \tag{2.8.4.3}$$

We calculated the elastic constants of Li_2O, Li_2S, Li_2O_2 and Li_2S_2 structures, as compiled in Table 2. All the elastic constants and shear moduli of the four structures,

Li_2O, Li_2S, Li_2O_2 and Li_2S_2, are positive, thus satisfying mechanical stability criteria set in equations (2) and (4). For a cubic material, it is well known that B, C' and C_{44} must be positive for a structure to remain mechanically stable. More importantly, we note a good agreement in our predicted heats of formation and the elastic constants, consistent with phase stability trend.

2.9. Phonons Calculations

A detailed knowledge of lattice vibrations is critical for the understanding and quantitative prediction of a wide variety of physical properties of solids. The fundamental thermodynamic functions of internal and free energy, entropy, heat capacity as well as non-linear properties such as thermal expansion and heat conduction are to a considerable extent determined by the vibrations of the constituent atoms in the lattice. Fortunately, the quantum theory of lattice dynamics is well developed and has proven to be one of the most successful theories of solid state physics.

With the advent of density functional theory and the progress with numerical methods for solving quantum physical equations together with the emergence of more and more powerful computers made it feasible to accurately describe the interatomic interactions in crystals and molecules based on quantum mechanics. Three different techniques for *ab initio* evaluation of vibrational properties have been developed, namely (i) direct methods based on total energy changes or forces calculated for atoms displaced from their equilibrium position, (ii) analytical calculation of force constants based on a perturbative expansion around the equilibrium geometry and (iii) Fourier transform of the atomic velocity autocorrelation function obtained from a molecular dynamics trajectory [75]. Direct methods (option (i) above) require the evaluation of total energy

and forces for the equilibrium geometry as well as of several distorted geometries from which the force constant matrix can be assembled. Phonon dispersion curves along specific high symmetry directions in reciprocal space were determined by the method of interplanar force constants [76], where planes perpendicular to these directions are displaced within an elongated supercell. The most general direct approach to lattice dynamics is based on the *ab initio* evaluation of forces on all atoms produced by a set of finite displacements of a few atoms within an otherwise perfect crystal. The perfect crystal environment has to be sufficiently large to ensure that interactions of the perturbation with all its translational symmetry equivalent copies are small, which usually requires construction of suitable supercells. The techniques for selecting suitable supercells and atomic displacements, assembling force constant matrices from the calculated forces and calculating phonon dispersion relations via Fourier transform are well documented [77].

2.9.1. Phonon Dispersion and Polarization Vectors

The frequencies $\omega^2(k, j)$ of phonon modes *j* are calculated by diagonalization of the supercell dynamical matrix for each wave vector k along a specified path through the Brillouin zone, thus creating phonon dispersion curves.

$$D(k) \cdot e(k, j)\omega^2(k, j)e(k, j) \tag{2-26}$$

The irreducible representations of all phonon modes at the Γ(0,0,0) point can be calculated, providing in addition Raman and infrared activities of the modes. The complex polarization vectors satisfy the orthonormality relations

$$\sum_j e_i^*(k, j; \mu) \cdot e_l(k, j; v) = \delta_{i,l}\delta_{\mu,v} \tag{2-27a}$$

$$\sum_i \sum_\mu e_i^*(k, j; \mu) \cdot e_i(k, j; \mu) = \delta_{i,j} \qquad \text{(2-27b)}$$

The polarization vectors $e(k,j;\mu)$ defined for the wave vector k centered at the origin of reciprocal space differ from the conventional polarization vector $e(k_\tau,j;\mu)$ as defined for the wave vector kτ pointing from the center of a given Brillouin zone labeled by the reciprocal vector τ. Because of $k = \tau + k_\tau$ the relation between these differently defined polarization vectors is

$$e(k, j; \mu) = e(k, j; \mu) \exp[-2\pi\tau \cdot r_\mu] \qquad \text{(2-28)}$$

Using the polarization vectors, the displacements caused by a particular phonon and its intensity can be calculated. Assuming amplitude Qk and phase $0 \le \varphi_k \le 1$ of the displacement wave, the displacements $U(n,\mu)$ of atoms (n,μ) for a given wave vector k and phonon branch j are given by the equation

$$U(n, \mu) = \frac{Q_k}{2\sqrt{M_\mu}} \{\mathrm{Re}\, e(k, j; \mu) \cos[2\pi(k \cdot R(n, \mu) - \phi_k)] - \mathrm{Im}\, e(k, j; \mu) \sin[2\pi(k \cdot R(n, \mu) - \phi_k)]\}$$

(2-29)

The intensity of phonon modes is obtained from the form factors. The form factor projected on the wave vector is defined as

$$F^{(p)}(k, j) = \frac{1}{k^2} \left| \sum_\mu \frac{k \cdot e(k, j; \mu)}{\sqrt{M_\mu}} \right|^2 . \qquad \text{(2-30)}$$

However, the intensity of a phonon mode is represented by the simple form factors

$$F^{(s)}(k, j) = \frac{1}{k^2} \left| \sum_\mu \frac{e(k, j; \mu)}{\sqrt{M_\mu}} \right|^2 \qquad \text{(2-31)}$$

which may be applied to remove unessential phonon branches originating from back folding, or to estimate relative intensities of all modes in varying Brillouin zones.

The MedeA-Phonon module is based on the general direct approach to lattice dynamics and is designed to work independent of a specific underlying code for deriving forces and total energies. However, together with the VASP a fully automatic and highly parallel procedure is provided within MedeA.

2.9.2 Phonon Dispersion Stability Conditions

When analysing the phonon dispersion curves, structures are said to be stable if and only if there are no soft modes in the negative frequency observed in the phonon dispersion curve.

2.10. Density of States

The density of states (DOS) is a useful mathematical concept allowing integration with respect to the electron energy to be used instead of the integration over the Brillouin zone. In addition, the DOS is often used for quick visual analysis of the electronic structure. Characteristics such as the width of the valence band, the energy gap in insulators and the number and intensity of the main features are helpful in qualitatively interpreting experimental spectroscopic data. DOS analysis can also help to understand the changes in electronic structure caused by, for example, external pressure.

More accurate methods are based on linear or quadratic interpolations of band energies between the reference points in the Brillouin zone. The most popular and reliable technique, which is based on the tetrahedron interpolation, is unfortunately ill suited to the Monkhorst-Pack grid of special points. Therefore VASP uses a simplified linear

interpolation scheme [78]. This method is based on the linear interpolation in parallelepipeds formed by the points of the Monkhorst-Pack set, followed by the histogram sampling of the resultant set of band energies.

The density of states behaviour at E_f is significant and can be used to correlate their stability. It is also known from literature that the DOS of structures of the same composition can be used to mimic the stability trend with respect to their behaviour at the E_f. The structure with the highest and lowest density of density at E_f is considered the least and most stable, respectively. Furthermore we can determine whether our structures are metal, semi-conductors or insulators by measuring their band gaps respectively.

2.11. Atomistic Simulation

One of the major reasons for computations in materials science is to gain a deeper understanding of materials on the atomic scale [79]. Atomistic computer modelling techniques now play a major role in both physical and biological sciences [80]. An atomistic simulation is now able to model the structure of mineral surfaces at the atomic level and is a valuable tool for interpreting and predicting surface structures [81]. The atomistic simulations are based on the Born model of ionic solids [82], in which the ions interact *via* long-range electrostatic forces and short-range forces. The value of atomistic simulations in the earth and materials sciences lies in demonstrating the mechanisms of atomistic procedures, and extending this capability to evaluate material properties to regimes where direct laboratory measurements are difficult or impossible to perform [83]. Atomistic models are limited to small system sizes. The major disadvantage is their inability to explicitly model electronic properties. This problem is

overcome by the use of electronic structure calculation density functional theory (DFT). The advantage of atomistic simulation is the reduction in computing time; we are able to model bigger system for a short period of time as compared to DFT. Energy minimization allows us to evaluate the most stable configurations and molecular dynamics provides the effect of temperature on the system. These techniques are discussed in the following sections.

2.11.1. Energy Minimisation

Energy minimisation allows us to evaluate energy of a system by adjusting the atom positions until a minimum energy configuration of the atoms is obtained. In this work we used energy minimisation throughout to calculate the energies and equilibrium structures of the bulk Li_2S and Li_2Se. As an example METADISE (minimum energy techniques applied to dislocations, interfaces, surface energies) codes [84], uses energy minimisation to calculate the structure of systems periodic in various dimensions (zero nanoparticles, one dislocations, two surfaces and three bulk). The advantage of energy minimisation is that (for systems it does not demand computationally, so it can be used to scan a range of possible configurations. The drawback of energy minimisation are that for large systems the inversion of the matrix of second order derivatives becomes prohibitively expensive, something which the ever increasing power of computers and techniques such as molecular dynamics go some way to negating and that it does not take account of the vibrational properties of the system. There is no representation of temperature in the simulated system however this effect will be small for ideal solid systems. The lowest energy configuration is found by using an iterative procedure to adjust the atom positions until the interaction energy is minimised. The calculated

interaction energy should be the minimum interaction energy of the system, i.e., the system must be at its mechanical equilibrium and there should be no residual stresses. However, this is rarely the case on setting up a simulation cell and hence the interaction energy needs to be minimized so as to remove these residual stresses. There are two ways of achieving this: Firstly, via a constant volume or constant area minimization, where the cell dimensions are kept fixed but the position of the ions can be modified. Secondly, by means of a constant pressure minimization where both the cell dimensions and the ions can relax, i.e., forces on the atoms and the cell dimensions are both removed [85]. The ions are at their minimised positions when all the forces are zero, i.e., when

$$\frac{\partial U}{\partial r} = 0 \qquad (2.1)$$

where U is the energy and r is the ion position.

The Newton-Raphson variable matrix method [86] has been employed for energy minimisation calculations throughout this work. This minimisation procedure optimises the energy of the systems modelled with the potential energy. In the Newton-Raphson method, $U(r)$ is expanded to second order by Taylor expansion:

$$U(r) = U(r_n) + g_n.\delta r^T + \frac{1}{2}\delta r^T.W_n.\delta r \qquad (2.2)$$

where δr is the displacement of a given ion

$$\delta r = r_{n+1} - r_n \qquad (2.3)$$

and W_n is the second derivative matrix,

$$W_n = -\frac{\partial^2 U}{\partial r_n^2} \qquad (2.4)$$

Then assuming equilibrium conditions where the change in energy with respect to ion positon is zero

$$\frac{\partial U}{\partial r} = 0 = g_n + W_n.\delta r \qquad (2.5)$$

which gives

$$\delta r = -W_n^{-1}.g_n \qquad (2.6)$$

Hence

$$r_{n+1} = r_n - .g_n.H_n \qquad (2.7)$$

where H_n is the Hessian matrix and is equivalent to W_n^{-1}. Therefore Equation 2.7 is the working equation for calculating the new atomic positions using the Newton-Raphson minimisation method. If the energy system was harmonic in r the minimum energy of the system would be obtained in a single step. However, the energy of the system is not harmonic, although the displacement gives rise to a lower energy configuration. Hence several iterations have to be performed before the equilibrium configuration is obtained. Since this method requires the calculation of both the first and the second derivative of energy with respect to the position of the ions and the inversion of the second derivative matrix, it can be computationally expensive for large systems. The speed of calculation can be increased if the inverted second derivative matrix is approximated and the matrix is recalculated after a fixed number of iterations or when the changes are in the energy are too large for the approximation to be valid [87]. There are a number of different ways that the inverse Hessian matrix can be approximated. The two methods that can be used to approximate are the Hessian matrix are shown below.

The Davidon-Fletcher-Powell (DFP) method [87]:

$$H_{n+1} \approx H_n + \frac{\delta r \times \delta r^T}{\delta r^T . \delta g} - \frac{(H_n . \delta g) \times (H_n . \delta g^T)}{\delta g^T . H_n . \delta g} \qquad (2.8)$$

where $\delta r = (r_{n+1} - r_n)$ and $\delta g = (g_{n+1} - g_n)$. The superscript corresponds to the transpose of the vector, and the new position $n+2$ can be calculated. The second method is the Broyden-Fletcher-Goldfarb-Shanno (BFGS) [88] [89]. This is a more efficient approach. This is identical to the DFP equation with only the additional term:

$$H_{n+1} \approx H_n + \frac{\delta r \times \delta r}{\delta r . \delta g} - \frac{(H_n . \delta g) \times (H_n . \delta g)}{\delta g . H_n . \delta g} + (\delta g . H_n . \delta g) u \times u \qquad (2.9)$$

where the vector u is defined as:

$$u = \frac{\delta r}{\delta r . \delta g} - \frac{H_n . \delta g}{\delta g . H_n \delta g} \qquad (2.10)$$

2.11.2. Molecular Dynamics

Molecular dynamics simulation is a computational technique used to study the motions of atoms in a given system (e.g., a solid material or a solid solution could equally be liquids and gases) in order to understand and predict the structural , dynamic, kinetic, and /or equilibrium properties at a chosen conditions (e.g., compositions, temperatures, and pressures) [90]. Molecular dynamics (MD) is a powerful method for exploring the structure of solids, liquids and gases. It is a modern method which requires electronic computers and recently supercomputers. Molecular Dynamics simulations are in many respects very similar to real experiments. When we perform a real experiment, we proceed as follows. We prepare a sample of the material that we wish to study. We connect this sample to a measuring instrument (e.g. a thermometer, manometer, or

viscometer), and we measure the property of interest during a certain time interval. If our measurements are subject to statistical noise (as most measurements are), then the longer we average, the more accurate our measurement becomes. In Molecular Dynamics simulation, we follow exactly the same approach. First, we prepare a sample: we select a model system consisting of N particles and we solve Newton's equations of motion for this system until the properties of the system no longer change with time (we equilibrate the system). After equilibration, we perform the actual measurement. In fact, some of the most common mistakes that can be made when performing a computer experiment are very similar to the mistakes that can be made in real experiments (e.g., the sample is not prepared correctly, the measurement is too short, the system undergoes an irreversible change during the experiment, or we do not measure what we think) [91]. We call molecular dynamics (MD) a computer simulation technique where the time evolution of a set of interacting atoms is followed by integrating their equations of motion. The molecular dynamics can be used to investigate the detailed atomistic mechanisms. With MD technique it is possible to simulate the dynamic, thermal behavior of atoms in solids. By performing simulations at different temperatures and studying the displacements of the ions as a function of time we can predict diffusion coefficients. The molecular dynamics technique involves solving Newton's laws of motion over a finite time period for all the particles of a system. The main difference with the energy minimization method discussed in the previous section, is that, molecular dynamics simulation gives the effect of temperature by assigning kinetic energy to the atoms in the simulation cell and thus allows us to follow the trajectory of the atoms and molecules with time. Hence, unlike in energy minimization calculations, atoms and molecules can potentially jump over energy barriers to reach a global

minimum; however, due to the very short 'real time' accessible to molecular dynamics simulations, this only applies to small energy barriers, i.e., of the order of few $k_B T$. All molecular dynamics simulations in this work were performed using the computer code DL_POLY developed by W. Smith and T.R. Forester in Daresbury, UK [92].

In molecular dynamics simulation, the particles are initially assigned random velocities, such that the system starts with the required temperature and that the simulation cell has no translational momentum, i.e.,

$$\sum_{i=1}^{N} m_i . v_i^2 = 3Nk_B T \qquad (2.11)$$

and

$$\sum_{i=1}^{N} m_i . v_i = 0 \qquad (2.12)$$

where N is the number of particles, k_B is the Boltzmann constant, T is the temperature, m_i is the mass of ion i_i, and v_i its velocity.

The second step of a molecular dynamics simulation is to calculate the force acting on each particle. Once the forces, F_i, are obtained the accelerations, a_i, can be calculated and the velocities, v_i, and positions F_i, are updated, for an infinitely small time step, according to

$$a_i(t) = \frac{F_i(t)}{m_i} \qquad (2.13)$$

$$v_i(t + \delta t) = v_i(t) + a_i(t).\delta t \qquad (2.14)$$

$$r_i(t + \delta t) = r_i(t) + v_i(t).\delta t \qquad (2.15)$$

These are the Newton's equations of motion and can only be applied strictly for an infinitesimal time step. In practice, computer codes use integration algorithms such as the Verlet algorithm [93] to solve Newton's laws of motion, as explained in the next section. The choice of the time step δt, in these equations is very important. Indeed if δt is too large, the molecular vibrations will occur within the time step, giving rise to large errors. However, if δt is too small, the particles will take too long to move a significant distance. In addition, another factor needs to be considered to choose the time factor. After each step, run time properties such as the potential energy, the temperature, or the pressure of the system are calculated. Then the process is repeated several thousand or million times to reach the required simulation time. In the first few tens of thousands steps, the particles' velocities are scaled to meet the desired temperature. This period is called the equilibrium period and it allows for the system to come to equilibrium at a given temperature and pressure before data are collected. Then, the simulation is run as long as possible, without scaling the particles' velocities, to obtain converged averages of the properties of interest and reduce statistical noise. In molecular dynamics we follow the laws of classical mechanics, and most notably Newton's law of motion:

$$\vec{F}_i = m_i \vec{a}_i \qquad (2.16)$$

for each atom *i* in a system constituted by *N* atoms. Here, m_i is the atom mass, $\vec{a}_i = \frac{d^2 \vec{r}_i}{dt^2}$ its acceleration, and $\vec{F}_i$ the force acting upon it, due to the interactions with other atoms.

In the next section we discuss the integration algorithm, the different types of ensembles used in this work and we will discuss the properties that are calculated from molecular dynamics simulations i.e. Radial distribution functions, diffusion coefficients and mean squared displacement.

Integration Algorithms

An integration algorithm is used to perform the step by step solution of the equations of motion using a finite difference algorithm. The algorithm used is this work is the Verlet algorithm [93]. The positions, velocities as well as accelerations are obtained by a Taylor expansion of the positions about time t:

$$\begin{aligned} r(t+\delta t) &= r(t) + v(t)\delta t + \frac{1}{2}a(t)\delta t^2 + \frac{1}{6}b(t)\delta t^3 + \ldots \\ v(t+\delta t) &= v(t) + a(t)\delta t + \frac{1}{2}b(t)\delta t^2 + \ldots \\ a(t+\delta t) &= a(t) + b(t)\delta t + \ldots \\ b(t+\delta t) &= b(t) + \ldots \end{aligned} \tag{2.17}$$

where r is the particle's position, **v** is the velocity, a is the acceleration and b is the third time derivative of r. From Equation (2.7) we can calculate the position of a particle about a position $r(t)$ before and after a time step δt

$$r(t+\delta t) = r(t) + v(t)\delta t + \frac{1}{2}a(t)\delta t^2 + \frac{1}{6}b(t)\delta t^3 + \vartheta(\delta t^4) \tag{2.18}$$

$$r(t-\delta t) = r(t) - v(t)\delta t + \frac{1}{2}a(t)\delta t^2 - \frac{1}{6}b(t)\delta t^3 + \vartheta(\delta t^4) \tag{2.19}$$

where $\delta(\delta t^4)$ is the order of accuracy. Now adding (2.8) and (2.9) gives

$$r(t+\delta t) + r(t-\delta t) = 2r(t) + a(t)\delta t^2 + \vartheta(\delta t^4) \tag{2.20}$$

We notice that Verlet algorithm [64] is time-reversible (i.e. $r(t+\delta t)$ and $r(t-\delta t)$ are interchangeable. Also, the absence of velocities, since they are not required but are necessary for the calculation of the kinetic energy. They can be calculated by subtracting Equation (2.9) from (2.8) and obtain:

$$v(t) = \frac{r(t+\delta t) - r(t-\delta t)}{2\delta t} + \vartheta(\delta t^2) \qquad (2.21)$$

Equation (2.20) is accurate to δt^4 while Equation (2.21) is accurate to order δt^2.

Ensembles

Statistical mechanics simulations are performed in different ensembles. The microcanonical or NVE ensemble, it's where the system is isolated from changes in particles (N), volume (V) and energy (E). A microcanonical molecular dynamics trajectory may be seen as an exchange of potential and kinetic energy, with total energy being conserved. The other ensemble is canonical or NVT ensemble, its where the number of particles, the volume and temperature are the constant quantities. And isothermal-isobaric or NPT ensemble, where the number of particles, pressure and temperature are the constant quantities. Initially a NPT simulation is performed on the bulk simulation cell (analogous to a constant pressure simulation in energy minimization) to remove any lattice strains. Thereafter, for example when considering surfaces, constant volume ensembles such as the NVT ensemble are used.

Molecular Dynamics Simulation Properties

The molecular dynamics studies result in various quantities describing the temperature-dependent behaviour of the analyzed systems. In our case we looked at the radial distribution functions (RDFs), mean squared displacement (MSD), and diffusion coefficient. These quantities provide the structural information about the solid and

liquid phases and about the melting phenomenon, meaning the temperatures of the solid-liquid transition can be estimated. However as stated by [94] the interpreted temperatures are not the real melting temperatures of the systems, but rather the temperatures of the mechanical instability of the infinite single crystal.

Radial Distribution Functions (RDFs)

The RDF is defined as the probability of finding an atom at a distance r from another atom compared to a homogeneous distribution [95] and is given by

$$g(r) = \frac{V}{N_1 N_2} \frac{1}{4\pi r^2 \delta r} \left\langle \sum_i \sum_{j>i} \delta\left(r - r_{ij}\right) \right\rangle \qquad (2.22)$$

where V is the volume, N_1 and N_2 are the atom types of the RDF. The delta function must give rise to a value of one for a range of $r(\delta r)$. The RDF tends to 1 at long distances with sharp peaks indicating a regular lattice structure. For amorphous or liquid systems the RDF shows characteristically a small number of broad peaks at short distance, indicating short range order, superimposed on an oscillating trace to 1, which indicates a loss of long range order [96]. The structural properties of our system were investigated by analysing the partial radial distribution functions (RDFs), $g_{CoS}(r)$, $g_{SS}(r)$. The partial RDFs $g_{\alpha\beta}(r)$ are defined in such a way that, by considering an atom of the species α, the probability of finding an atom of the species β in a spherical shell $(r, r+dr)$ is:

$$\rho_\beta 4\pi r^2 g_{\alpha\beta}(r) dr \qquad (2.23)$$

where $\rho_\beta = {}^{x_\beta}\!/_{V}$, is the number density of the species β with mole fraction x_β, and V is the volume per atom.

RDFs give the probability of finding the centre of a particle or atom at a given distance from the centre of another particle. We calculated the partial distribution functions obtaining the nearest neighbour interatomic distances of Li-Li, Li-S and S -S.

The light atom at the center is the reference atom, and the circles around it represent the other atoms. A ring centered on the reference is drawn with radius r and thickness dr. The radial distribution function can be an effective way of describing the structure of a system at different temperatures.

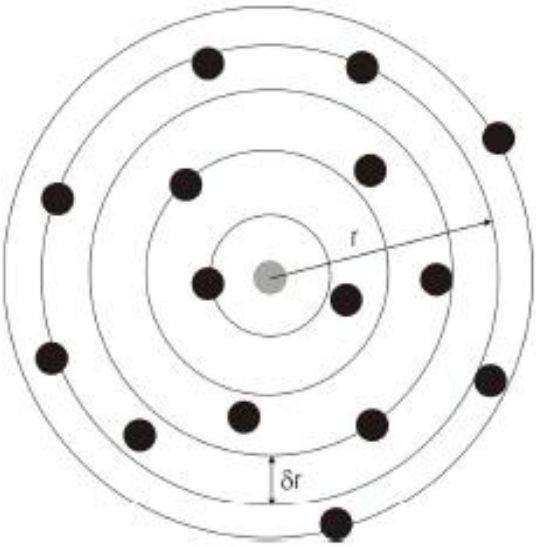

Figure 4: Schematic representation of the radial distribution function

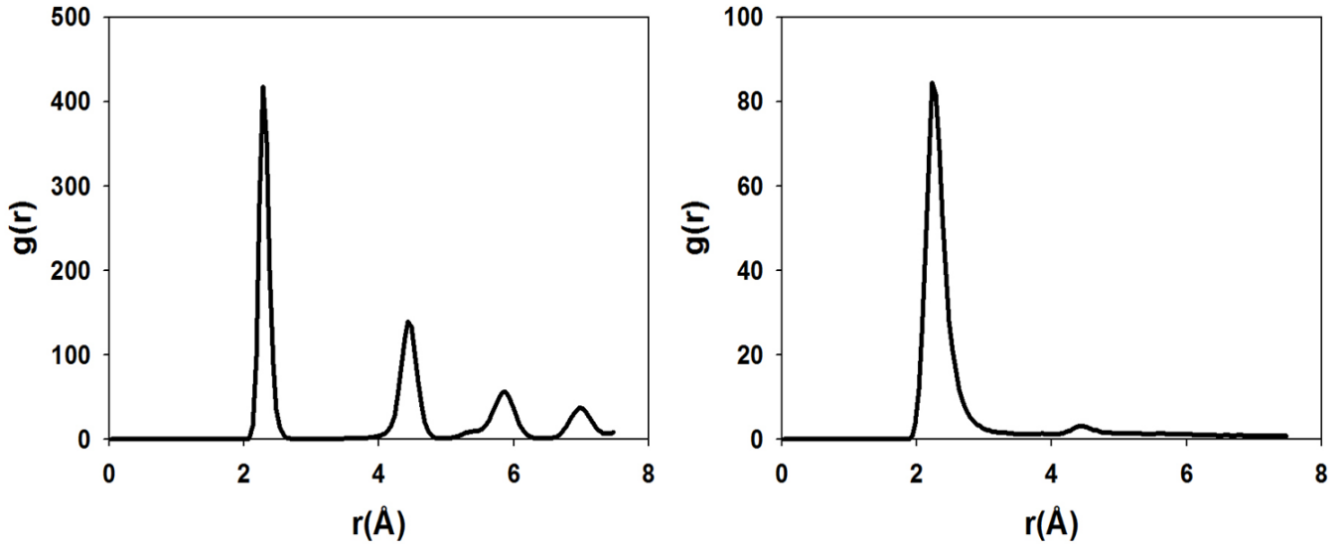

Figure 5: Example of a Cobalt-Sulphur RDF in a crystalline solid on the left and in a liquid phase on the right.

Differentiation between a solid and a liquid can be made using the rdfs by the number of peaks appearing in a particular RDF plot. In a crystal or solid, the radial distribution functions have a multiple number of sharp peaks and heights are characteristic of the lattice structure. The radial distribution function of a liquid has a small number of peaks at short distances and the height of the peaks decreases. The examples of cobalt-sulphur radial distribution functions are given in Figure 5. For the crystalline solid, the peaks are sharp and thin and show long-range order. In case of a liquid phase, the peaks are broad and the radial distribution function rapidly converges to one.

Mean Squared Displacement (MSD)

In this study, the behavior of the mean squared displacement (MSD) as a function of time is also used to discriminate between a solid and a liquid phase as suggested by [97]. The time dependence of the average mean squared displacement (MSD) is one of

the tools to obtain the information on the atom mobility. It is calculated according to the following relationship:

$$6Dt = <| r_i(t) - r_i(0) |^2 > \qquad (2.24)$$

In a solid (i.e. at a lower temperature), the diffusion will be significantly smaller and the MSD is flat. In a liquid (i.e. at a higher temperature), the particles diffuse randomly and the gradient of the curve is proportional to the diffusion coefficient. The curve takes a parabolic shape at the start, this is due to the short time it takes an atom to feel the effect of the other atoms. If there is no increase in the MSD of an ion type with time, then the ions are vibrating about their mean lattice site. Also as the MSD is the distance squared a vibrational will add to the function rather than cancel itself out. However such movements are small compared to atoms actually diffusing through the crystal. If the MSD's increases with time, then the ions are considered to be moving away from their initial positions.

Diffusion Coefficient

The diffusion is another measure to estimate relative mobilities of individual Li_2S and Li_2Se atoms. It is known that diffusion coefficient can be estimated from the slope of MSD plots using the Einstein relation as follows:

$$D = \frac{1}{6}\frac{d}{dt} <| r_i(t) - r_i(0) |> \qquad (2.25)$$

The integral Equation 2.25 is the velocity autocorrelation function (VAF), which is related to the diffusion coefficient. The VAF decays to zero at long time; the function is integrated mathematically to calculate the diffusion coefficient as in Equation 2.26.

$$D = \frac{1}{3}\int_0^\infty < v_i(t).v_i(0) > dt \qquad (2.26)$$

The melting point of the simulated system can be located by increasing the temperature of a crystalline system until diffusion appears.

Periodic Boundary Conditions

Periodic boundary conditions are used in most of our simulations of molecular dynamics (and energy minimization). Implementing periodic boundary conditions means that the particles are usually enclosed in a cubic simulation box of a fixed side-length. The box is then replicated to infinity by rigid translations in the three Cartesian directions, producing infinite images of each particle in the box. A particle in the box would not only interact with the rest of the particles in the same box, but with the images in the nearby boxes, provided that they lie within the range of interaction. When a particle leaves the simulation box, one image fills the void, shown in Figure 6.

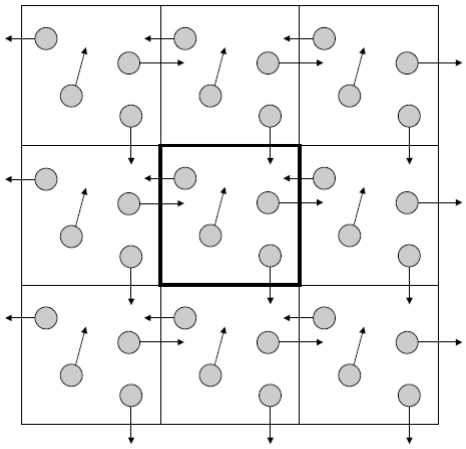

Figure 6: Schematic representation of the periodic boundary conditions where the simulation cell is highlighted in bold.

The highlighted cell in Figure 6 indicates the simulation cell whereas the other cells indicate the images. The system no longer has a surface, which is necessary to simulate bulk crystals or in the case of liquids to prevent outer molecules from boiling off into space. Two strategies can be employed when simulating surfaces. The first is to use two-dimensional periodic boundary conditions, that is where the cell is periodic in only two directions and the other direction is used to create the surface. This method uses the Parry summation which is described in the next chapter. The second is to use three-dimensional periodicity but have the simulation cell to be large so that the interactions between the interface and its images are negligible. This method use Ewald summation to model the electrostatic interactions.

Chapter 3: First Principle Calculations for Li_2S, Li_2O, Li_2O_2 and Li_2S_2 Structures: Structure and Stability

In this chapter we discuss the DFT results in particular the lattice constants and the heats of formations of the Li_2S, Li_2O, Li_2O_2 and Li_2S_2 structures. We further compare the obtained results with the available experimental and theoretical data. One code was used to perform calculations; namely VASP [98] as discussed in detail in chapter 2. In the next section we discuss the convergence parameters of the Li_2S, Li_2O, Li_2O_2 and Li_2S_2 structures. We also discuss the calculated bulk moduli and elastic constants of Li_2S, Li_2O, Li_2O_2 and Li_2S_2 structures. We will also present the phonon dispersion and the density of states results.

3.1. Cutoff Energy and K-points Convergence

3.1.1. Cutoff Energy

In order to determine the appropriate cutoff energy for our structures (Li_2S, Li_2O, Li_2O_2 and Li_2S_2 structures), single point energy calculations were performed for different kinetic energy cutoffs at default number of k-points for each system within GGA-PBE. The method was employed owing to its robustness for metallic systems. We used ultrasoft pseudopotentials [99], which require significantly less computational resources than the norm-conserving potentials. In figure 8 we show the curves of total energy per atom against cutoff energy for the Li_2S, Li_2O, Li_2O_2 and Li_2S_2 structures. The energy cutoffs of 500 eV was chosen for Li_2S, Li_2O, Li_2O_2 and Li_2S_2 structures,

respectively since the energy gave a constant slope at that point and they yielded energy differences of less than 1meV/atom. The curves are shown in figure 8.

3.1.2. K-Points

In this section, we show the convergence of the total energies with respect to the k-point sampling set size, as illustrated in figures 7. We have carried out total energy calculation at fixed cut-off energy for each structure (determined above) while the number of *k*-points was varied. The total energy with respect to the number of *k*-points was considered converged when the energy change per atom (between two consecutive points) was within 1meV per atom. The k-points were chosen as 8x8x8 for Li_2S, Li_2O, Li_2O_2 and Li_2S_2 structures, as shown in figures 7.

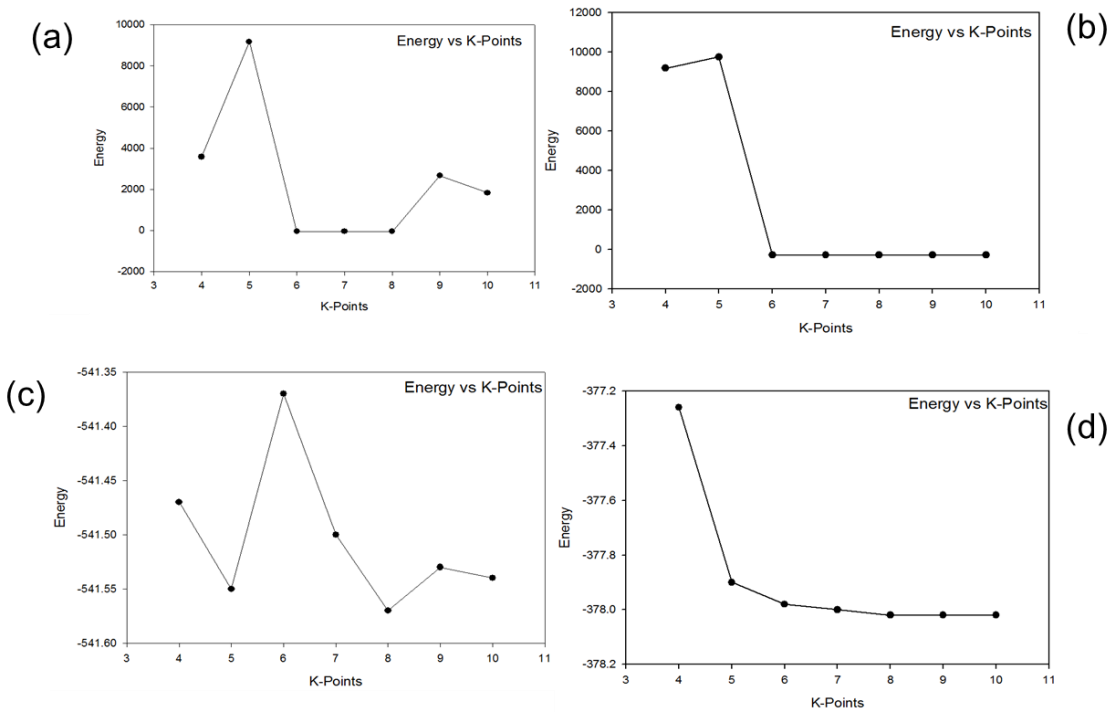

Figure 7 : Graphs of energy of formation vs the number of k-points for (a) Li_2O, (b) Li_2S, (c) Li_2O_2 and (d) Li_2S_2.

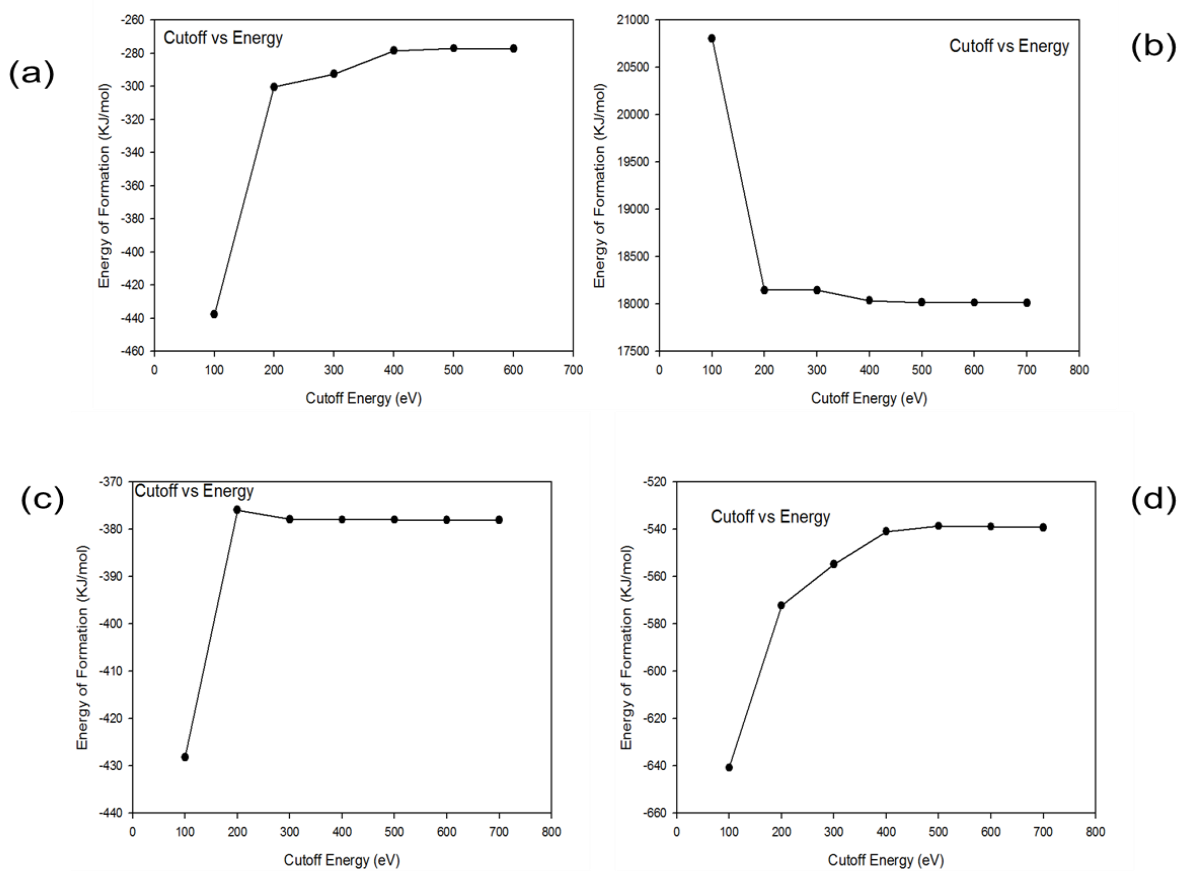

Figure 8: Graphs of energy of formation vs energy cut-off for (a) Li_2O, (b) Li_2S, (c) Li_2O_2 and (d) Li_2S_2.

3.2. Geometry Optimization

The geometry optimization for the Li_2S, Li_2O, Li_2O_2 and Li_2S_2 structure was performed within the generalized gradient approximation using the energy cutoff of 500eV. The lattice parameters of the structures were allowed to vary. The calculations were carried out till a good convergence was obtained. The total energy of the optimized structures was used to calculate the heats of formation which will be discussed in detail in the next section.

3.3. Heats of Formation for the Li_2S, Li_2O, Li_2O_2 and Li_2S_2 Structure

The calculations were performed at experimental lattice constant in the framework of DFT using VASP code. Table 4 summarizes the optimized lattice constants and heats of formation for studied systems together with those of previous studies, theoretical and experimental. Other studies employed different exchange correlation functional.

Our computed lattice parameters are in good agreement with the experimental and theoretical results. The GGA results are in good agreement with calculations such as linear combinations of atoms (LCAO), LMTO and full potential linearized augmented plane wave (FLAPW). We have calculated the equilibrium lattice constants and the heats of formations of the Li_2S, Li_2O, Li_2O_2 and Li_2S_2 structures. The calculations have predicted structures with negative heats of formations, Li_2S, Li_2O, Li_2O_2 and Li_2S_2 structures which are expected to be stable. Their heats of formation are almost of the same magnitude and the relaxed structures show no rotation. We observe that the cubic Li_2O has the most negative ΔH in good agreement with the experiments whereas Li_2S_2 is the least negative ΔH this can be due to the fact that the structure does not exist or the no much work done on it, the Li_2S_2 structure was built from existing Li_2O_2 structure by replacing oxygen atoms with sulphur atoms.

3.4. Competition Between Li_2S, Li_2O, Li_2O_2 and Li_2S_2

The heats of formation calculations reveal that Li_2S, Li_2O, Li_2O_2 and Li_2S_2 structures all have a negative ΔH. However, that of Li_2S_2 structure is closer to zero than the rest.

In summary, our predicted heats of formation results agree well with those found experimentally, in particular, the Li_2S and Li_2O structures which agrees to within 3% with the experimental values.

Table 4 : The equilibrium lattice parameters and heats of formation (ΔHf) of the Li_2S, Li_2O, Li_2O_2 and Li_2S_2 structure

Structure	Lattice Parameters (Å)		ΔH_f (KJ/mol)		Volume
	VASP	experimental	VASP	experimental	(Å^3)
Li_2O_2	a=3.16	3.18[27]	-277.16		66.57
	c=7.69	7.72[27]			
Li_2S_2	a= 4.13		-40.25		155.50
	c=10.52				
Li_2O	a=4.63	4.57 [28]	-541.57		99.42
Li_2S	a=5.72	5.71[29]	-378.02		187.15

3.5. Competition Between Li_2S, Li_2O, Li_2O_2 and Li_2S_2

The heats of formation calculations reveal that Li_2S, Li_2O, Li_2O_2 and Li_2S_2 structures all have a negative ΔH. However, that of Li_2S_2 structure is closer to zero than the rest.

In summary, our predicted heats of formation results agree well with those found experimentally, in particular, the Li_2S and Li_2O structures which agrees to within 3% with the experimental values.

3.6. Elastic Properties

We investigated the elastic constants and moduli of Li_2S, Li_2O, Li_2O_2 and Li_2S_2 structures within density functional theory in the framework of GGA. The planewave

cut-off energy was 500 eV and convergence of the calculations is 1meV. The knowledge of elastic constants is essential for many practical applications related to the mechanical properties of solids, for example, thermoelastic stress, internal strain and fracture toughness. Elastic constants determine the response of crystal to external forces. They play an important role in determining the strength of the material.

The elastic properties of solids are important hence they are related to various fundamental properties, equation of state, phonon spectra etc. We have calculated the elastic constants (C_{11},C_{12},C_{13},C_{33} and C_{44}) for Li_2S,Li_2O, Li_2O_2 and Li_2S_2 in their anti-fluorite and hexagonal phases, and compared them with experimental and theoretical results.

In Table 5 we list the elastic moduli, anisotropy ratio and bulk moduli for Li_2S, Li_2O, Li_2O_2 and Li_2S_2 structures. In the cases of Li_2S and Li_2O, our calculated values are in good agreement with experimental values. Whereas in the case of Li_2O_2 and Li_2S_2, our calculated values are lower than the experimental results, using LDA and GGA especially Li_2O_2. There is no much work done on Li_2S_2 experimental results.

The mechanical stability criteria of cubic systems as outlined elsewhere [26] are given as follows:

$$C_{44} > 0,\ C_{11} > |C_{12}| \quad \text{and} \quad C_{11} + 2C_{12} > 0, \qquad (3.1.1)$$

where C_{11}, C_{12} and C_{44} are the only three independent elastic constants. Based on three independent single crystal elastic constants of a cubic crystal, C_{11}, C_{12}, C_{44}, the elastic moduli are determined using the following expressions:

$$B = \left(\frac{C_{11} + 2C_{12}}{3}\right), C' = \frac{C_{11} - C_{12}}{2}, A = \frac{(2C_{44} + C_{12})}{C_{11}}, \qquad (3.1.2)$$

where B is the bulk modulus, C' tetragonal shear modulus and anisotropic factor A.

The corresponding mechanical stability criterion for hexagonal crystal reads as

$$C_{11}>0,\ C_{11}-C_{12}>0,\ C_{44}>0,\quad (C_{11}-C_{12})\,C_{33}-2C_{13}^{2}>0 \qquad (3.1.4)$$

All the structures Li_2S,Li_2O, Li_2O_2 and Li_2S_2 in their anti-fluorite and hexagonal phases, satisfy necessary conditions of cubic and hexagonal for stability.

Table 5 : The elastic constants (GPa), anisotropy ratio and bulk moduli for Li_2S, Li_2O, Li_2O_2 and Li_2S_2 structures.

	Li_2O		Li_2S		Li_2O_2		Li_2S_2
	VASP	EXP [27]	VASP	EXP [20]	VASP	EXP [25]	VASP
C_{11}	200.60	217.0	82.14	83.9	169.0	207.3	72.90
C_{12}	19.39	25.0	18.43	18.10	49.77	33.80	24.81
C_{13}					-0.13	21.50	-3.24
C_{33}					158.5	358.1	36.63
C_{44}	50.65	68.0	34.19	32.20	38.13	46.40	4.43
C'	90.61		96.01		59.50		48.09
B	79.59		39.67		89.51		40.84
A	0.30		1.05		0.75		0.46

3.7. Phonon Dispersions for the Li_2S, Li_2O, Li_2O_2 and Li_2S_2 Structures.

The study of phonons is an important part of solids states physics, since phonons play a major role in many physical properties of the solids, including materials thermal conductivity. In particular, the properties of long- wavelength phonons give rise to sound in solids. Phonons are quantum mechanical version of a special type of vibrational motion, known as normal modes in classical mechanics, in which each part of a lattice oscillates with the same frequency. The normal modes are the elementary vibrations of the lattice. The phonon spectrum of Li_2S, Li_2O, Li_2O_2 and Li_2S_2 structures

were investigated by VASP code that allow inter-atomic forces to be calculated. We used the PHONON code of Parlinski interfaced to VASP, which allows phonons, thermodynamic properties such as lattice specific heat, vibration energy and free energy to be calculated. PHONON is a software for calculating the dispersion curves, and phonon density spectra of crystals from either a set of force constants, or from a set of Hellmann-Feyman forces computed within an ab initio program which optimizes the structure of the crystalline supercell within constraints imposed by a crystallographic space group. In Figure 9 and Figure 10 we comparing experimental results with computed phonon dispersions for Li_2S and Li_2O structures. For Li_2S there is a good agreement of calculated and experimental, especially on acoustic modes and lower optical modes. For Li_2O there is a good agreement of calculated and experimental, especially on acoustic modes and lower optical modes. In Figure 11 and Figure 12 we present the calculated phonon DOS and phonon spectra for Li_2O and Li_2S structures, the phonon spectra indicates that the two structures are stable due to the absence of vibrations in the negative frequency which is in good agreement with the calculated elastic properties. For Li_2O, the lithium atoms vibration in the x,y and z components dominates a lot in the optical modes, with the oxygen atoms vibrations in the x,y and z components dominating in the acoustic mode. For Li_2S, the lithium atoms vibration in the x,y and z components dominates a lot in the optical modes, with the sulphur atoms vibrations in the x,y and z components dominating in the acoustic mode.

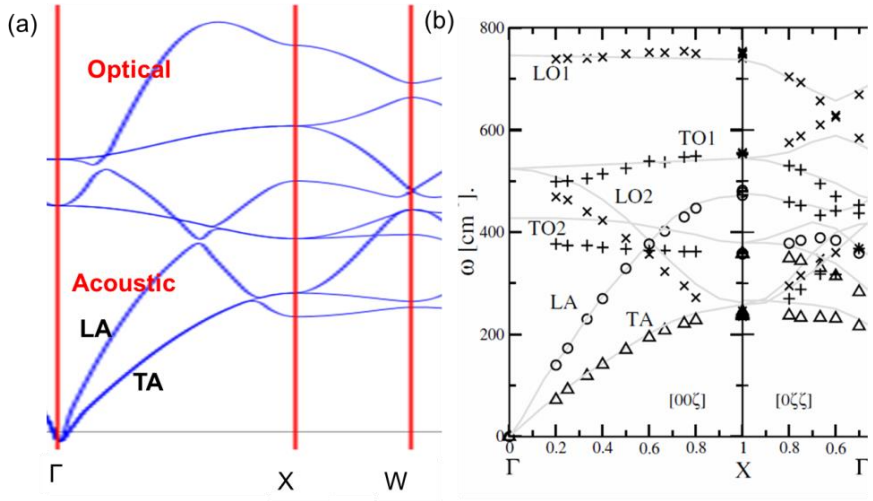

Figure 9 : Phonon dispersion of (a) calculated and (b) experimental for Li_2O [100].

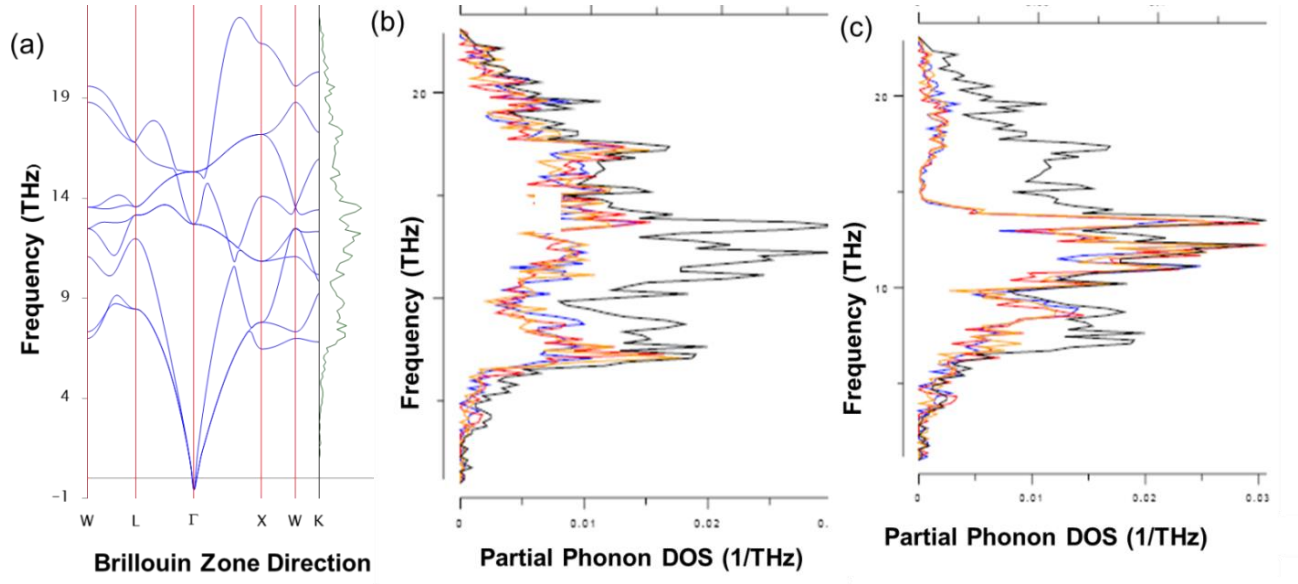

Figure 10 : Phonon dispersion spectra for (a) Li_2O, (b) phonon density of states for lithium contribution and (c) oxygen contribution. With red, yellow and blue representing x,y and z components respectively.

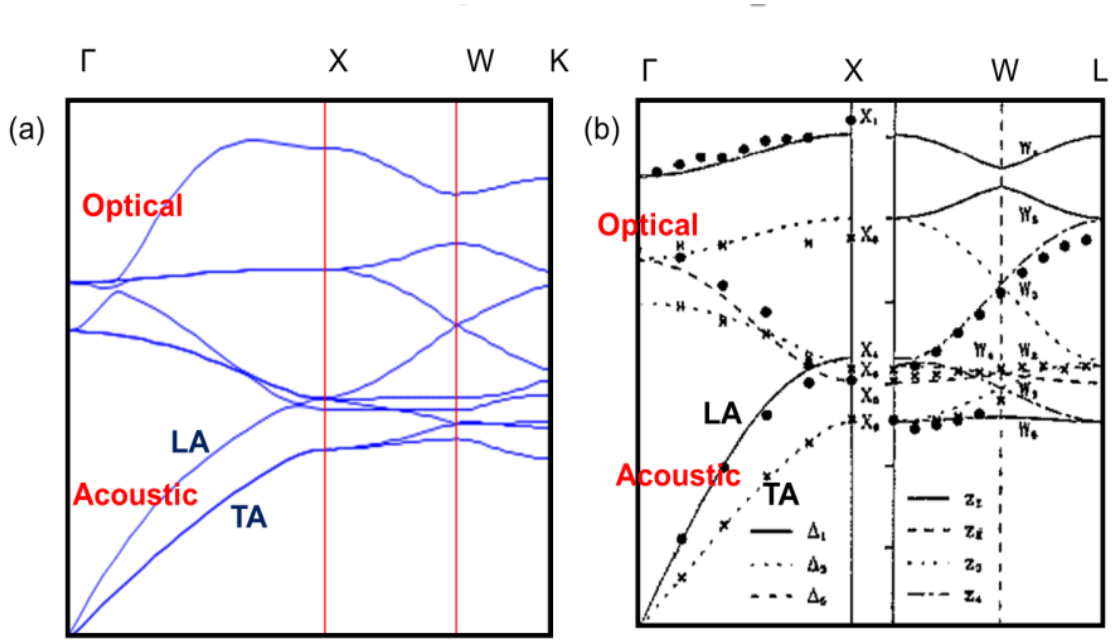

Figure 11 : : Phonon dispersions of (a) calculated and (b) experimental for Li_2S [21].

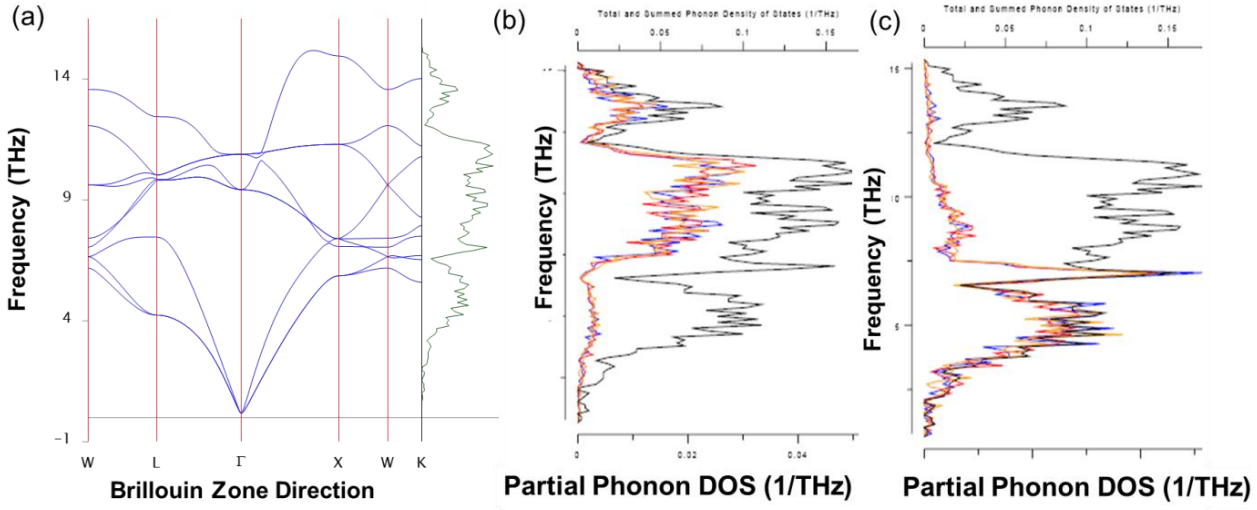

Figure 12 : : Phonon dispersion spectra for (a) Li_2S, (b) phonon density of states for lithium contribution and (c) sulphur contribution. With red, yellow and blue representing x,y and z components respectively.

In Figure 13 we present the calculated phonon DOS and phonon spectrum for Li_2O_2 structure, the phonon spectra indicates that the structure is generally stable even though

it has some small soft modes which is in good agreement with the calculated elastic constant values C_{13}. The lithium atoms vibrations in the z component dominates the optical mode with x and y components absence, with the oxygen atoms vibrations x,y and z components dominating the acoustic modes.

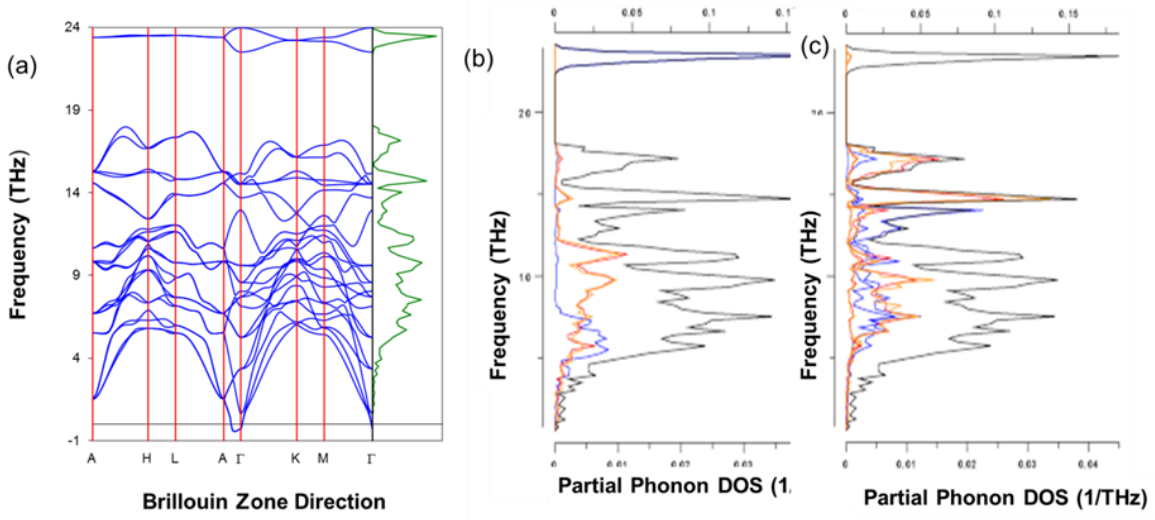

Figure 13 : Phonon dispersion spectra for (a) Li_2O_2 ,(b) phonon density of states for oxygen contribution and (c) lithium contribution. With red, yellow and blue representing x,y and z components respectively.

In Figure 14 we present the calculated phonon DOS and phonon dispersion for Li_2S_2 structure, the phonon spectra indicates that the structure is unstable due to the presence of vibrations in the negative frequency which agrees well with the calculated elastic properties. The soft modes observed are along F, B, G and Γ directions on the phonon spectra

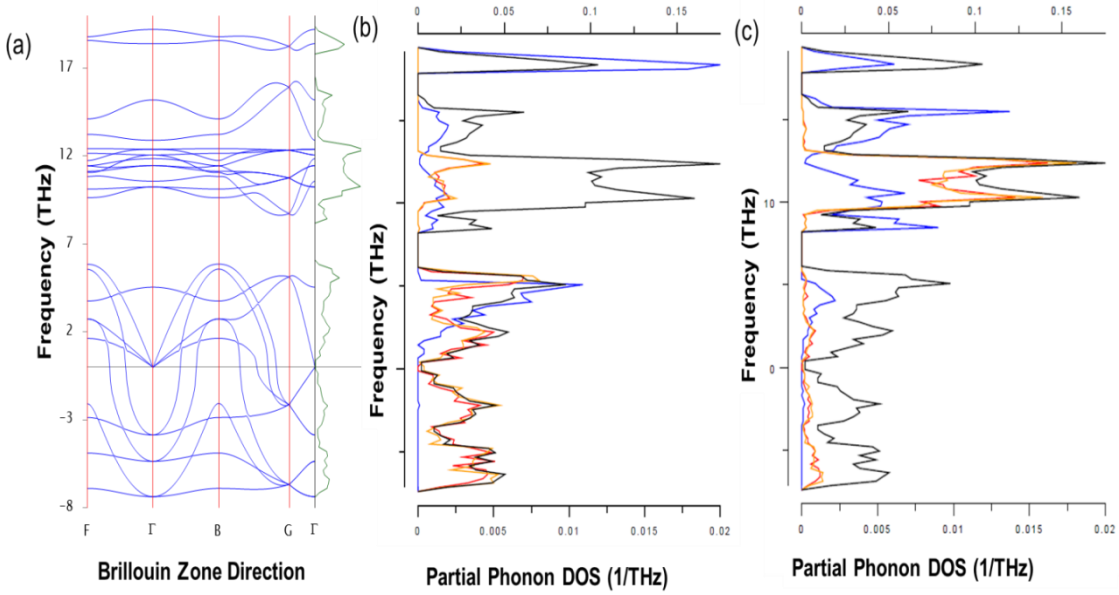

Figure 14 : Phonon dispersion spectra for (a) Li_2S_2, (b) phonon density of states for sulphur contribution and(c) lithium contribution. With red, yellow and blue representing x,y and z components respectively.

In Figure 14 we present the calculated phonon DOS for Li_2S_2 structures, We obtained phonon density of states to check which between lithium and sulphur is responsible for the soft modes on phonon dispersion. We have noticed that the soft modes observed on phonon dispersion are due to the high vibrations of the sulphur atoms as observed on the phonon density of states. The soft modes are also due to a negative C_{13} value observed on elastic constant table.

In Figure 15 we present structures extracted, Further study on the negative energies of the phonon dispersion was done on unstable Li_2S_2 structure using VASP to investigate other polymorphs of Li_2S_2 which might be stable. Using the obtained dispersion we extracted other structures of Li_2S_2 with different symmetries (polymorphs). The polymorphs that were obtained are Li_2S_2 (P-1, P2_1 and P1_2/m), this polymorphs were then optimized, structural, electronic and mechanical properties were investigated to

check which of the polymorphs is stable. Li_2S_2 (P2_1) structure was found to be more stable among other polymorphs, which can be observed from Figures 16, 17 and 18.

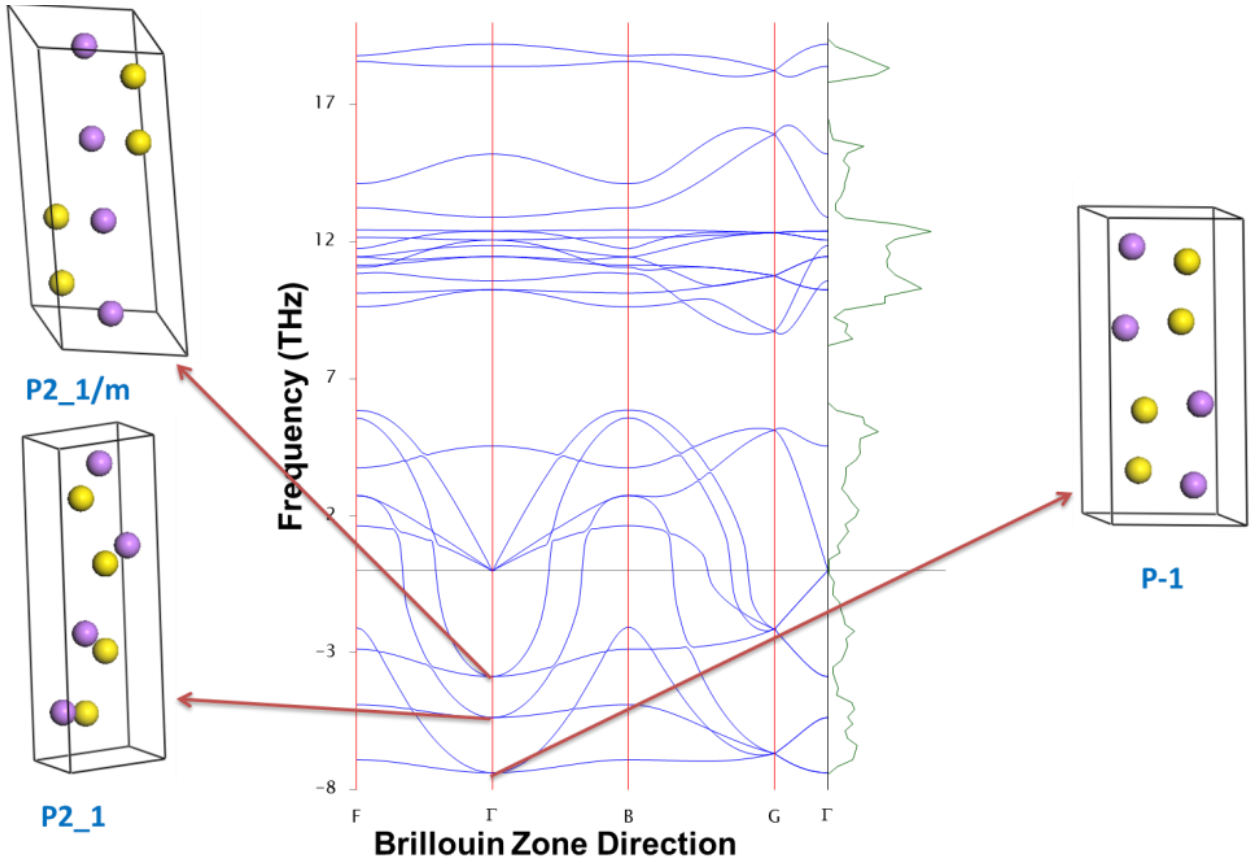

Figure 15 : Polymorphs extraction from Li_2S_2 phonon dispersion.

Table 6 : The equilibrium lattice parameters and heats of formation (ΔHf) of the Li_2S_2 polymorphs- Li_2S_2 (P2_1), Li_2S_2 (P2_1/m) and Li_2S_2 (P_1) structures.

Structure	Lattice Parameters (Å)		ΔH_f (KJ/mol)		Volume
	VASP	experimental	VASP	experimental	($Å^3$)
Li_2S_2 (P2_1)	a= 4.19		-158.34		145.28
	c= 9.93				
Li_2S_2 (P2_1/m)	a= 4.31		-153.15		146.33
	c= 9.84				
Li_2S_2 (P_1)	a= 4.22		-161.92		142.33
	c= 9.13				

Table 7 : The elastic constants (GPa), anisotropy ratio and bulk moduli for Li_2S_2 polymorphs- Li_2S_2 (P2_1), Li_2S_2 (P2_1/m) and Li_2S_2 (P_1) structures.

	Li_2S_2 (P2_1)		Li_2S_2 (P2_1/m)		Li_2S_2 (P_1)	
	VASP	experimental	VASP	experimental	VASP	experimental
C_{11}	79.57		84.79		68.28	
C_{12}	4.25		-0.20		22.77	
C_{13}	22.29		23.16		9.78	
C_{33}	61.77		71.98		58.15	
C_{44}	8.62		3.04		24.88	
C'	41.91		42.29		45.53	
B	29.36		28.13		37.94	
A	0.52		0.10		1.06	

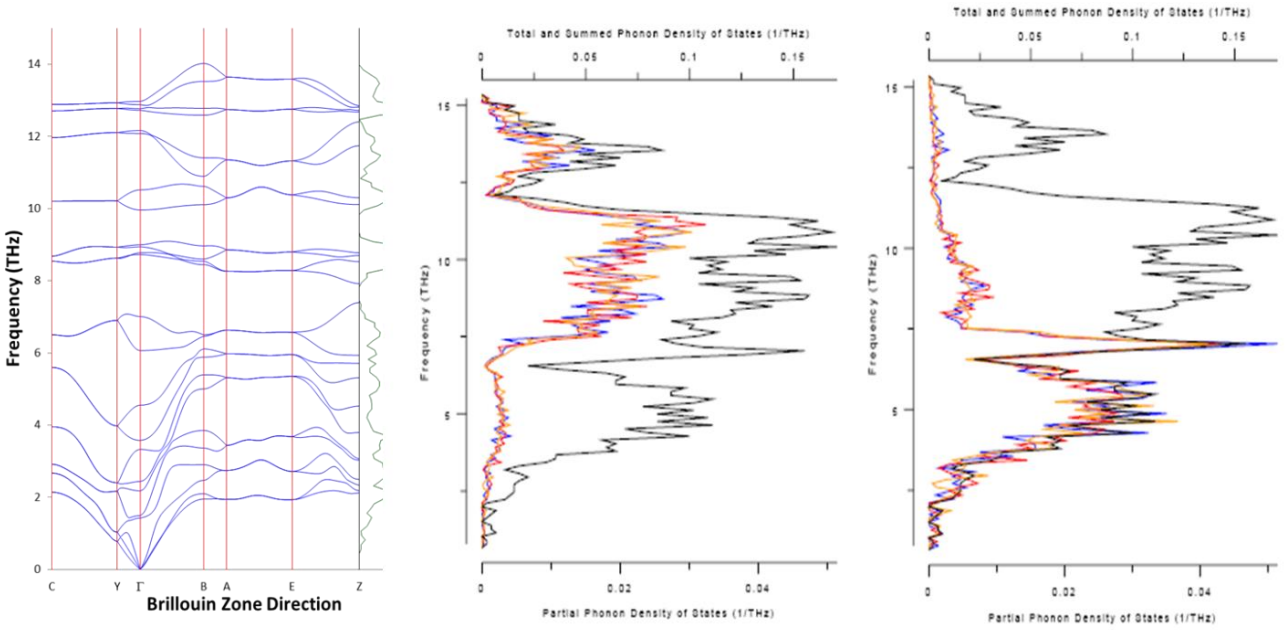

Figure 16 : Phonon dispersion spectra for (a) Li_2S_2 (P2_1), (b) phonon density of states for lithium contribution and (c) sulphur contribution. With red, yellow and blue representing x,y and z components respectively.

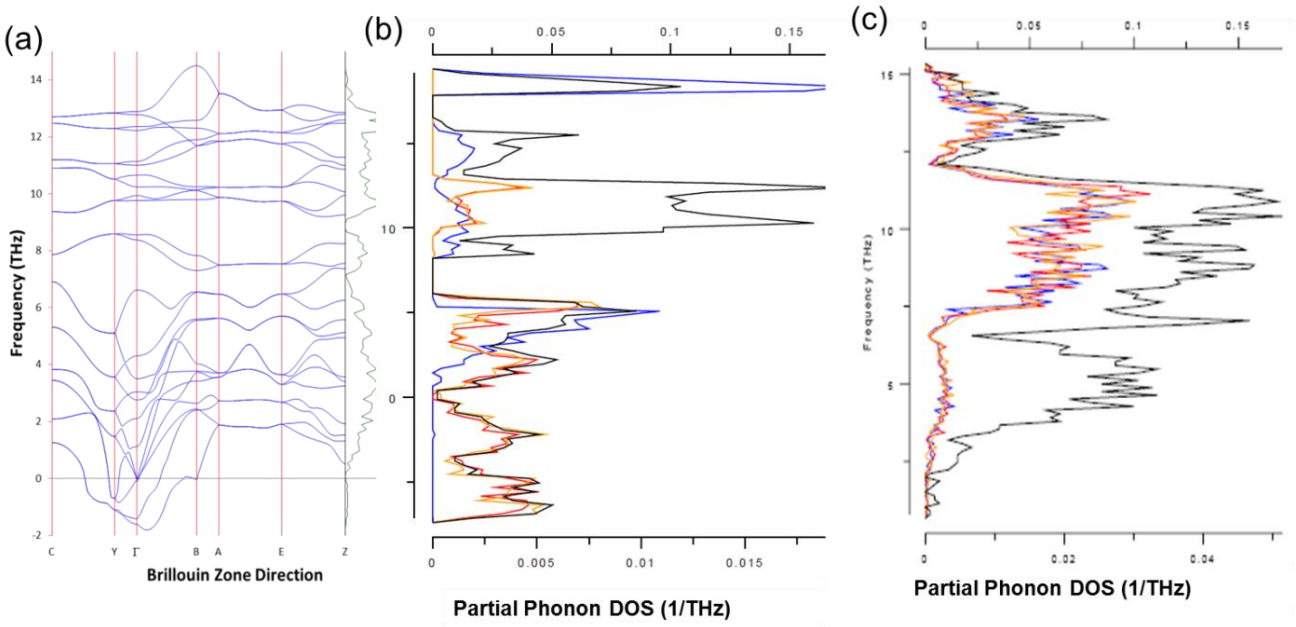

Figure 17 : Phonon dispersion spectra for (a) Li_2S_2 (P2_1/m), (b) phonon density of states for lithium contribution and (c) sulphur contribution. With red, yellow and blue representing x,y and z components respectively.

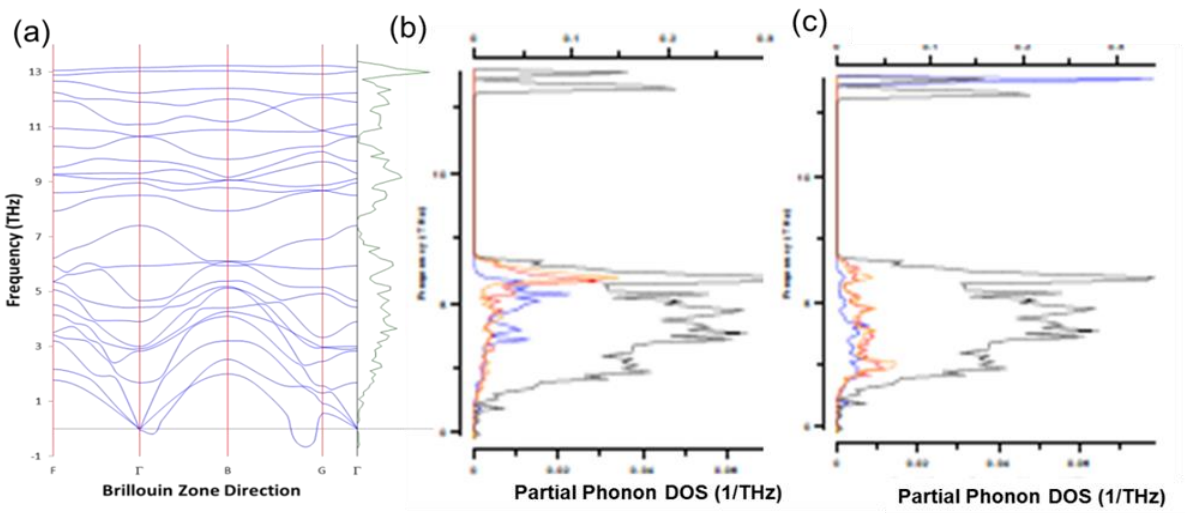

Figure 18 : Phonon dispersion spectra for (a) Li_2S_2 (P_1), (b) phonon density of states for lithium contribution and (c) sulphur contribution. With red, yellow and blue representing x,y and z components respectively

3.8. Density of States for Li_2S, Li_2O, Li_2O_2 and Li_2S_2 Structures.

The density of states (DOS) of a system describes the number of states at each level that are available to be occupied by electrons. A high DOS at specific energy level means that there are many states available for occupation. A DOS of zero means that no states can be occupied at that energy level. From the DOS we can deduce the nature of materials and also predict the stability of the systems.

In figure 19 and figure 20 show the density of states (DOS) and partial density of states (PDOS) of Li_2O, Li_2S, Li_2O_2 and Li_2S_2 structures. There is a clear distinction between the plots for the Li_2O, Li_2S, Li_2O_2 and Li_2S_2 structures. However, their density of states behaviour at E_f is significant and can be used to correlate their stability. It is also known from literature that the DOS of structures of the same composition can be used to mimic the stability trend with respect to their behaviour at the E_f. The structure with the highest and lowest density of density at E_f is considered the least and most stable, respectively. The total and partial DOS indicates that on Li_2O and Li_2S p orbitals of Li predominates

at Fermi energy level and also s orbital of O and S respectively. For Li_2O_2 and Li_2S_2 structures the total and partial DOS indicates that Li p orbital dominates and also s orbitals of O and S respectively. Furthermore, we determined whether our structures are metal, semi-conductors or insulators by measuring their band gaps respectively. From figures we measured the band gaps of all the discharge products to confirm whether they are metal, semi-conductors or insulators, Li_2O and Li_2S have the band gaps of 5 and 3.7 eV respectively hence they are called insulators, whereas Li_2O_2 andLi_2S_2 have the band gaps of 2.2 and 2.0 eV hence they are preferably called semi-conductors.

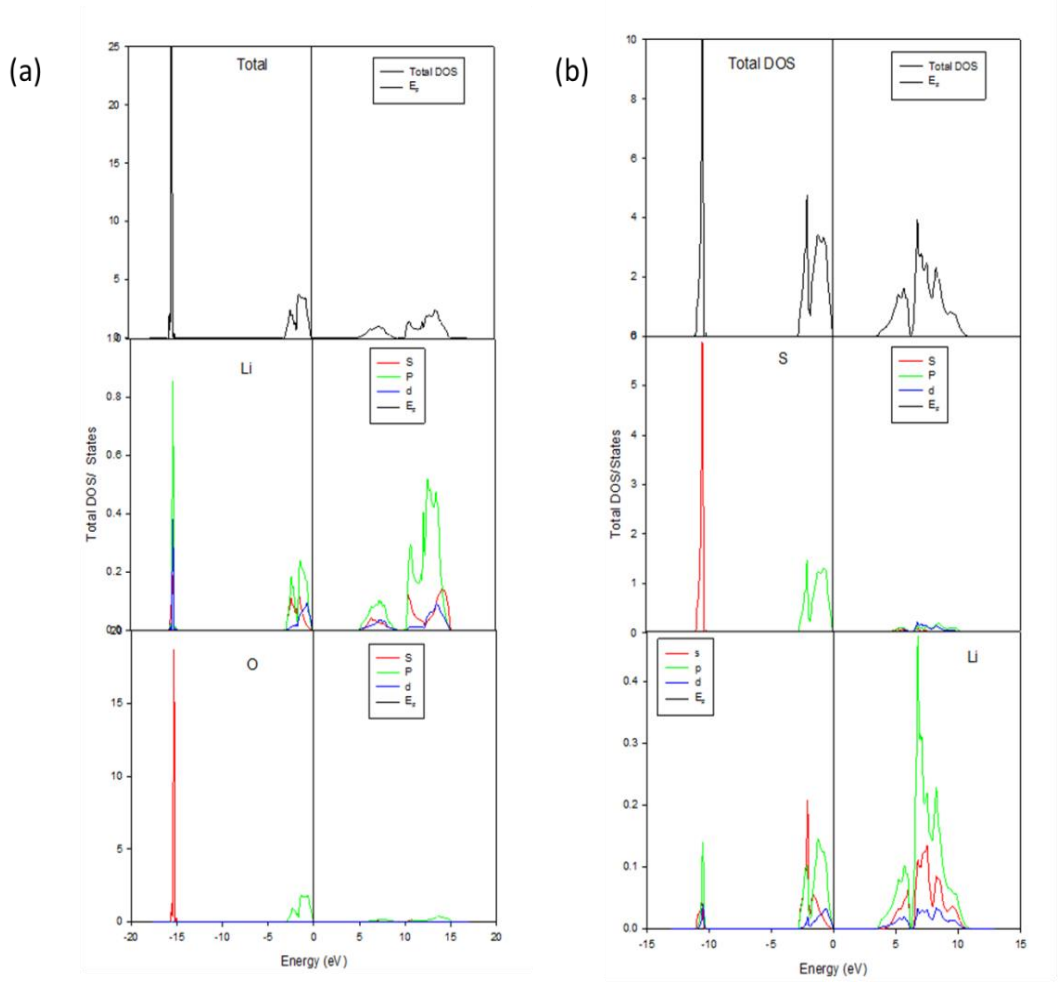

Figure 19 : DOS and PDOS of (a) Li_2O and (b) Li_2S.

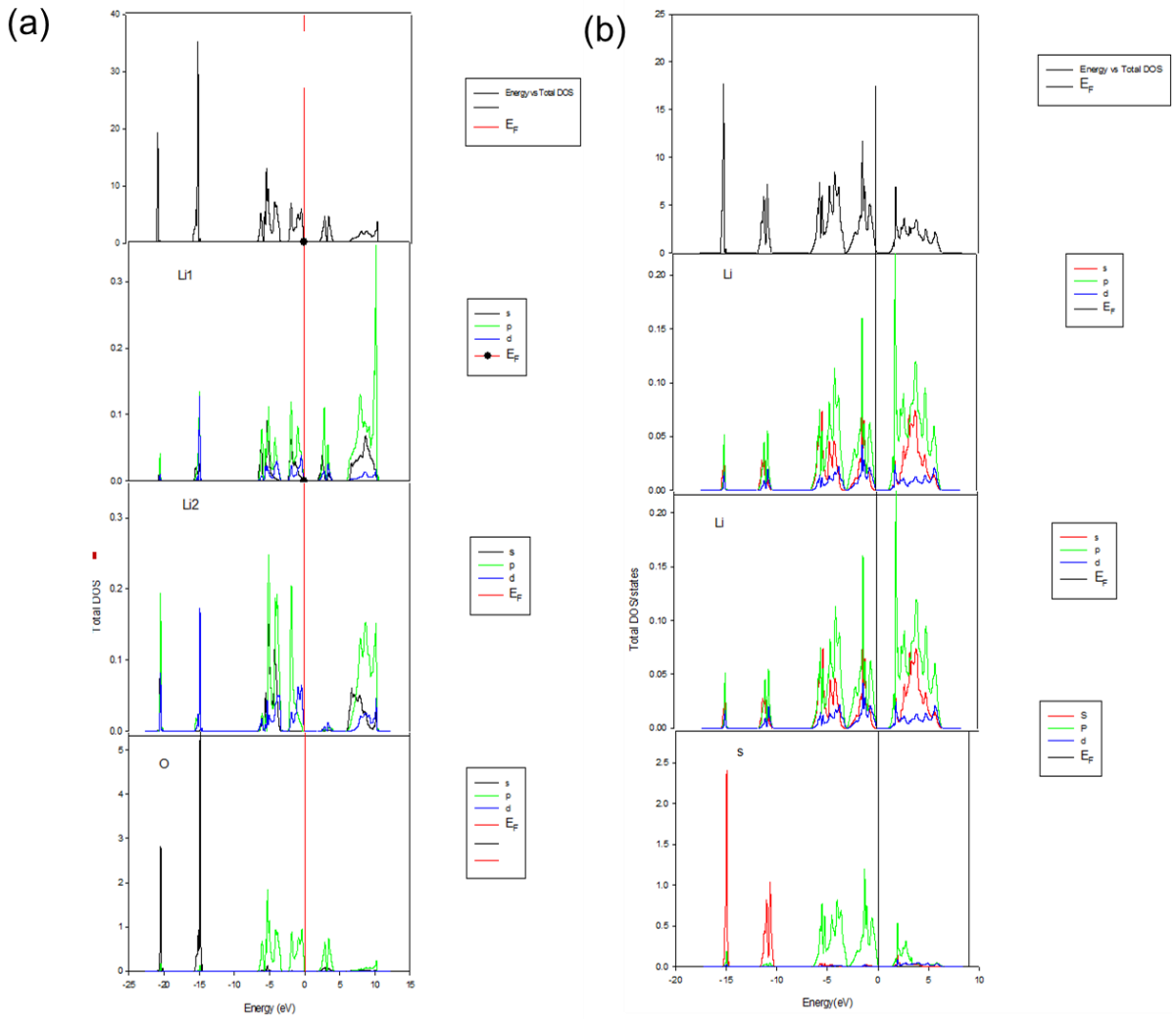

Figure 20 : DOS and PDOS of (a) Li_2O_2 and (b) Li_2S_2

3.9. Discussions

In this chapter we present first principle study on the discharge products formed in Li-S and Li-O batteries which are Li_2S, Li_2O, Li_2O_2 and Li_2S_2 structures. The equilibrium lattice parameters of the Li_2S, Li_2O, Li_2O_2 and Li_2S_2 structures were performed within the generalised gradient approximations. Li_2S, Li_2O and Li_2O_2 structures are well studied either experimentally or theoretically and the results were found to be in good agreement with the available experimental values and the heats of formations suggest that the structures are stable as well with low negative values. The calculated electronic

and elastic properties of Li_2S, Li_2O and Li_2O_2 structures were found to be in good agreement with experimental studies and elastic properties indicates that the structures are mechanically stable due to positive values. The calculations on the phonon dispersion and the density of states were performed and they confirm the stability of Li_2S, Li_2O and Li_2O_2 structures.

Phonon dispersions indicates that the structures are very stable due to the absence of soft modes in the negative frequency which is in great agreement with experimental work and also calculated elastic properties which are all positive. Calculated electronic density of states to check whether studied materials are semi-conductors, metals or insulators. Density of states depicts that Li_2O and Li_2S are called insulators.

Li_2S_2 structure has not been studied and the first principle studies are unavailable in literature. In this thesis the material was studied to explore properties such as structural, electronic and mechanical properties. Heats of formation value is close zero all indicating that the structure is stable. Furthermore, the phonon dispersion curves of the Li_2S_2 structure showed the availability of the soft modes which are due to the negative elastic constant C_{13} of the structure. We also performed phonon density of states for Li_2S_2 structure to check which between lithium and sulphur is responsible for instability of the structure, we have found out that the instability of Li_2S_2 structure is due to high vibrations of sulphur atoms.

We further extracted other polymorphs of Li_2S_2 structure from phonon dispersions curves along gamma direction on the brilliuon zone of unstable Li_2S_2 structure, we managed to obtain a stable new polymorph of Li_2S_2 structure from phonon dispersion curve. Finally we, noticed that Li_2O_2 and Li_2S_2 are preferably called semi- conductors from density of states.

Chapter 4: Interatomic Potential Models for Li_2S and Li_2Se Systems

In this chapter the description of quantum mechanical and atomistic simulation methods is given. Related approximations and derivation of potential models are discussed, together with their validation.

Both the energy minimisation and molecular dynamics (MD) techniques, discussed in the previous sections, require that the forces between atoms (interatomic interactions) are evaluated at each step. This chapter focuses upon the description of such interatomic interactions and their use to calculate the total energy of a system. The description of such interatomic interactions can be separated into two distinct methodologies: atomistic techniques and *ab initio* techniques.

Atomistic simulation techniques (discussed in this section) employ simple empirically derived equations to describe the interatomic interactions. In comparison ab initio techniques (discussed previously; Electronic Structure Techniques) are based upon the fundamental principles of quantum mechanics, and as such present an increased level of complexity. For theoreticians the choice between which of these different techniques to employ is often determined by the information required coupled with the computational time and resources available. Using atomistic techniques it is possible to simulate large numbers (tens of thousands) of atoms. Hence such methods are particularly suited to modelling the relaxation around defects, the influence of which can extend significantly into the crystal lattice of a system. Atomistic techniques are also ideal for producing accurate statistical data from MD simulations, enabling the use

of the prerequisite large simulation cells and long simulation times. Ab initio techniques can be used to provide a material study offering a much more detailed insight into the underlying chemistry. However, such techniques are significantly more computationally expensive, and are therefore more appropriate for smaller systems.

4.1. Atomistic Potential Model

Atomistic potential models describe the variation in the energy of the molecule or solid as a function of atomic coordinates [101]. The reliability of the calculations depends on the quality and accuracy of the potential model. The potential model; describes the interactions between two or more species. The different Coulombic summation schemes that have been employed are described. Finally, the potential functions used in this study are presented and all the potential parameters are discussed.

4.1.1. The Born Model of Solids

The atomistic simulation techniques used in this study are based on the Born model of solids [102]. In this model, it is assumed that the energy and its derivatives can be defined as the summation of all interactions between the atoms in the system which gives rise to the total interaction and total net force acting on each atom due to others [103]. Furthermore, the atoms of a system are represented as point-charge particles that interact via long-range electrostatic forces and short-range interactions. Hence, the interaction energy between two ions is obtained by

$$\phi_{ij} = \frac{1}{4\pi \in_0} \frac{q_i q_j}{r_{ij}} + \Phi\left(r_{ij}\right) \tag{4.1}$$

Where the first term represents the long-range Coulombic interactions, $\in_0$ is the permittivity of vacuum, q_i and q_j are the ionic charges, and r_{ij} is the interatomic distance. The second term, $\Phi(r_{ij})$, describes the short-range interactions between ions, which include the repulsion between the electron charge clouds and the van der Waals attraction forces.

The interaction energy of a system is the sum of the pairwise interactions between all ions i and j. Where appropriate, many-body terms are also included to take into account, for example, deviations from equilibrium bond angles. Thus, the overall interaction energy of a system can be written in terms of the atomic positions

$$\phi_i = \sum_{i}^{N} \sum_{\substack{j \\ j \neq i}}^{N} \frac{1}{4\pi \in_0} \frac{q_i q_j}{r_{ij}} + \sum_{i}^{N} \sum_{\substack{j \\ j \neq i}}^{N} \Phi(r_{ij}) + \sum_{i}^{N} \sum_{\substack{j \\ j \neq i}}^{N} \sum_{\substack{k \\ k \neq i \\ k \neq j}}^{N} \Phi_{ijk}(r_{ijk}) \qquad (4.2)$$

The first term of the equation (4.2), the Coulombic energy of the system, cannot be obtained by simply summing all the pairwise electrostatic interactions. This is because the contribution of the point-charges to the electrostatic potential decays as 1/r, which causes the Coulombic term to converge very poorly. Therefore, the electrostatic interactions are calculated using summation methods, such as the Ewald sum for example, as described later in this chapter. The other terms of equation 2, the short-range interactions, converge much faster and thus can usually be calculated by a simple summation.

4.1.2. Long Range Interactions

Coulombic Simulation

The electrostatic interactions between charged particles are long-ranged and hence a particle i will interact with all other particles j in the simulation box and also, with the periodic images of these particles, including those of i. Therefore, the Coulombic contribution, ϕ_i to the interaction energy is

$$\phi_i = \frac{1}{2}\left(\frac{1}{4\pi \in_0}\right)\sum_n \sum_{i=1}^{N}\sum_{j=1}^{N} \frac{q_i q_j}{\left|r_{ij} + nL\right|} \tag{4.3}$$

where q_i and q_j represent the charges on particles i and j, r_{ij} is the interatomic distance, $\in_0$ is the permittivity of free space, and L is the set of simulation cell vectors reflecting the periodicity of the simulation box. The sum over n is the sum of all the periodic images where n is the ordered triple of integers that define the periodic images, where n is the ordered triple of integers that define the periodic images of the simulation cell. The prime on the first summation indicates that $i = j$ is ignored for $n = 0$. The problem is that the sum in (Equation 4.3) is very slow to converge due to the $1/r$ term. Therefore, one needs a quicker and more reliable summation scheme such as Ewald summation.

Ewald Summation

Ewald summation [104] is an excellent technique for calculating electrostatic interactions in periodic systems in three-dimension and is an efficient technique for summing the interaction between an ion and all its infinite periodic images. This method divides the Coulombic potential into three separate parts, i.e. a term in reciprocal space, ϕ_1, a real space term, ϕ_2, and a self-interaction term ϕ_3, where:

$$\phi = \phi_1 + \phi_2 + \phi_3 \tag{4.4}$$

In the Ewald method, every particle, of charge q_i, is assumed to be surrounded by a spherically symmetric charge distribution of opposite sign, which exactly cancels q_i and is usually taken to be a Gaussian distribution such as

$$\rho_i(r) = -q_i\left(\frac{\alpha}{\pi}\right)^{3/2} \exp\left(-\alpha r^2\right) \tag{4.5}$$

Where the arbitrary parameter α determines the width of the distribution, and r is the position relative to the centre of the distribution. Therefore, only the fraction of q_i that is not screened contributes to the electrostatic potential due to the particle i. At long distances, this fraction rapidly converges to zero and the screened interactions are thus short-ranged. Therefore, the electrostatic interactions between these screened charges can now be calculated by direct summation in real space.

The total contribution of the screened Coulombic interactions, ϕ_i to the interaction energy is then given by

$$\phi_2 = \frac{1}{2}\left(\frac{1}{4\pi \in_0}\right)\sum_n \sum_{i=1}^{N}\sum_{j=1}^{N} \frac{q_i q_j}{\left|r_{ij} + nL\right|} \times erfc\left(\alpha\left|r_{ij} + nL\right|\right) \tag{4.6}$$

where *erfc* is the complementary error function

$$erfc(x) = 1 - \frac{2}{\sqrt{\pi}}\int_0^x \exp\left(-t^2\right)dt \tag{4.7}$$

The rate of convergence of Equation 4.6 is dependent on the width of the cancelling Gaussian distribution, defined by α; the wider the Gaussians; the faster the series converges, as Equation 4.7 tends to zero with increasing x.

The contributions of the charge distributions to the electrostatic potential, ϕ_1 are calculated by summing their Fourier transforms in reciprocal space, further detail is given in Kittel (1963) [105]:

$$\phi_1 = \frac{1}{2}\sum_{k\neq 0}\sum_{i=1}^{N}\sum_{j=1}^{N}\frac{1}{\pi\lambda^3}\frac{q_i q_j}{4\pi\varepsilon_0}\frac{4\pi^2}{k^2}\exp\left(-\frac{k^2}{4\alpha^2}\right)\cos\left(K.r_{ij}\right) \qquad (4.8)$$

where the vectors K are reciprocal vectors and given by $K = 2\pi n/\lambda$. This expression ignores the term when $k = 0$, which can be neglected provided the net charge on the unit cell is zero. Although this reciprocal sum converges much more rapidly than the original point charge sum, the number of terms that need to be included increases with the width of the Gaussians. The ϕ_1 summation includes the interaction between the continuous Gaussian charge cloud of charge q_i with itself. The self-interacting component, ϕ_3, must be subtracted. The self-interaction term is defined as:

$$\phi_3 = -\frac{\alpha}{\sqrt{\pi}}\sum_{k=1}^{N}\frac{q_k^2}{4\pi\varepsilon_0} \qquad (4.9)$$

Three parts of the electrostatic interaction can then be summed to give the overall Coulombic interaction using Equation 3.4.

Parry Summation

The Parry summation [105] , which is a modification of the Ewald method was used in this study, in the simulations of surfaces, which are two dimensional periodic systems. In this method, the crystal is assumed to consist of a series of charged planes of infinite size rather than an infinite lattice. When summing the electrostatic interactions the vectors are now divided into in-plane vectors and vectors perpendicular to the plane. Hence the reciprocal space term needs to be modified to account for the fact that the

overall charge of a plane of atoms can be different from zero. The detailed derivation of the reciprocal space term can be found in reference [106].

4.1.3. Short Range Interactions

The short range interactions consist of different contributions. At small distances electron charge clouds will start to interact strongly and therefore will repel each other. Also, at these distances, the dipole-dipole interactions, due to fluctuating dipoles on each ion, will result in attractive van der Waals forces. In addition, when considering covalent systems, the short-range interactions between three or more ions can also be included in the model to represent directionality in the bonding. In this work, the short-range attractive and repulsive interactions are described by simple parameterised potential functions. The potential parameters can be derived empirically by fitting to experimental data, such as crystallographic positions, elastic or dielectric properties, and infrared frequencies, or, by fitting to more accurate simulations such as electronic calculations.

Lennard-Jones Potential

The Leonard-Jones potential is often used to describe the intermolecular interactions and takes the form:

$$U\left(r_{ij}\right)=\frac{A_{ij}}{r_{ij}^{n}}-\frac{B_{ij}}{r_{ij}^{m}} \tag{4.10}$$

where the most common values for n and m are 12 and 6, respectively. The first term represents the repulsion between electronic clouds, which dominates at very short distances. The second term is the attractive part of the potential and models the van der Waals dispersion forces, which dominate at larger distances.

To facilitate the parameters (n and m) fitting process, the Lennard-Jones potential can also be written as:

$$U(r_{ij}) = \frac{E_0}{(n-m)}\left[m\left(\frac{r_0}{r_{ij}}\right)^n - n\left(\frac{r_0}{r_{ij}}\right)m \right] \tag{4.11}$$

Buckingham Potential

In the Buckingham potential, the repulsive term is replaced by an exponential term and potential takes the form

$$U(r_{ij}) = A_{ij} \times \exp\left(-r_{ij} \Big/ \rho_{ij}\right) - \frac{C_{ij}}{r_{ij}^6} \tag{4.12}$$

Where A_{ij} and ρ_{ij} are parameters that represent the ion size and hardness, respectively. The first term is known as the Born-Mayer potential and the attraction term was later added to form the Buckingham potential. Very often, for the cation-anion interactions, the attractive term is ignored due to the very small contribution of this term to the short-range potential, or, alternatively, the interaction is subsumed into the A and ρ parameters.

Morse Potential

The Morse potential is used to model the interactions between covalently bonded atoms and has the form

$$U(r_{ij}) = A_{ij} \times (1 - \exp(-B_{ij} \times (r_{ij} - r_0))^2 - A_{ij} \tag{4.13}$$

where A_{ij} is the bond dissociation energy, r_0 is the equilibrium bond distance, and B_{ij} is a function of the slope of the potential energy well. The Coulombic interactions

between covalently bonded atoms are often partially or totally ignored as the Morse potential already contains the attractive component of the interaction between neighbours.

Three-Body Potential

A further component of the interactions of covalent species is the bond-bending term, which is added to take into account the energy penalty for deviations from the equilibrium value. Hence, this potential describes the directionality of the bonds and has a simple harmonic form:

$$U\left(\theta_{ijk}\right)=\frac{1}{2}k_{ijk}\left(\theta_{ijk}-\theta_0\right)^2 \tag{4.14}$$

where k_{ijk} is the three-body force constant and θ_0 is equilibrium angle

Shell Model Potential

The shell model is different from previous models; it includes the electronic polarisation of the atoms. The shell model was developed by Dick and Overhauser in 1958 [107]. In this model the ion is described by a core and a shell. The core, which contains all the mass of the ion, is attached to the shell by harmonic spring. The shell has no mass and models the electronic charge cloud. The core has all the ion's mass and determines the position of the ion. The total charge of the ion is shared between the core and the shell. The core has the positive charge and the shell a negative charge; however there exist potentials for highly oxidised cations that have positive charges on the shell. Figure 3.3 shows a schematic representation of the shell model.

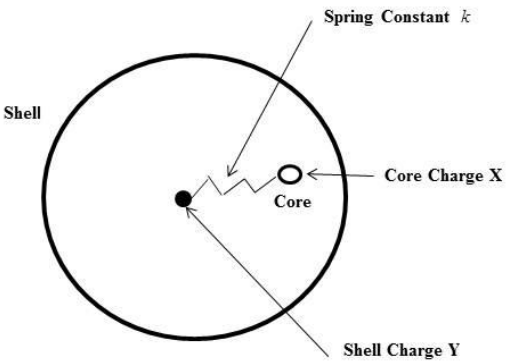

Figure 21: Schematic representation of the shell model.

The ion electronic polarisability, α, is related to the shell charge, Y, and the spring constant, k, by

$$\alpha = \frac{Y^2}{k} \tag{4.15}$$

The parameters Y and k are obtained by empirical fitting to dielectric constants, elastic constants or phonon dispersion curves. The disadvantage of shell model is that the number of species in the computer simulation is doubled; hence the calculations become computationally expensive. The remainder of the chapter tackle the methods of deriving the potentials and the potentials used in this work.

4.2. Derivation of Interatomic Potentials

There are two approaches of deriving force fields. The first approach is to adjust the parameters to fit experimental data. This approach depends on the availability of a range of experimental data. The second approach of fitting the potentials parameters is by adjusting the parameters to reproduce *ab-initio* electronic structure data; this is done by adjusting the energy with respect to atomic position. Nowadays with the advancement of computer technologies [108] and the development of good *ab-initio* softwares, such

as VASP code [98] and CASTEP code [109], this approach is being used more often. In the past the first approach was favoured, because the electronic structure calculations were time consuming and because of lack of powerful computers then, hence computationally expensive.

Nevertheless, both approaches use the same principle, which is to derive a model that can accurately reproduce the available data. Data can be elastic constants, bulk moduli, dielectric constants or phonon frequencies. In performing a fit, it is important to define a quantity that measures the quality of results known as the sum of squares F :

$$F = \sum_{i=1}^{N_{obs}} w\left(f_i^{obs} - f_i^{calc}\right)^2 \tag{4.16}$$

where N_{obs} is the number of observables, f_i^{obs} and f_i^{calc} are the fitted and calculated values of the observable, respectively, and w_i is the weighting factor for the observable. There are several criteria of knowing how to choose an appropriate and sensible weighting factor. Firstly, the weighting factor should be inversely proportional to the uncertainty in the measured value, when fitting for experimental data. Secondly, to ensure that all the values are fitted on an equal footing, regardless of units, the weighting factor should be inversely proportional to the magnitude of the observable squared. The process of fitting involves minimising the value of F , through the variation of potential parameters. To do this, we use the default approach which is similar to that used in optimisation. A commonly used approach is a Newton-Raphson minimisation via the simulation package GULP (General Utility Lattice Package) [110].

4.3. The Atomistic Potentials Used In This Work

As with any atomistic simulation, the accuracy and reliability of the results depend, ultimately, on the quality of the interionic potentials [111]. In this section, a simple two-body potential function based on the Born model of ionic solids was used. As with most of MD simulations, the shell model (used to approximate electronic polarization effects) was not incorporated because of the significant increase in computational time that would ensue; as such all particles were assumed to be rigid ions. We report on the derivation of interatomic potentials which were finally tested by comparison of structural results with experimental values. Furthermore, molecular dynamics (MD) calculations, based on such potentials, using the DL_POLY code, were carried out in particular to assess their reliability at high temperatures. The corresponding structural properties of our calculated parameters are in agreement with the experimental and other calculated results. The experimental structural parameters were used as inputs for derivation of the potential model. Elastic properties were calculated by first principle methods (shown in Table 8 and 9), in the current study, to assist in the fitting since no experimental results are available.

Table 8: Calculated elastic constants of Li_2S.

Elastic Constants (GPa)	C_{11}	C_{12}	C_{44}
	82.14	18.43	34.19

Table 9: Calculated elastic constants of Li_2Se.

Elastic Constants (GPa)	C_{11}	C_{12}	C_{44}
	66.78	17.70	29.91

Buckingham potential modelling the interaction between Li-Li, S-S and Li-S ions and between Li-Li, Se-Se and Li-Se ions. Such derived interatomic potentials of Li_2S and Li_2Se are given in Table 10 and Table 11 respectively, and these are, thus far, the best potentials after a considerable developmental effort.

Table 10: Interatomic potential parameters for the Li2S as derived in the present study.

Species	Charge *(e)*			
Lithium (Li)	0.50			
Sulphur (S)	-1.00			
Buckingham Potentials	*A (eV)*	*ρ (Å)*	*C(eV /Å^6)*	*Cut-off(Å)*
Li core – Li core	1200.2	0.2000000	0.000	20
Li core – S core	20144058.0	0.201820	3.000	10
S core – S core	1549955.3	0.132724	32.000	10
Three-body	K_b (eV/rad^2)	$\theta_0{}^0$		
Li core S core S core	3.5412	109.503000		
S core Li core Li core	0.69400	199.730369		

Table 11: Interatomic potential parameters for the Li_2Se as derived in the present study.

Species	Charge *(e)*			
Lithium (Li)	0.50			
Sulphur (Se)	-1.00			
Buckingham Potentials	*A (eV)*	*ρ (Å)*	*C(eV /Å^6)*	*Cut-off(Å)*
Li core – Li core	1200.00	0.2000	20.000	20
Li core – Se core	917183.00	0.147428	30.000	10
Se core – Se core	100201.0	0.284920	22.000	10

Three-body	K_b (eV/rad^2)	θ_0^0
Li core Se core Se core	3.5412	250.503000
Se core Li core Li core	0.69400	99.730369

4.4. Validation of the Atomistic Potentials Model

4.4.1. Structural and Elastic Properties

In this section we consider the validation of our derived interatomic potential models for Li_2S and Li_2Se. The bulk Li_2S and Li_2Se are both cubic and have a space group of *Fm3m* (225) with the lattice parameter a = 5.72 and a = 6.00 respectively. In a unit cell, Li atoms occupy $1/8^{th}$ of the available octahedral and half (1/2) of the tetrahedral sites. One out of every nine cobalt atoms one is in an octahedral position, with the rest occupying pseudo-tetrahedral site. Figure 22 shows the cubic unit cell of bulk Li_2S.

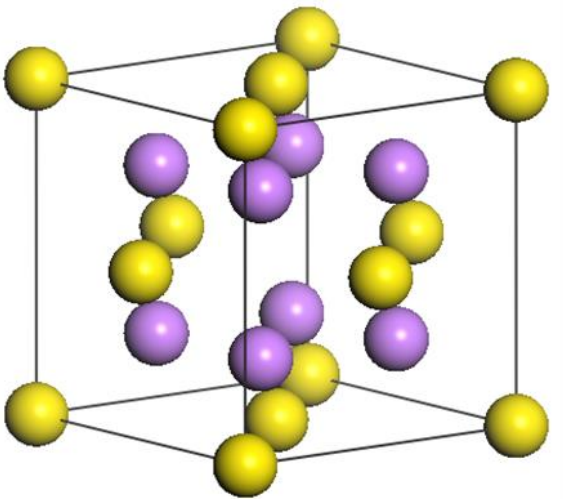

Figure 22: Cubic unit cell of bulk Li_2S.

The potential models are developed to simplify the complexity of the quantum mechanical computations. For example, even a semi-qualitative force field or potential model can be used to identify the most probable surfaces, and hence reduce the number of surfaces that need to be examined using quantum mechanical methods. The elastic constants, calculated by quantum mechanics, were used as input data for the

development of potentials models. The accuracy of the derived interatomic potentials was first checked by comparing the known experimental and calculated data. To validate our potential models we start by showing the properties that where obtained from our derived potentials i.e., lattice parameters, interatomic distances, and elastic properties.

Table 12 shows the calculated lattice parameters obtained from different methods. The lattice parameters obtained using energy minimisation codes GULP and METADISE are smaller than those from the literature, but still within the acceptable range of 2%.

Table 12: Comparison of the lattice parameter of Li_2S, obtained from the derived interatomic potentials, with the other calculated and experimental values.

Method	Parameter *a (Å)*
Potential Model (This Work)	5.68
VASP (GGA-PBE)[a]	5.677
Experimental [a]	5.67
Theoretical [b]	5.645

[112][a] [113]

Table 13 shows a comparison of the elastic properties of Li_2S we calculated using DFT methods (VASP code) and those calculated from our derived interatomic potentials employing the GULP and METADISE codes; experimental elastic constants are available for Li_2S. The elastic constants from the interatomic potentials are in good agreement with those from DFT calculations, together with the various moduli of elasticity, i.e. the bulk, shear, elasticity moduli and Poisson's ratio. In addition, the Li_2S

phase has elastic constants that satisfy the generalized elastic stability criteria for cubic crystals [108] [109]:

$$C_{44} > 0, C_{11} > |C_{12}| \quad \text{and} \quad C_{11} + 2C_{12} > 0 \tag{3.23}$$

Table 13: Calculated elastic constants and moduli of the Li_2S phase.

Elastic Properties	Observable (GGA) [112]	GULP (Fitted)
C_{11}	113.6	108.39
C_{12}	17.8	20.88
C_{44}	26.6	28.52
Bulk Modulus, *B* (GPa)	49.73	50.05
Shear Modulus, *G* (GPa)	35.12	37.56
Elastic Modulus, *E* (GPa)	85.28	87.13

The bulk modulus *B*, shear modulus *G* and elastic modulus *E* of the cubic Li_2S phase were deduced according to the following formulae.

$$B = \frac{1}{3}(C_{11} + 2C_{12}) \tag{3.24}$$

$$G = \frac{1}{5}(C_{11} - C_{12} + 3C_{44}) \tag{3.25}$$

$$E = \frac{(C_{11} - C_{12} + 3C_{44})(C_{11} + 2C_{12})}{2C_{11} + 3C_{12} + C_{44}} \tag{3.26}$$

Poisson ratio v is obtained from:

$$v = \frac{3B - E}{6B} \tag{3.27}$$

Table 14 shows the calculated lattice parameters obtained from different methods. The lattice parameters obtained using energy minimisation codes GULP and METADISE are smaller than those from the literature, but still within the acceptable range of 2%.

Table 14: Comparison of the lattice parameter of Li_2Se, obtained from the derived interatomic potentials, with the other calculated and experimental values.

Method	Parameter *a (Å)*
Potential Model (This Work)	5.931
ABINIT [a]	5.93
VASP (LDA) [b]	5.966

[114][a] [115][b]

Table 15 shows a comparison of the elastic properties of Li_2S we calculated using DFT methods (VASP code) and those calculated from our derived interatomic potentials employing the GULP and METADISE codes; experimental elastic constants are available for Li_2S. The elastic constants from the interatomic potentials are in good agreement with those from DFT calculations, together with the various moduli of elasticity, i.e. the bulk, shear, elasticity moduli and Poisson's ratio. In addition, the Li_2S phase has elastic constants that satisfy the generalized elastic stability criteria for cubic crystals [108] [109]:

$$\begin{aligned} &(C_{11} - C_{12}) > 0, \\ &C_{11} + 2C_{12} > 0, \\ &C_{44} > 0 \end{aligned} \tag{3.23}$$

Table 15: Calculated elastic constants and moduli of the Li_2Se phase.

Elastic Properties	Observable (VASP)	GULP (Fitted)
C_{11}	66.78	69.36
C_{12}	17.70	16.62
C_{44}	29.91	24.12
Bulk Modulus, *B* (GPa)	34.06	33.90

4.4.2. Phonon Dispersions and Density of States of Li_2S and Li_2Se.

Phonons play a major role in many of the physical properties of solids, including a material's thermal and electrical conductivities. They are a quantum mechanical description of a special type of vibrational motion, in which a lattice uniformly oscillates at the same frequency. In classical mechanics this is known as normal mode [114]. Phonon calculations are exact at the zone centre for a single unit cell and for a supercell composed of more unit cells at the wave vectors commensurate with the supercell. In practice, a phonon calculation is converged if the force constants between an atom at the centre of the supercell and those at the cell boundaries are effectively zero.

The phonon calculations of Li_2S and Li_2Se cubic phases were executed using the VASP code. This density functional calculation uses the Perdew-Burke-Emzerhot (PBE) Generalized Gradient Approximation (GGA) for the exchange correlation functional. All atoms were described with pseudopotentials taken from the VASP library and developed on plane waves basis sets using the Projector Augmented Wave (PAW) method**.**

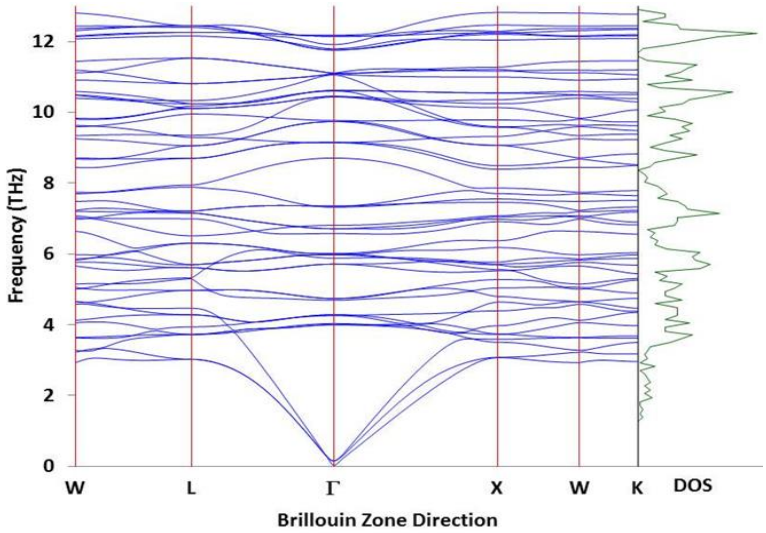

Figure 23: Phonon DOS and dispersion curve of Li_2Se phase.

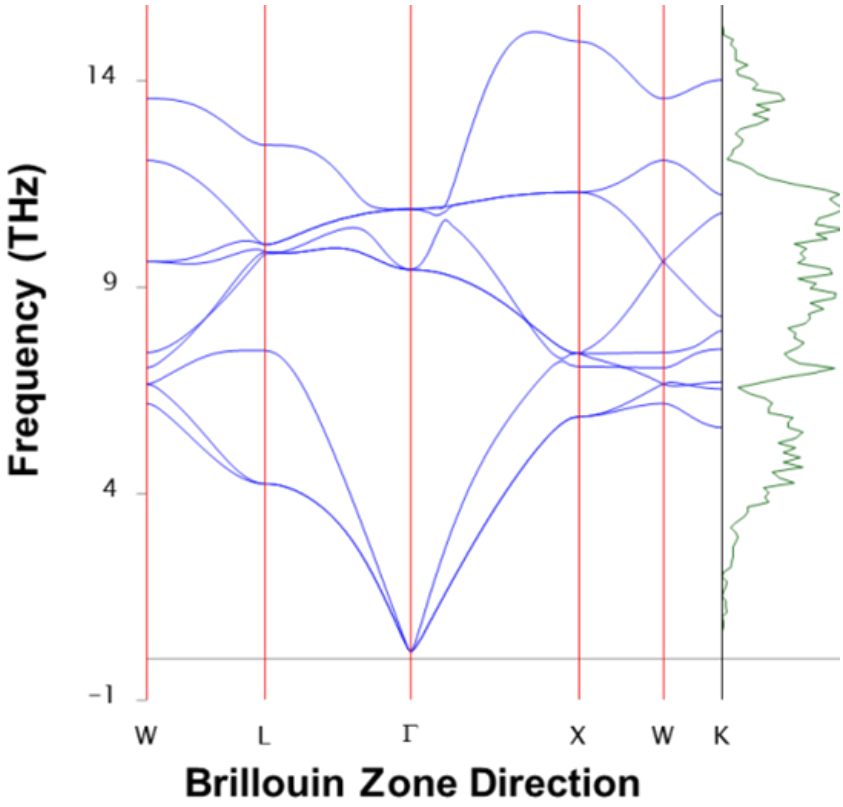

Figure 24: Phonon DOS and dispersion curve of Li_2S phase.

Figures 23 and 24 above shows the phonon dispersion curve and the total density of states (DOS) of the Li_2S and Li_2Se phases which allude to the stability of the system. This is deduced from all phonon branches lying above 0 THz, implying that there are no soft modes encountered along high symmetry directions. This is an indication that the Li_2S and Li_2Se phases are stable. Which is an important factor for the next generations of rechargeable lithium batteries for the discharge products formed to be stable. Both Li_2S and Li_2Se are the discharge products formed in Li/S and Li/Se batteries which are considered for future energy storage.

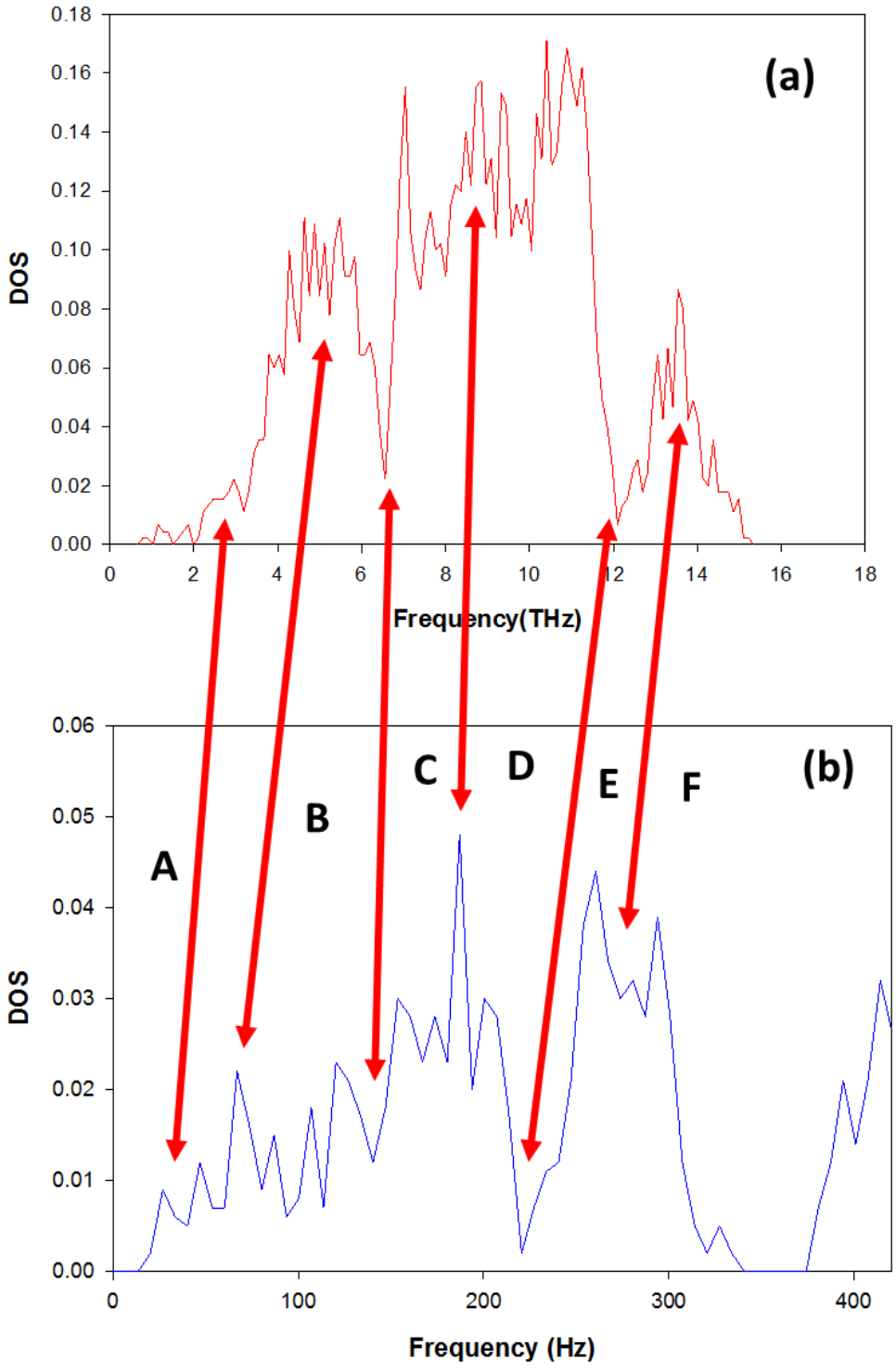

Figure 25 : A comparison of the total phonon densities of states (DOS) of Li_2S calculated using a) first principle method with the VASP code and b) our derived interatomic potentials using the GULP program

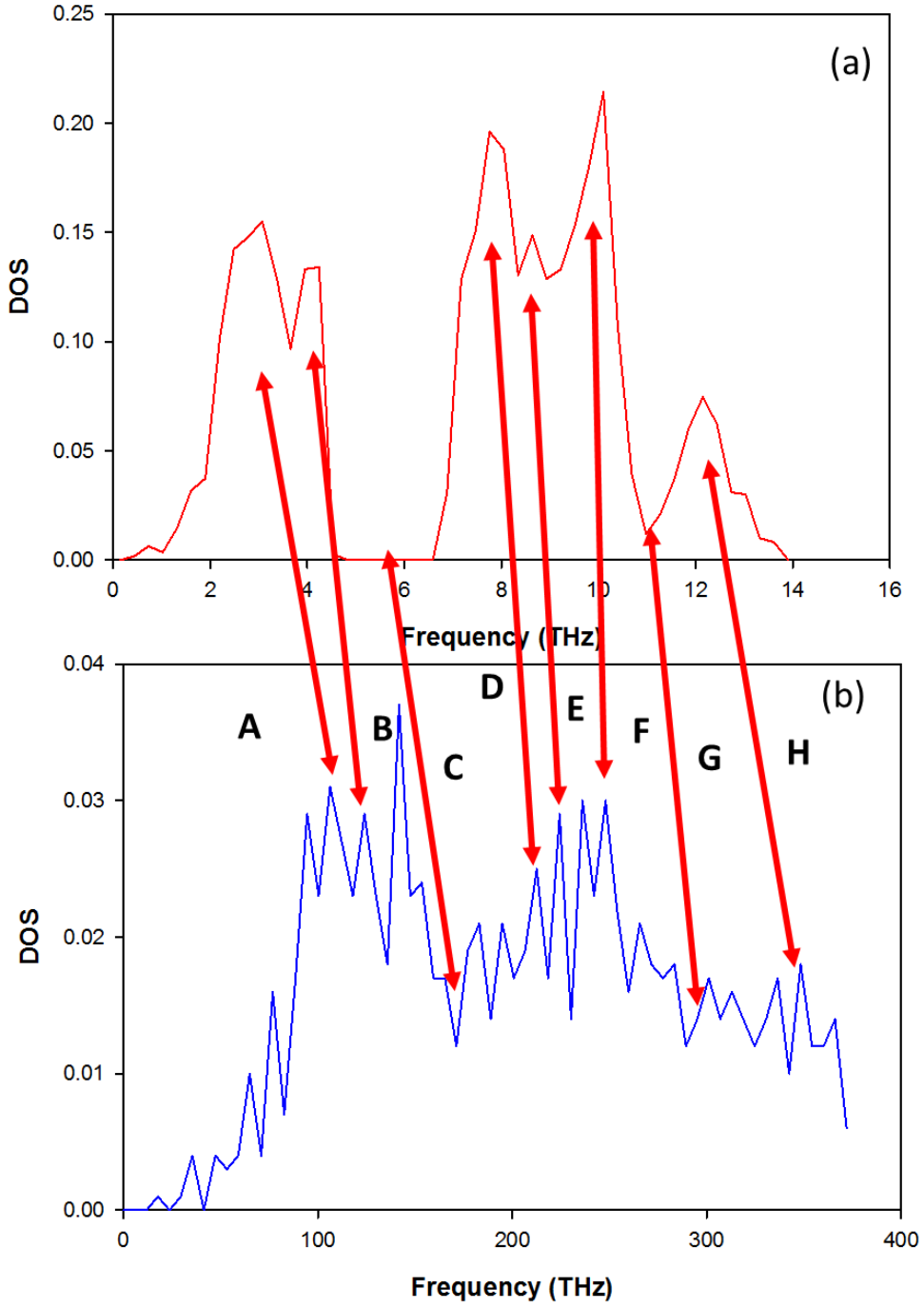

Figure 26 : A comparison of the total phonon densities of states (DOS) of Li_2Se calculated using a) first principle method with the VASP code and b) our derived interatomic potentials using the GULP program

The total phonon density of states of Li_2S and Li_2Se, calculated quantum mechanically by the VASP code, is given in Figure 25 and 26 and is compared with that determined by the GULP code using our derived interatomic potentials. Although not all finer details are reproduced, some features such as distinct peaks of the densities of states from the two methods, marked A to H can be correlated in both Li_2S and Li_2Se. Some differences are noted especially with intensities of DOS peaks. Larger K point grids in GULP calculations could not improve the correspondence of the DOS from the two codes. Hence the differences can be ascribed to the simulation of our potential model. The difference in the frequency regimes of the comparison could be due to A- parameter of the derived interatomic potentials but the future work will be on modifying this parameters.

4.4.3. X-Ray Diffraction Pattern

The consistency of our potential model was also demonstrated by the X-ray Diffraction (XRD) patterns compared with the experimental findings [21] [116]. Figure 27 shows XRD patterns of both Li_2S and Li_2Se for this work and X-Ray Diffraction patterns from the literature.

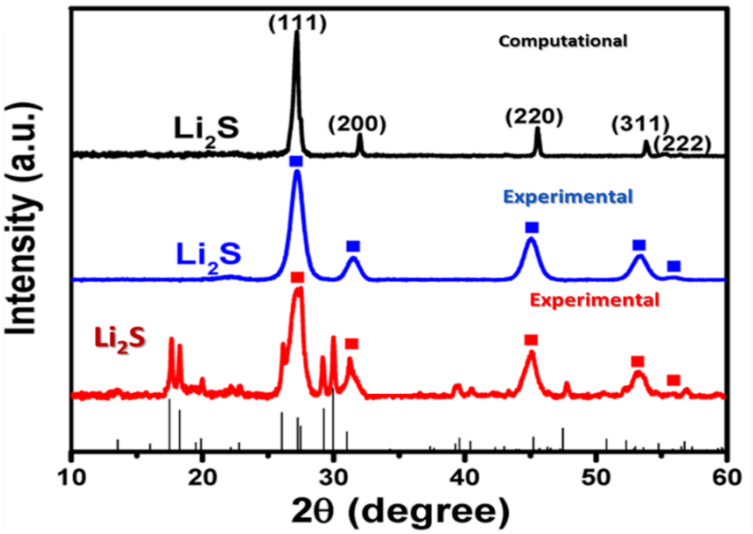

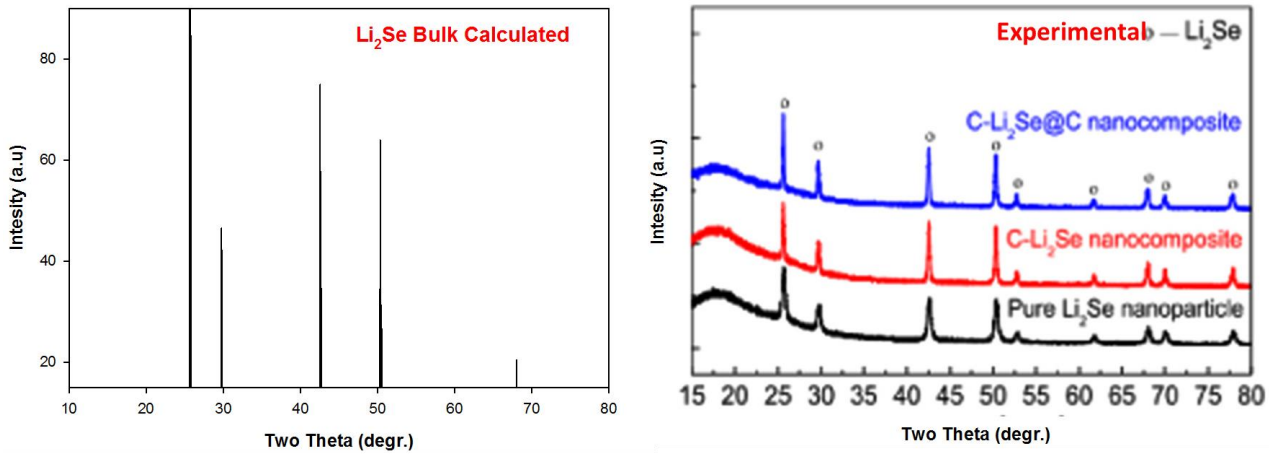

Figure 27: X-Ray diffraction patterns of Li_2S and Li_2Se bulk structure for a) this work and b) experimental

In summary, our new derived interatomic potential model is able to simulate and reproduce the structure and elastic properties of Li_2S and Li_2Se phases, to within smaller percentage of other calculated and the available experimental results. The potentials are good, as the calculation of DOS is a stringent test. Its strength has been mainly demonstrated by its good performance on structural and mechanical properties, and as will be shown in the next section using Molecular Dynamics code, i.e. DL_POLY, its

accurate reproduction of high temperature bulk properties effects. This far exceeds what is normally required of models in literature. However the reason to why certain experimental details are not well reproduced by the current computational approach could be that the potential models need further refining as this it's the first study of this kind on this materials.

4.5. Atomistic Potentials Different Sets for Li_2S and Li_2Se

In this section we present further results on potentials models derivation and validation. This very much required as it will reveal clear reason to why the set of potential models selected in above section. It will furthermore assist to show how the value A –parameter have an impact on the final calculations of the molecular dynamics which are in the next sections. Further sets of potential models for Li_2S (MC2 and MC3) were derived and validated together Li_2Se sets (MC*2 and MC*3).

4.5.1. Atomistic Potentials Different Set for Li_2S

4.5.1.1. Structural, Elastic Properties and Potentials Models for Set 2-MC2 and Set 3 –MC3.

Table 16 : Comparison of the lattice parameter of Li_2S, obtained from the derived interatomic potentials, with the other calculated and experimental values (MC2).

Method	Parameter *a (Å)*
Potential Model (This Work)	5.72
VASP (GGA-PBE)[a]	5.71
Experimental [a]	5.708
Theoretical [b]	5.715

Table 17 : Calculated elastic constants and moduli of the Li_2S phase (MC2).

Elastic Properties	Observable (GGA) [117]	GULP (Fitted)
C_{11}	83.90	84.50
C_{12}	18.10	8.73
C_{44}	34.20	30.47
Bulk Modulus, *B* (GPa)	40.08	35.00

[117][a] [113][b]

Table 18 : Set 2 (MC2) Interatomic potential parameters for the Li_2S as derived in the present study.

Species	Charge *(e)*			
Lithium (Li)	0.50			
Sulphur (S)	-1.00			
Buckingham Potentials	*A (eV)*	*ρ (Å)*	*C(eV /Å^6)*	*Cut-off(Å)*
Li core – Li core	1200.2	0.2000000	0.000	20
Li core – S core	1549955.3	0.132724	3.000	10
S core – S core	26025.137	0.316293	32.000	10

Three-body	K_b (eV/rad^2)	$\theta_0{}^0$
Li core S core S core	3.5412	109.503000
S core Li core Li core	0.69400	199.730369

Table 19 : Comparison of the lattice parameter of Li_2S, obtained from the derived interatomic potentials, with the other calculated and experimental values (MC3).

Method	Parameter *a (Å)*
Potential Model (This Work)	5.708
VASP (GGA-PBE)[a]	5.71
Experimental [a]	5.708
Theoretical [b]	5.715

[117][a] [113][b]

Table 20 : Calculated elastic constants and moduli of the Li_2S phase (MC3).

Elastic Properties	Observable (GGA) [117]	GULP(Fitted)
C_{11}	83.90	84.20
C_{12}	18.10	2.10
C_{44}	34.20	30.43
Bulk Modulus, *B* (GPa)	40.08	33.00

Table 21 : Set 3 (MC3) Interatomic potential parameters for the Li_2S as derived in the present study.

Species	Charge *(e)*			
Lithium (Li)	0.50			
Sulphur (S)	-1.00			
Buckingham Potentials	*A (eV)*	*ρ (Å)*	*C(eV /Å^6)*	*Cut-off(Å)*
Li core – Li core	1200.2	0.2000000	0.000	20
Li core – S core	154995.3	0.132724	3.000	10
S core – S core	21141.0	0.30857	32.000	10

Three-body	K_b (eV/rad^2)	$\theta_0{}^0$
Li core S core S core	3.5412	109.503000
S core Li core Li core	0.69400	199.730369

4.5.2. Atomistic Potentials Different Set for Li_2Se

4.5.2.1. Structural, Elastic Properties and Potentials Models for Set 2- MC*2 and Set 3 –MC*3.

Table 22 : Comparison of the lattice parameter of Li_2Se, obtained from the derived interatomic potentials, with the other calculated and experimental values (MC*2).

Method	Parameter *a (Å)*
Potential Model (This Work)	5.98
ABINIT [a]	5.93
VASP (LDA) [b]	5.966

[114][a] [115][b]

Table 23 : Calculated elastic constants and moduli of the Li_2Se phase (MC*2).

Elastic Properties	Observable (VASP)	GULP (Fitted)
C_{11}	61.42	56.00
C_{12}	25.36	26.34
C_{44}	22.38	23.45
Bulk Modulus, *B* (GPa)	37.38	36.22

Table 24 : Set 2 (MC*2) Interatomic potential parameters for the Li_2Se as derived in the present study.

Species	Charge *(e)*			
Lithium (Li)	0.50			
Selenium (Se)	-1.00			
Buckingham Potentials	*A (eV)*	*ρ (Å)*	*C(eV /Å^6)*	*Cut-off(Å)*
Li core – Li core	1200.00	0.2000	20.000	20
Li core – Se core	91718320.00	0.116224	30.000	10
Se core – Se core	21141.0	0.324604	22.000	10

Three-body	K_b (eV/rad^2)	$\theta_0{}^0$
Li core Se core Se core	3.5412	250.503000
Se core Li core Li core	0.69400	99.730369

Table 25 : Comparison of the lattice parameter of Li_2Se, obtained from the derived interatomic potentials, with the other calculated and experimental values (MC*3).

Method	Parameter *a (Å)*
Potential Model (This Work)	6.02
GGA (This Work)	6.01
ABINIT [a]	5.93
VASP (LDA) [b]	5.966

[114][a] [115][b]

Table 26 : Calculated elastic constants and moduli of the Li_2Se phase (MC*3).

Elastic Properties	Observable (VASP)	GULP (Fitted)
C_{11}	61.42	52.00
C_{12}	25.36	23.00
C_{44}	22.38	21.99
Bulk Modulus, *B* (GPa)	37.38	33.22

Table 27 : Set 3 (MC*3) Interatomic potential parameters for the Li_2Se as derived in the present study.

Species	Charge *(e)*			
Lithium (Li)	0.50			
Sulphur (Se)	-1.00			
Buckingham Potentials	*A (eV)*	*ρ (Å)*	*C(eV /Å^6)*	*Cut-off(Å)*
Li core – Li core	1200.00	0.2000	20.000	20
Li core – Se core	917183.00	0.150134	30.000	10
Se core – Se core	174201.00	0.276356	22.000	10

Three-body	K_b (eV/rad^2)	$\theta_0{}^0$
Li core Se core Se core	3.5412	250.503000
Se core Li core Li core	0.69400	99.730369

4.6. MD Study of Li_2S and Li_2Se

Molecular dynamics (MD) is a key theoretical tool in understanding microstructural, dynamic and thermal effects in various systems at the atomistic level. Modern simulations with millions of atoms can investigate collective phenomena, such as melting and phase transitions. The key factors in atomistic molecular dynamics are the interatomic potentials, which determine the forces on the atom [118]. Atomistic MD calculations form an effective simulation method for investigating systems consisting of a large number of atoms and it provides dynamical information on atomic positions and velocities at the various simulation time steps [119]. In addition, molecular dynamics (MD) method is a powerful and effective tool to study the physical characteristics of micro/nanostructure [120]. Hence we will use MD to study the nanostructures later in the thesis. In this chapter we use the derived interatomic

potentials of Li_2S and Li_2Se, to study the temperature effects on bulk structures using molecular dynamics technique. The bulk properties such as lattice parameter, interatomic distances, and elastic constants are calculated using energy minimisation technique. The following properties; radial distribution functions (RDFs), diffusion coefficients and mean squared displacements (MSD); will depict changes induced by temperature.

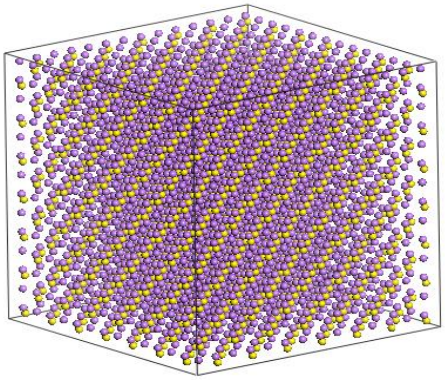

Figure 28: The 5x5x5 supercell of Li_2S bulk structure used in the MD calculations.

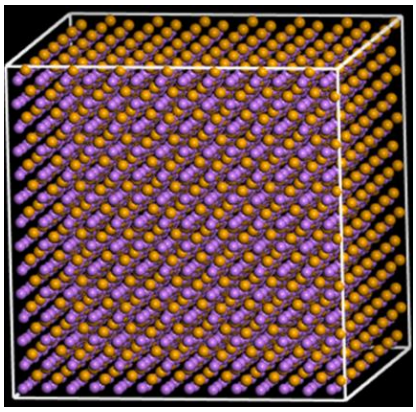

Figure 29: The 5x5x5 supercell of Li_2Se bulk structure used in the MD calculations.

One of the mechanisms of checking the melting temperature of bulk structures is the variation energy with respect to temperature using molecular dynamics method. Figures 30 and 31 shows the graphs of total energy against the temperature and the energy change between 300 K and 1100 K is near linear; however, after 1100 K there is a slight deviation from linearity. This could be attributed to the phase change of Li_2S and Li_2Se. We notice a further very significant change in energy at 1300 K. This indicates that there is a phase transition from solid phase to a liquid phase from 1300 K.

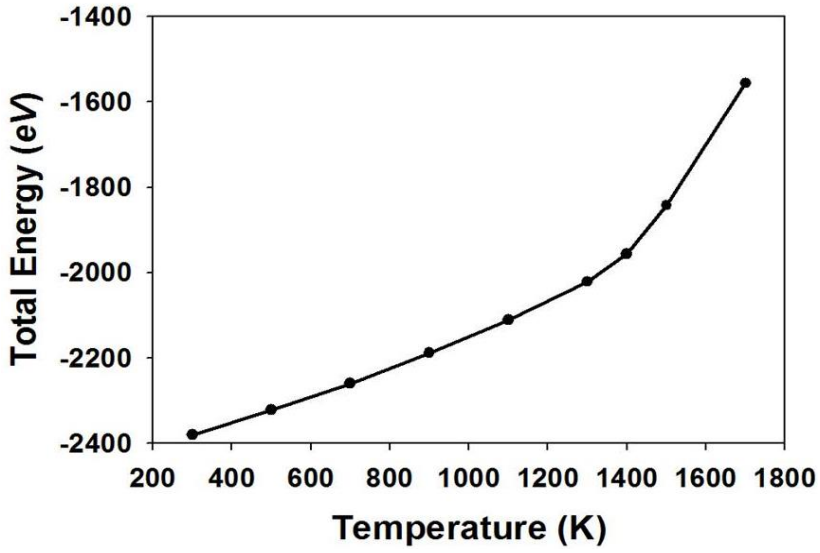

Figure 30: The total energy variation with temperature for Li_2S bulk structure.

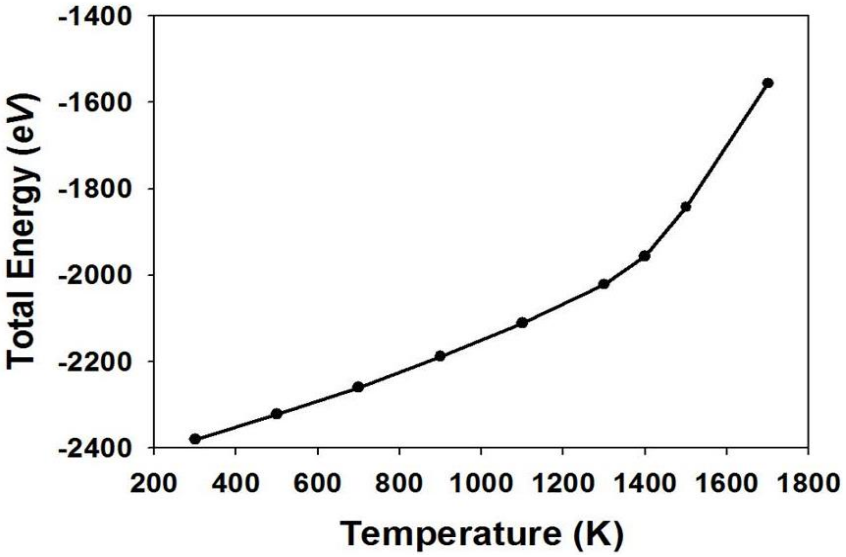

Figure 31: The total energy variation with temperature for Li_2Se bulk structure.

Figure 30 and 31 shows the graphs of total energy against the temperature at different temperatures, from 1000K K to 1300 K with the increment of 200 K. From the radial distribution function plots we observe that at lower temperatures of 1000 K there are several sharp peaks, implying a well-defined structure. However, as we increase the temperature the peaks become broader and their number decreases, showing that the structure is experiencing the phase transition from a solid phase to a liquid phase especially

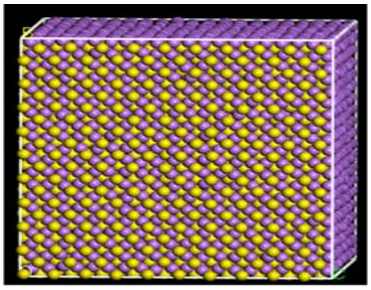

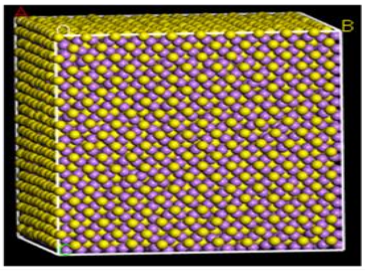

300K

600K

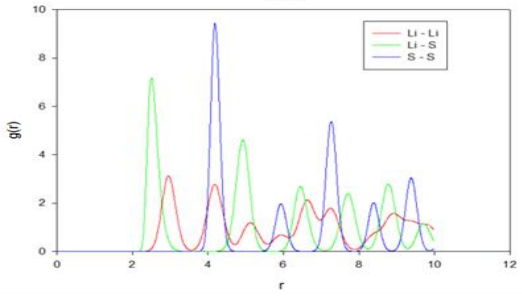

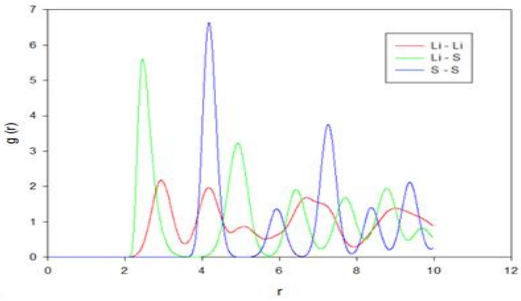

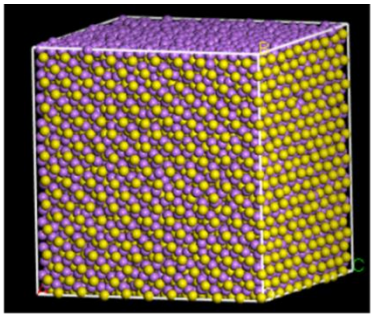

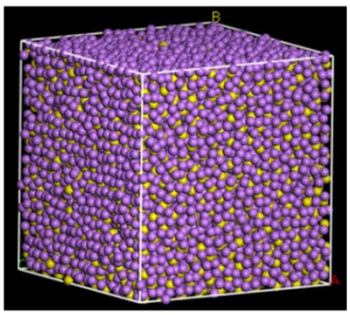

900K

1300K

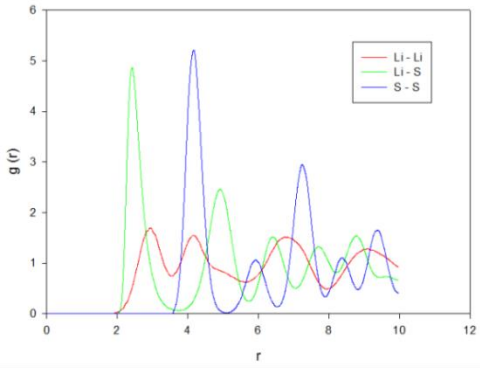

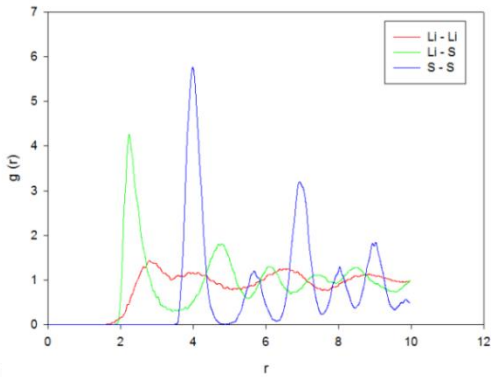

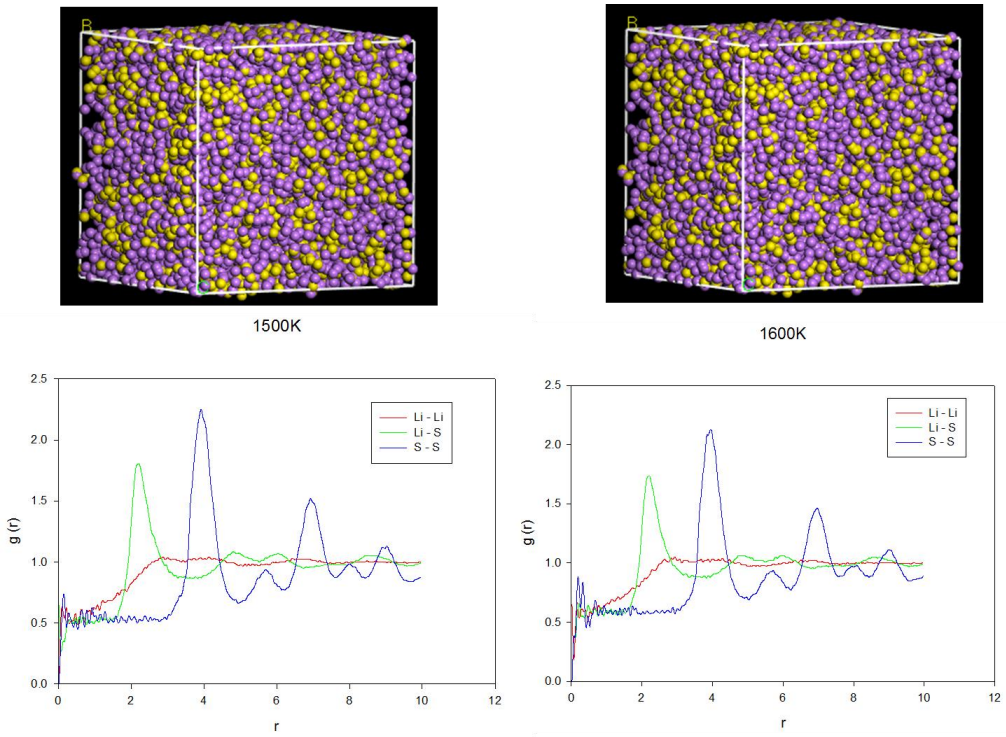

Figure 32: Radial distribution functions of the Li_2S bulk structure at different temperatures.

In order to demonstrate the phase changes of the Li_2S structure, we show all the RDFs and snapshots of the bulk structures at different temperatures in figure 32. Similar study was performed by Mjwara *et.al* (1991) [121] utilizing brillouin scattering to investigate the high temperature diffuse phase transition, which is basically what we aim for using molecular dynamics with derived interatomic potentials.

The RDFs indicate that as the temperature increases, the peaks become broader and the number of peaks decreased. Furthermore, the total RDFs show that between 300 and 900 K, the second and third peaks are well-defined. However, at 1300 K the peaks collapses. This is the temperature range where Li_2S undergoes phase change from normal to high form. Indeed our simulations (Figure 32) confirm the molten phase at

1300 K, since the height of the coalesced peak is reduced, which is further in agreement with the total energy versus temperature (Figure 31) anomalous enhancement above 1200 K. At a higher temperature of 1500 K the height of the coalesced peak is further reduced showing a completely molten structure.

In addition, from the pictures we observe that there is a phase transition from a lower temperature to a higher temperature. At 300 K the structure is still intact and crystalline. However, as we increase the temperature in steps of 100K up to 1500 K, we observe that the structure loses its crystallinity, from 1300 K, as the regular arrangement of atoms disappears. At 1300 K the arrangement of atoms has completely disappeared. This is in further support of the high temperature proposition put forward by the results of the radial distribution functions and the total energy.

Similar has been observed on the figure 33 below on the study of Li_2Se, there is no much study done on this materials though. However we have noticed that the RDFs indicate that as the temperature increases, the peaks become broader and the number of peaks decreased. Furthermore, the total RDFs show that between 300 and 900 K, the second and third peaks are well-defined. However, at 1300 K the peaks collapses. This is the temperature range where Li_2Se undergoes phase change from normal to high form. Indeed our simulations (Figure 33) confirm the molten phase at 1300 K, since the height of the coalesced peak is reduced, which is further in agreement with the total energy versus temperature (Figure 31) anomalous enhancement above 1200 K. At a higher temperature of 1500 K the height of the coalesced peak is further reduced showing a completely molten structure.

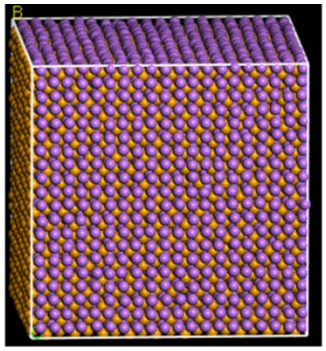

300K

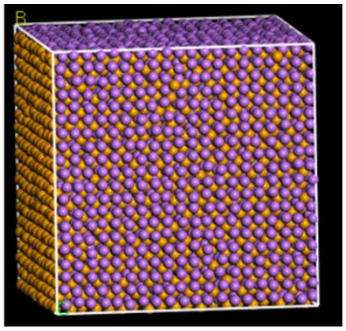

600K

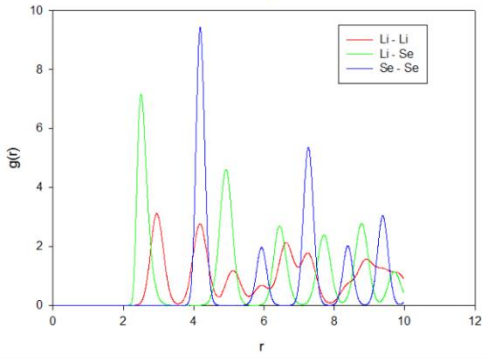

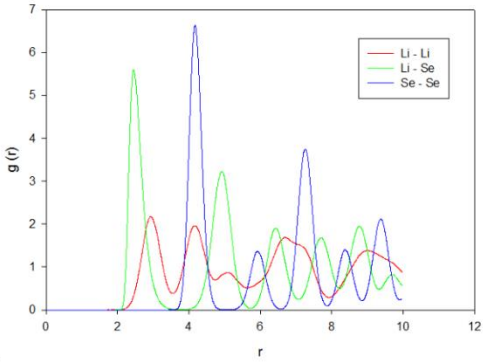

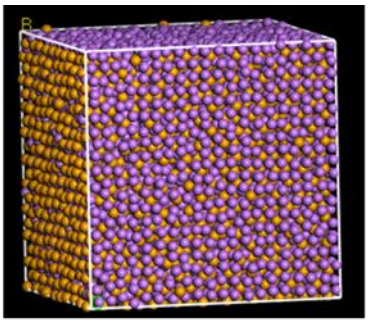

900K

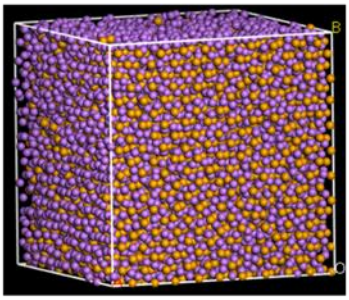

1300K

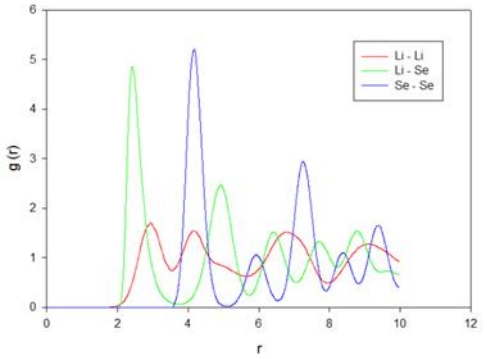

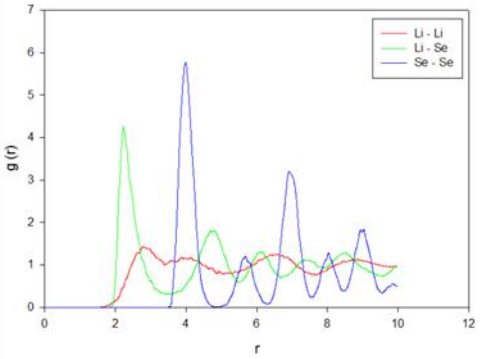

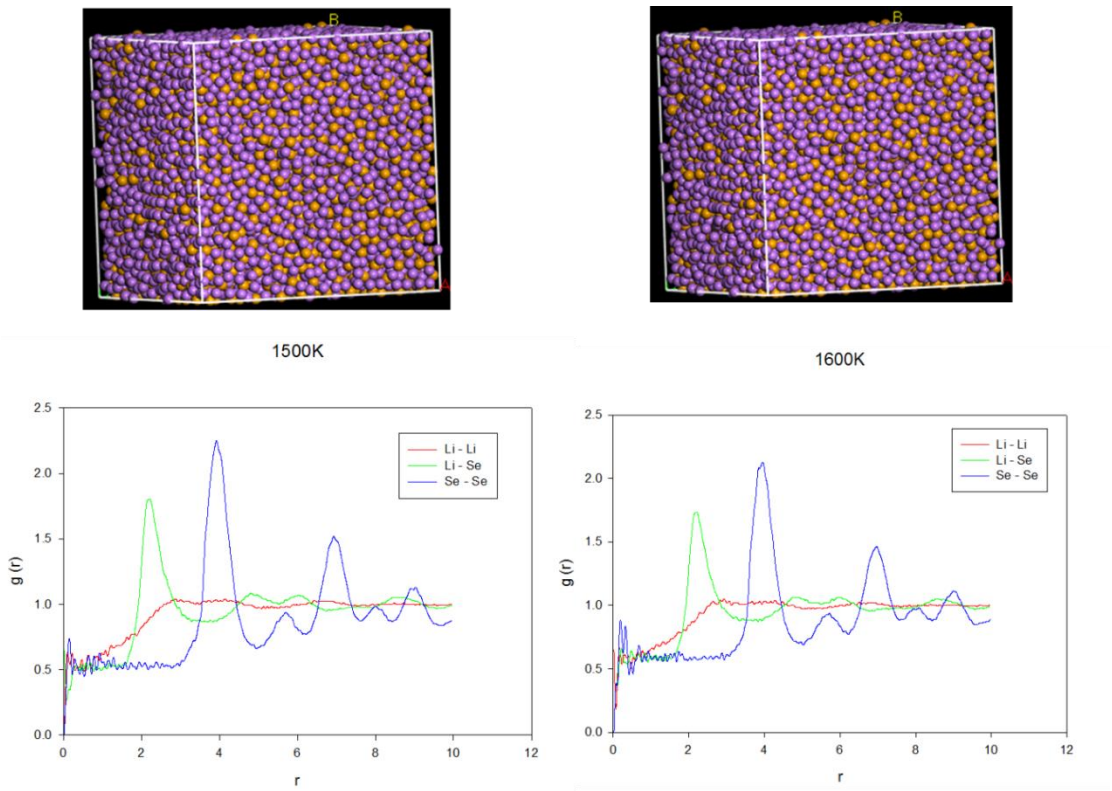

Figure 33: Radial distribution functions of the Li_2Se bulk structure at different temperatures.

4.7. MD Study of Li_2S and Li_2Se Using MC and MC* Potential Models.

4.7.1. MD Study of Li_2S

Atomistic potential models for 2 sets MC2 and MC3 derived in chapter 4 section 4.5 were tested in molecular dynamics. The sets were derived to check the a the huge change of *A- parameter* from all the change rapidly to a big value has any impact on the MD calculations which indeed it was found the change a *A- parameter* has an impact on the calculations hence the structure Li_2S collapse at low temperature.

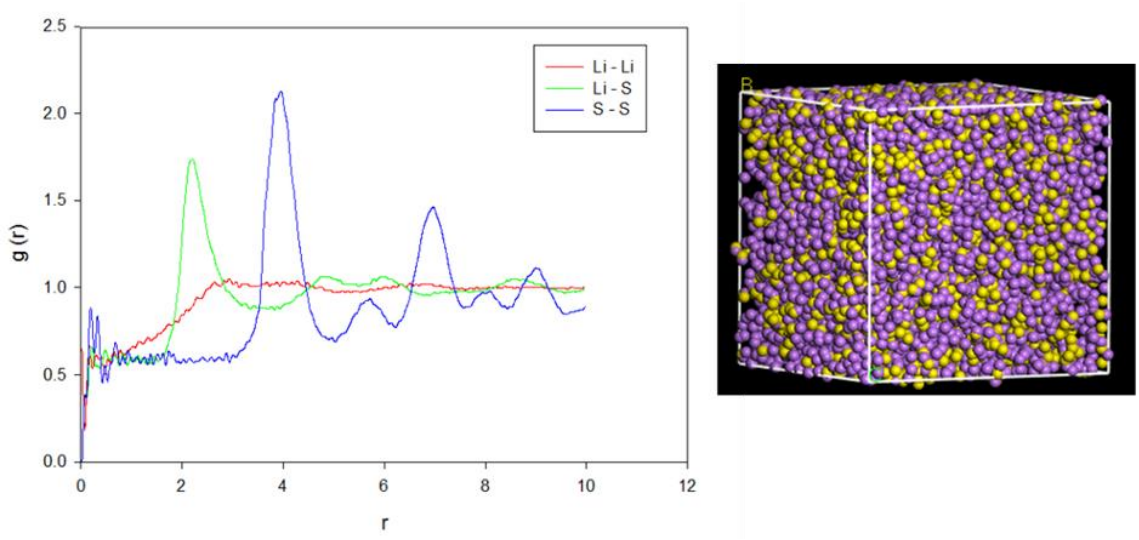

Figure 34: Radial distribution functions of the Li_2S bulk structure at 300K.

4.7.2. MD Study of Li_2Se

Atomistic potential models for 2 sets MC*2 and MC*3 derived in chapter 4 section 4.5 were tested in molecular dynamics. The sets were derived to check the a the huge change of *A- parameter* from all the change rapidly to a big value has any impact on the MD calculations which indeed it was found the change a *A- parameter* has an impact on the calculations hence the structure Li_2Se collapse at low temperature.

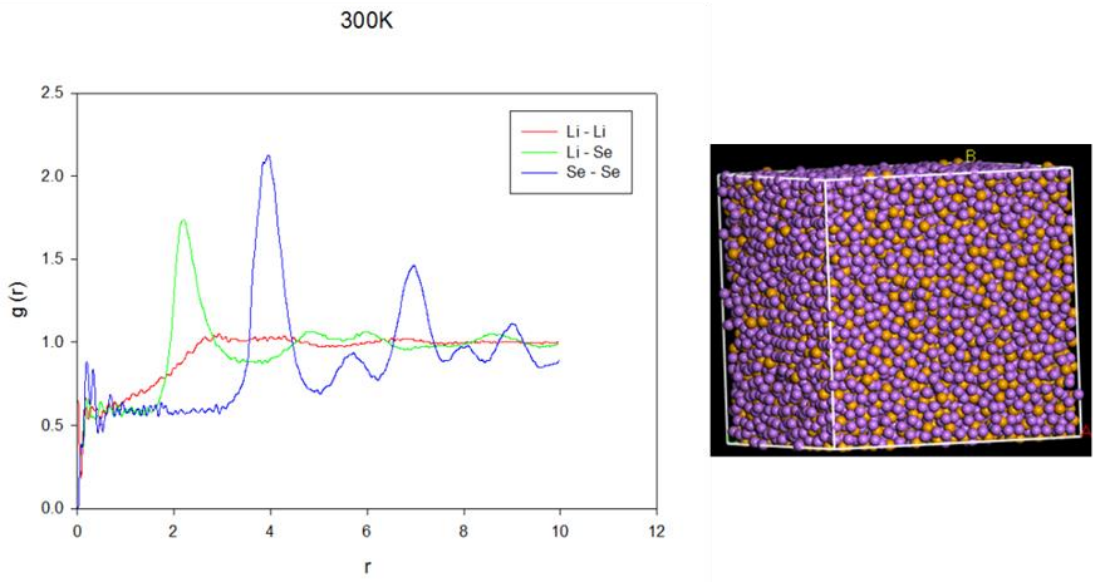

Figure 35 : Radial distribution functions of the Li2Se bulk structure at 300K.

4.8. Discussions

Currently, most Li_2S and Li_2Se computational modelling studies are based on first principles density functional theory methods, which whilst more accurate tend to be limited to smaller systems and do not adequately accommodate thermal effects. In order to address such concerns, the first empirical interatomic potentials for the Li_2S and Li_2Se structures were derived in the present study; a task that poses challenges in the classical simulation methods and is critical to their success [47]. The attention is initially focussed on the binaries, Li_2S and Li_2Se since they are more amenable to computational methods. Several experimental structural, elastic and lattice dynamics properties, which are key for fitting potentials, were scarce or not available, hence they were calculated, in the present study, by DFT methods. The derived interatomic potentials of Li_2S and Li_2Se were adequately validated, in the bulk form, as evidenced by their accurate determination of structure, elastic constants and moduli and phonon density of states; which indeed compare well with to those obtained by experiment [122] or DFT methods or DFT methods.

The robustness of the interatomic potentials was further illustrated by their ability to reproduce complex high temperature transitions of the bulk Li_2S and Li_2Se which were observed experimentally from Brillouin scattering [123] and lattice dynamics [124] methods, and DFT molecular dynamics [125]. The change in total energy with temperature (further explanation and estimates of transition temp) and radial distribution functions, deduced from molecular dynamics studies, clearly depicted the phase change from normal to high form above 1100K. Furthermore, the potentials of the bulk Li_2S and Li_2Se show melting at 1300K, as demonstrated by calculated rdfs and energy; all consistent with the experimental results. However, the stiffnesses on Li-S

and S-S interactions were noted from calculated rdfs. Successful employment of interatomic potentials in studies of large systems has been clearly demonstrated in metal sulphides such as FeS_2, where high temperature properties were also reproduced [49]. In addition, complex nano-architectures including nanospheres, nanoporous, nanorods, were generated from metal sulphide empirical potentials such as ZnS [126], similarly to what was done for TiO_2 [48] and MnO_2 [50] amongst others. Hence similar phenomena and structures can be generated with interatomic potentials of Li_2S and Li_2Se.

Chapter 5: Cluster Expansions and Monte-Carlo Simulations for Li-S-Se System

The discovery of new electrode materials is key to realizing safe and efficient electrochemical energy storage systems essential to enabling future green energy technologies. Beyond conventional intercalation chemistry, reaction of lithium with sulphur and oxygen have the potential to provide 2 to 5 times the energy density of current commercial systems [16]. However, both Li/S and Li/O systems suffer from cycling performance issues that impede their commercial applications: Li/O cycling is limited by electrolyte decomposition and large cell polarization; Li/S suffers from the low conductivity of S and the solubility of intermediary polysulfide species during cycling [17].

Here we explore the potential of selenium, a d-electron containing member of group 16 elements of periodic table with high electrical conductivity, as an electrode material for rechargeable batteries. We show that Se and mixed SexSy represent an attractive new class of cathode materials with promising electrochemical performance in reactions with Li ions using cluster expansion and Monte Carlo simulation techniques.

5.1. The Cluster Expansion

Modern DFT methods are able to calculate material properties with reasonable to high precision (depending on the quality of the approximations to the exchange and correlation effects). Standard DFT applications are, however, restricted to unit cells of a few hundreds of atoms. If one wants to model an alloy with varying atomic concentrations and crystal structures a huge number of very large supercells would be

needed, if one tries to solve this problem in a brute force way. Such a procedure is, of course, not feasible. A successful strategy to overcome this limitation is offered by the cluster expansion (CE) [127] in particular when combined with Monte Carlo simulations.

The concept of CE is to describe every configuration dependent property of a system by a linear combination of interacting building blocks or figures. By configuration one understands a distribution of atoms over a given lattice. Then the energy for a given con-figuration σ is written as a sum over pairs, tripletts, quadruplets, and so on, the so-called *figures* or *clusters*. It was shown [127] that such an expansion exists if – mathematically–the expansion goes over all configurations (i.e. atomic distributions). For practical reasons the expansion has to be limited to reasonably small clusters, so that the expansion converges numerically. If the input of a convergent cluster expansion is provided by DFT calculations, then the accuracy of DFT calculations can be carried over to systems consisting of 104−106 atoms. Many studies were made for binary bulk systems (e.g. [128] [129] [130]

5.1.1. Basic Principles of the Cluster Expansion

From an optimized cluster expansion, a set of effective cluster interactions can be extracted and used in large-scale Monte Carlo simulations to explore order-disorder phenomena and phase segregation processes as a function of temperature.

On a basic lattice various atoms, for example of type A and B, are distributed to define structure σ, a periodic configuration of A and B atoms. This configuration is described by the pseudo spin operator σ_q =+-1, which has the value +1 if atom A sits on site q or -1 if that atom is B.

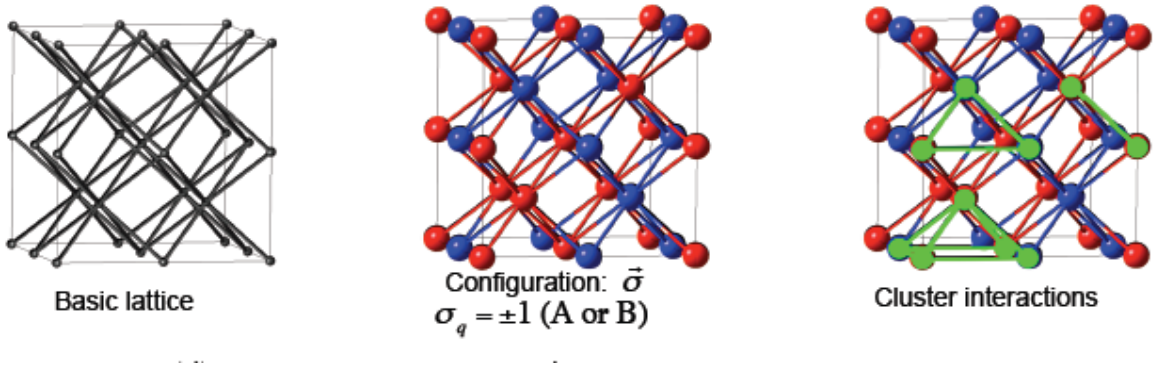

The energy (σ) associated with structure σ can be described by an expansion of cluster interactions and their respective interaction energies J by means of equation

$$E(\vec{\sigma}) = J_0 + J_1 \sum_i \sigma_i + \sum_{i>j} J_{ij}\sigma_i\sigma_j + \sum_{i>j>k} J_{ijk}\sigma_i\sigma_j\sigma_k + \cdots$$

In this equation J_0, the first term, describes a constant, configuration independent contribution. The second term is concentration dependent and is a sum over all N sites of structure σ with onsite energy J_1 times the pseudo spin operator σ at each site i. Further terms describe the cluster interactions between multiple sites, for example two-body interactions J_{ij} or three-body interaction J_{ijk}. They contain spin products $\sigma_i\sigma_j \ldots$ over all f vertices of a cluster times its effective cluster interaction energy $J_{ij\ldots}$ summed up over all the possible ways that the cluster can be placed on the lattice of structure σ. In other words, the energy (σ) of structure σ is broken down into clusters with their associated effective interaction energies. The core issue of cluster expansion is to identify a universal set of interactions J best-suited to describe a given model. To accomplish this it is useful to reformulate above equation into the more compact form

$$E(\vec{\sigma}) = \sum_{C \epsilon \vec{C}} J_C \, \Pi_C(\vec{\sigma})$$

The cluster expansion equation sums up the product of cluster C's interaction energy J_C with its correlation function,

$$\Pi_C(\vec{\sigma}) = N^{-1} \sum_{i=1}^{N} \sum_{k \in C} \prod_{v \epsilon \vec{f}} \sigma_v$$

a sum over all the possible ways a cluster C with $\vec{f}$ vertices can be placed on the N sites of the structure. In the correlation function the spin product $\sigma_1 \ldots \sigma_f$ goes over all f vertices of the cluster. Only symmetry inequivalent clusters are now considered and clusters included in an expansion can be collected by the vector $C = \{C_1, \ldots, C_n\}$.

5.1.2. The UNCLE-Code

All the CE calculations of the present work were done by making use of the program package UNiversal CLuster-Expansion (UNCLE) [131] which was developed by the group of S. Muller, now at the Technical Univeristy of Harburg-Hamburg. The code is able to perform a complete CE fit using a genetic algorithm and to predict the ground states of systems containing up to three and more elements. For deriving results for temperatures T= 0 Monte Carlo simulations are implemented. By this, configurational entropies are taken into account. The working scheme for a cluster expansion is sketched in figure

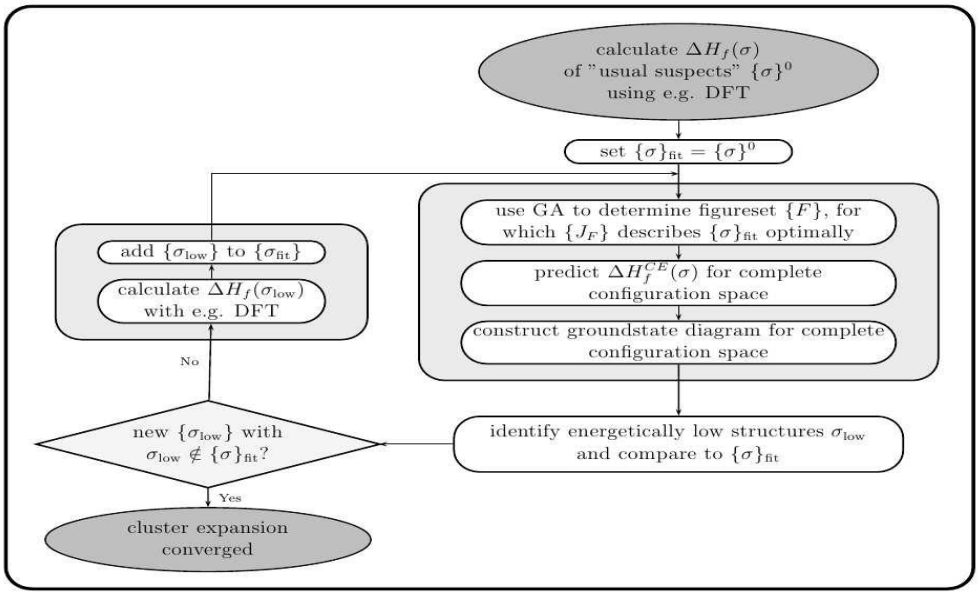

Figure 36 : Self-consistent working plan as used by UNCLE for the cluster expansion for finding new input structures [131]

5.1.3. Selecting the Input Structures

A very important task of a convergent CE is to guarantee that the figures and associated effective interaction energies that are chosen are not biased by the training set. To prevent a wrong interpretation of the whole system by choosing the wrong input, UNCLE uses the chosen figure set to fit the energy of other structures. New structures can now be designed and if they lie energetically below the existing ground state line they are recalculated by DFT, providing a new set of input structures. Then, a new set of figures is fitted and the procedure repeated. Such an iterative approach has the advantage that a reliable ground state line can be achieved together with a figure set which yields accurate results.

5.1.4. Genetic Algorithm

A minimization using genetic algorithm was first used for the CE by Hart et al. [132]. In this approach the figure list is represented as a binary string. A figure used is marked by the value 1, otherwise the value is 0. Furthermore, the interaction energies are also represented as a binary string. The combination of both binary strings, including figures used and their interaction energies, is now the genetic 'DNA' of a solution, who's fitness is described by the CVS. A higher CVS compared to other solutions means, that this solution has a lower fitness.

Now, a 'population' of n_{pop} different solutions is created, in which the fitness of every individual solution is calculated. Of those n_{pop} individuals only the fittest n_{fit} ($0 < n_{fit} < n_{pop}$) individuals are selected to survive to the next iteration process. The other $n_{pop} - n_{fit}$ solutions are replaced by 'descendants' of the surviving fittest 'parent' solutions. Their 'DNA' is created by two different processes as sketched in Fig. 37:

• In crossover, the 'DNA' of the 'offspring' is created by mixing the 'DNA' of two randomly selected 'parent' solution. Thereby the 'DNA' of one 'parent' solution is used up to the crossover point. After that point the 'DNA' of the second 'parent' is used.

• In mutation, a random binary bit of the 'DNA' string is flipped from one state to the other, i.e. $1 \Rightarrow 0$ or $0 \Rightarrow 1$.

Note, that one may replace all surviving 'parent' solutions with the 'children', as long as only the fittest 'parent' solutions are used to create them.

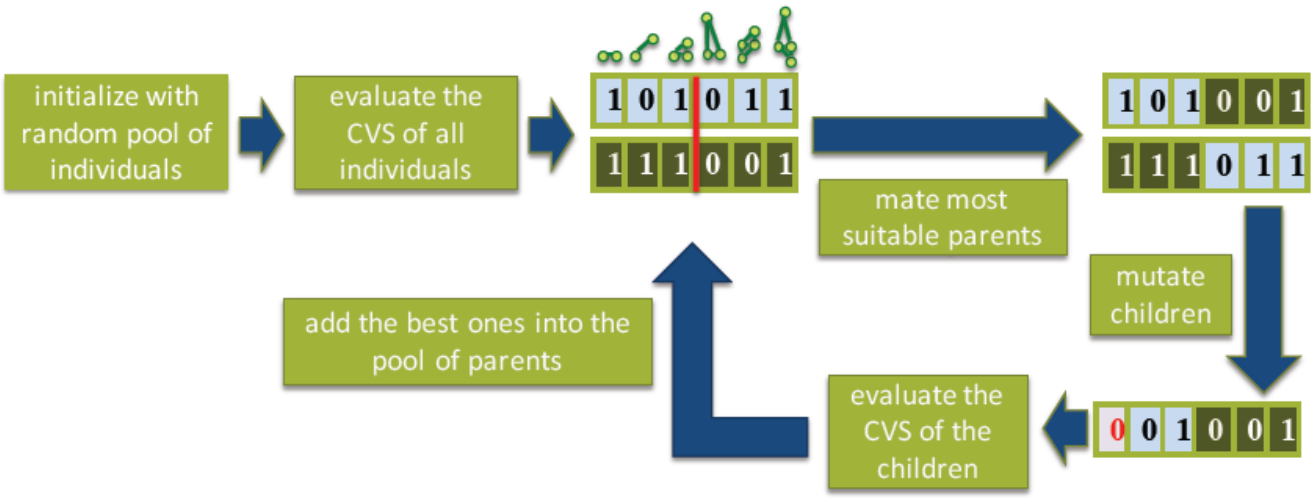

Figure 37 : Illustration of the genetic algorithm

In an example of crossover is given. Two ‘parent’ solutions marked red and green are used to create a ‘child’ solution. The sketch in shows mutation. A random bit in the binary string is flipped into the opposite state. Thus, the fitness of the new ‘population’ created by this process can be re-evaluated and the whole procedure is repeated until a solution with a small enough CVS is found.

This procedure will always find a minimum. But it remains unclear, if a local or global minimum has been found. Therefore, it is advisable to do a number of separate CE and take the solution with the lowest CVS as the final solution. UNCLE can be set up to do this automatically by doing a number of runs sequentially and only storing the best solution at the end.

5.1.5. Running the Cluster Expansion

After the genetic algorithm has converged a set of figures is chosen to describe the system best. This set predicted all the DFT derived ground state energies of the starting input set and resulted in the lowest SC_V. Structures, which were not members of the input set of the GA run, should now be predicted sufficiently correct. Now, the ECIs –

as derived from the fitting are taken to describe all possible structures of the system on the given parent lattice. If the enthalpy of formation of one of these structures is below the ground state line as defined by the DFT input data– this structure is included in an enlarged input set. As a consequence, its formation enthalpy is calculated by DFT and added it to the list of input structures. With this enlarged input set a new GA is done. This procedure is repeated until no new ground states are predicted by the CE. As a result, the stable structures of the system are obtained and the final ground state line.

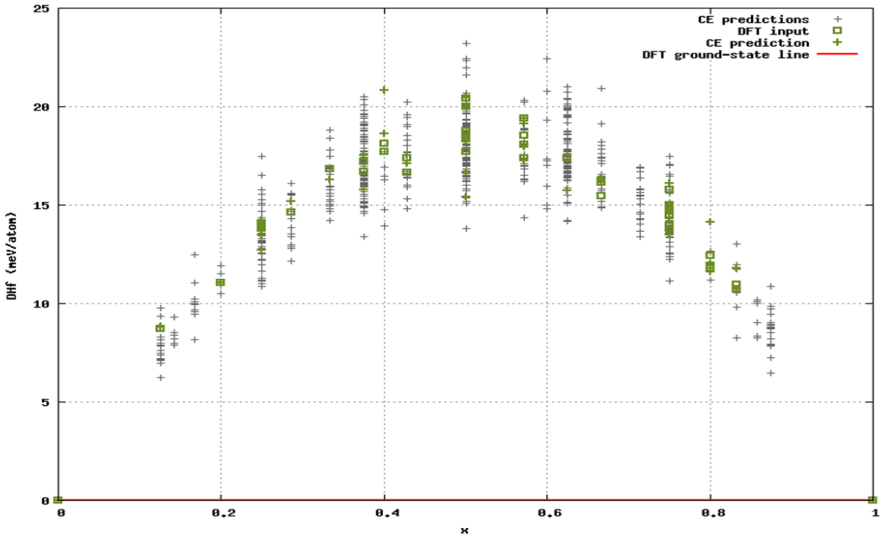

Figure 38 : Ground state line of the binary Li-S-Se systems for a bcc-parent lattice.

Red lines are the structure with lowest formation energies defining the ground state line; green squares denote the DFT results taken as input for the CE; green crosses represent the energies predicted by CE.

5.1.5.1. Miscible Constituents

If a model has miscible constituents, the structures with energies close to the ground states, that is those structures with the lowest ΔH_f at a given concentration, are the most

important ones, and the cluster expansion should be most accurate for those. To accomplish this, those structures predicted by the cluster expansion to be more favourable (with a lower ΔH_f) and are not yet part of the training set are added to the training set. This is done iteratively until no new structures are predicted by cluster expansion to be more favourable than those already included in the training set. At this point the cluster expansion has converged and from all structures considered by the cluster expansion the thermodynamically stable ones have been identified.

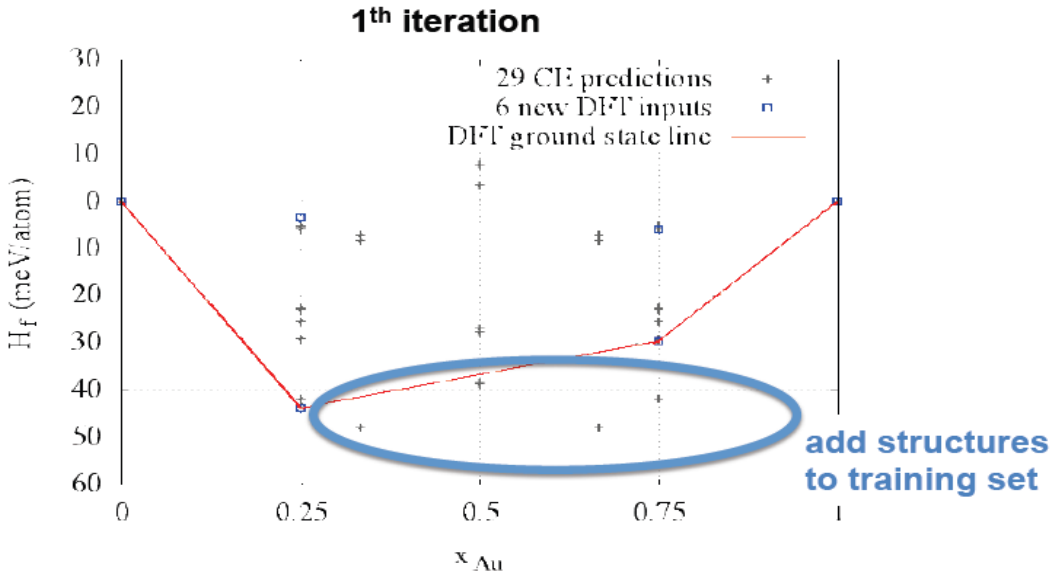

Figure 39 : Binary ground state diagram illustrating miscible constituent

5.1.5.2. Miscibility Gap

If the model is phase separating, no stable ordered structures exist apart from the two pure phases and all structures are of equal importance to the cluster expansion. Therefore, the selection process of structures to be added to the training set has to improve the quality of the cluster expansion for all structures considered, irrespective of their formation energies ΔH_f.

To determine how good (or bad) the energies of the structures are predicted by the cluster expansion the stochastic nature of the genetic algorithm is used. Multiple cluster expansions are performed using an identical training set. The energy of all considered structures are then predicted by these multiple *J*'s and a standard deviation of the predicted energies is evaluated. Structures with the highest standard deviation are those whose description by the cluster expansion is the worst. Therefore, these are added iteratively to the training set.

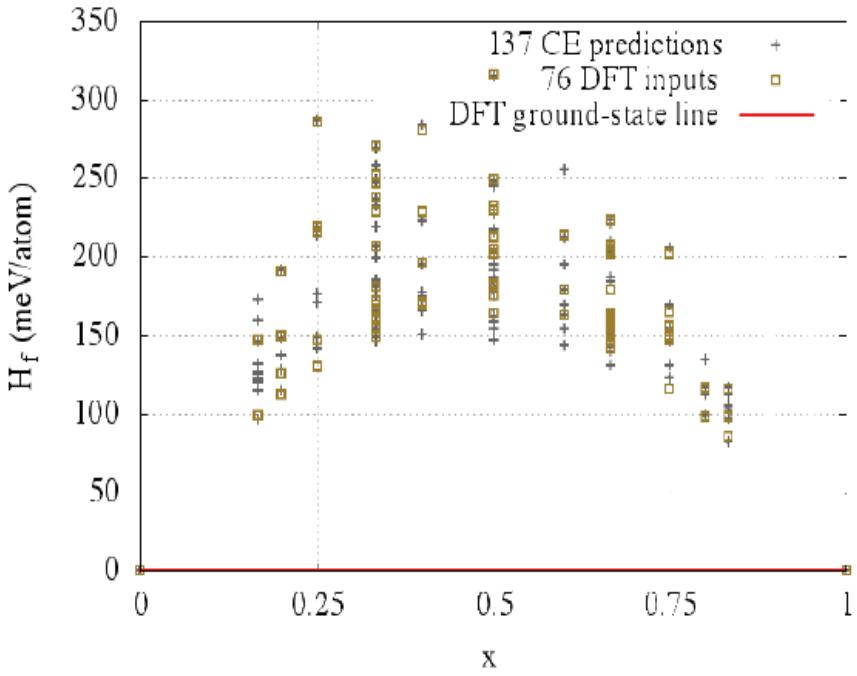

Figure 40: Binary ground state diagram illustrating miscibility gap

5.2. Monte Carlo Simulations

The cluster expansion needs effective interaction energies (ECI), which in the present case were derived from standard DFT calculations. Strictly, speaking DFT total energies are only valid for T=0K. To include temperature effects one might think first about configurational entropies, which in this work are included by performing Monte Carlo calculations based on the cluster expansion ingredients. Another and very

important temperature effect comes from vibrational entropies, which can be derived from DFT calculations for suitably selected displacements, like it is in Reith et.al. [133] . This is computationally very demanding in particular for ternary cases, and is far beyond the scope of a diploma thesis. Doing this then the ECI would become temperature dependent and with that also the whole CE. In the present work the Monte Carlo (MC) technique without lattice vibrations is applied. The Monte Carlo method (MC) is a stochastic method and it is often used for statistical thermodynamics. Its major application consists in the approximation of integrals, the calculation of mean values and the search for global minima in phase space. Since it is often very demanding or even impossible to cover the complete phase space just a

21 sample of it is taken into account. The choice of this sample is the most crucial point in the simulation. In the so-called simple or naive MC the sample is chosen randomly. This procedure is not very efficient for tasks such as finding a global minimum since the chosen phase points are distributed over the whole phase space. For such a distribution the probability to jump into the global minimum is quite small. An improvement would be a sample of suitably weighted points in phase space, which then leads into the global minimum. In this way, points in phase space with low weight would be neglected. Such an MC simulation is reasonable in describing a thermodynamical system at finite temperatures since the configurational entropy can be derived. For elucidating the application of MC in combination with the cluster expansion (CE) the basic principles will now be explained together with the MC implementation in the UNCLE-code.

5.2.1. Random Walks and Markov-chains

As already mentioned before the choice of the sample is the crucial point in finding thermodynamic characteristics of the investigated system. The crucial question is, how does the jump from one phase point to the next one happen? MC uses a random procedure for changing the point in the phase space: by applying the so-called *random walk* strategy every point has the same probability to be chosen as the next one to be considered. The corresponding transition probability P depends now only on the current point in phase space, but not on the n-2 points, which have been chosen before. This description of the transition probability is called a *Markov chain*.

$$P(K_n = i | K_{n-1} = j | ..... | K_0 = l) = P(K_n = i | K_{n-1} = j) = P_{ij}(n)\,.$$

Assuming that each transition probability P can be written as $P_{ij}(n)$ a matrix which contains the transition into each point of phase space can defined as

$$\mathbf{P} = \begin{pmatrix} P_{11} & \dots & P_{1K} \\ P_{21} & \dots & P_{2K} \\ \vdots & \ddots & \vdots \\ P_{K1} & \dots & P_{KK} \end{pmatrix}$$

This matrix has to fulfill two conditions, because it is stochastic, namely:

1. Because the matrix elements are probabilities, all the components have to be positive,

   $Pij \geq 0$.

2. The probability to *change* position in phase space has to be 1, which means $\sum_{j=1}^{K} Pij = 1$, with *i* being the current point and K being the number of points in phase space.

The next step in the random walk through phase space consists in defining the stationary probabilities of a point *i* to be populated after n steps:

$$w_i(n) = P(K_n = i)$$

Now the stationary probability vector w(n) is defined whose components are the probabilities of arriving at each point of the whole phase space,

$$w(n) = (w_1(n), w_2(n) \ldots w_K(n))^T$$

This vector has to fulfill again the conditions rules as the transition matrix $P \equiv P_{ij}$. Knowing the probability w of a given point in phase space for step n the probability for step n+1 is then defined as

$$w_j(n+1) = \sum_{i+1}^{K} w_i(n) P_{ij},$$

which –in a matrix notation– looks like

$$w(n+1) = Pw(n)$$

The vector **w** can now be constructed for s following steps by

$$w(n+s) = P^s w(n)$$

which for n=0 is

$$w(s) = P^s w(0)$$

At this point the probability distribution over the whole phase space after s steps can be predicted by knowing the probabilities of the points in phase space being populated and the transition probabilities at the start. Since in a random walk approach every step has the same probability, until now each element of the transition matrix and the stationary probability vector have the form of,

$$P_{ij} = \frac{1}{K}, \; w_i = \frac{1}{K}$$

In order to construct an efficient algorithm a weight for the transition to different points in the phase space has to be implemented.

5.2.2. Implementation of the MC Simulation in the UNCLE Code

In the UNCLE code a MC calculation with a grand-canonical and a canonical ensemble is possible. The system the calculation is dealing with is a box of atoms with a given extension and it obeys periodic boundary conditions: the box is a unit cell. For both the grand-canonical and the canonical calculation different implementations are made, as illustrated in figure 41.

5.2.3. Grandcanonial Ensemble

In a grandcanonical ensemble the system can be seen as the crystal of interest, which is connected to a reservoir of atoms that can propagate into the system. The total number

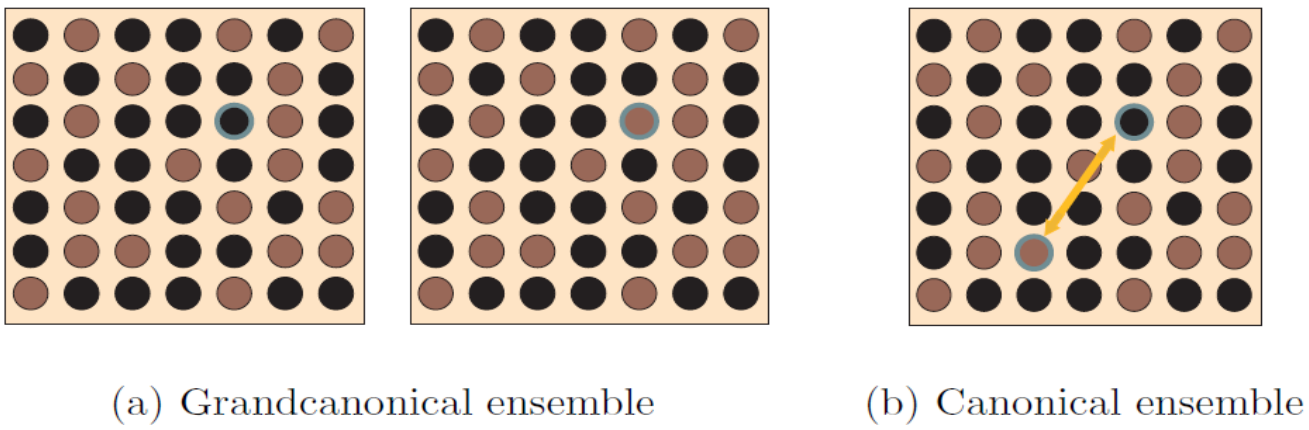

Figure 41 : Visualization of a MC step in UNCLE. In the grandcanonical simulation the type of one atom in the crystal is changed, in the canonical approach the positions of two atoms in the crystal are changed.

In both cases the Boltzmann distribution of the old and the new system are calculated and compared to decide if the transition is made or not. of atoms in the simulation box has to stay constant, which means that if an atom is added into it another one has to be removed. The thermodynamic which controls the propagation of the atoms in and out of the box is the chemical potential μ. If the chemical potential of one atom type in the system is raised, then the number of atoms of this type will be decreased. The reason for that is that if one atom (e.g. atom A) is removed from the system and another one (e.g. B) is added then the chemical potential changes by $\Delta\mu = \mu_A - \mu_B$ with μ_i being the chemical potentials for the atomic species. The transition rate for changing a configuration σ into σ' is then defined as

$$P^*_{\sigma\sigma'} = \begin{cases} 1 & \text{if} \epsilon < e^{-(\Delta E - \Delta\mu)/kT} \\ 0 & \text{if } \epsilon > e^{-(\Delta E - \Delta\mu)/kT} \end{cases}$$

where $\Delta E = E(\sigma') - E(\sigma)$. This means, that if the energy of the system after the atom exchange is lowered by a larger amount than the change of the chemical potential then the step will be accepted, otherwise it will be compared to the random number in the usual way as described above. Using the *Ising* model of the cluster expansion makes it easy to change an atom type at a defined position. The atom is chosen randomly and by changing the spin variable of it the atom type is obviously changed. In the next step the energy of the simulation box is calculated using the ECIs and the energy difference ΔE can now be calculated. Since the chemical potentials of the atom types are essential starting parameters $\Delta\mu$ and the Boltzmann factors are defined as well.

5.2.4. Canonical Ensemble

In a canonical ensemble the conserved quantity is the concentration of each atom type in the simulation box. In each step the position of two randomly chosen atoms is exchanged. Doing so the energy of the composition in box changes and the transition rate can be written as

$$P^*_{\sigma\sigma'} = \begin{cases} 1 & \text{if } \epsilon < e^{-(E(\sigma')-E(\sigma))/kT} \\ 0 & \text{if } \epsilon > e^{-(E(\sigma')-E(\sigma))/kT} \end{cases}$$

The random walk through phase space is continued until a chosen number of steps is done or the change in the energy of the system is below a given numerical limit. In the present work the grandcanonical simulations as done for the binary systems were limited to a certain number of steps done.

5.3. Results and Discussions

5.3.1. Search for the Ground States (Cluster Expansion)

The ground-state search of binary compounds by total-energy calculations and diagrammatic approaches suffers largely from the need that the small group of crystallographic configurations considered must include the stablest one. The combination ‘CE plus MC’ allows us to circumvent this problem as it will be demonstrated in this thesis.

To start the CE for searching for the ground states of the Li_2-SSe system the DFT energy formation enthalpies of Li_2-SSe were computed. In addition, 42 other structures as

suggested by the genetic algorithm (GA) were added. By starting a GA with these structures a cross validation score (CVS) of 2 meV per atom was achieved and a new input structure which was predicted as a ground state by the CE was chosen in this first run to be calculated with VASP and to be added to the input set. The maximal size of the unit cells for the CE predictions were adjusted during the fitting procedure and finally the largest unit cells contained 24 atoms. When no new ground state structures were found by CE, the system was considered to have converged. The final ground state line relative to the fcc ground states of the elements and the predicted enthalpies of formation are shown in figure below.

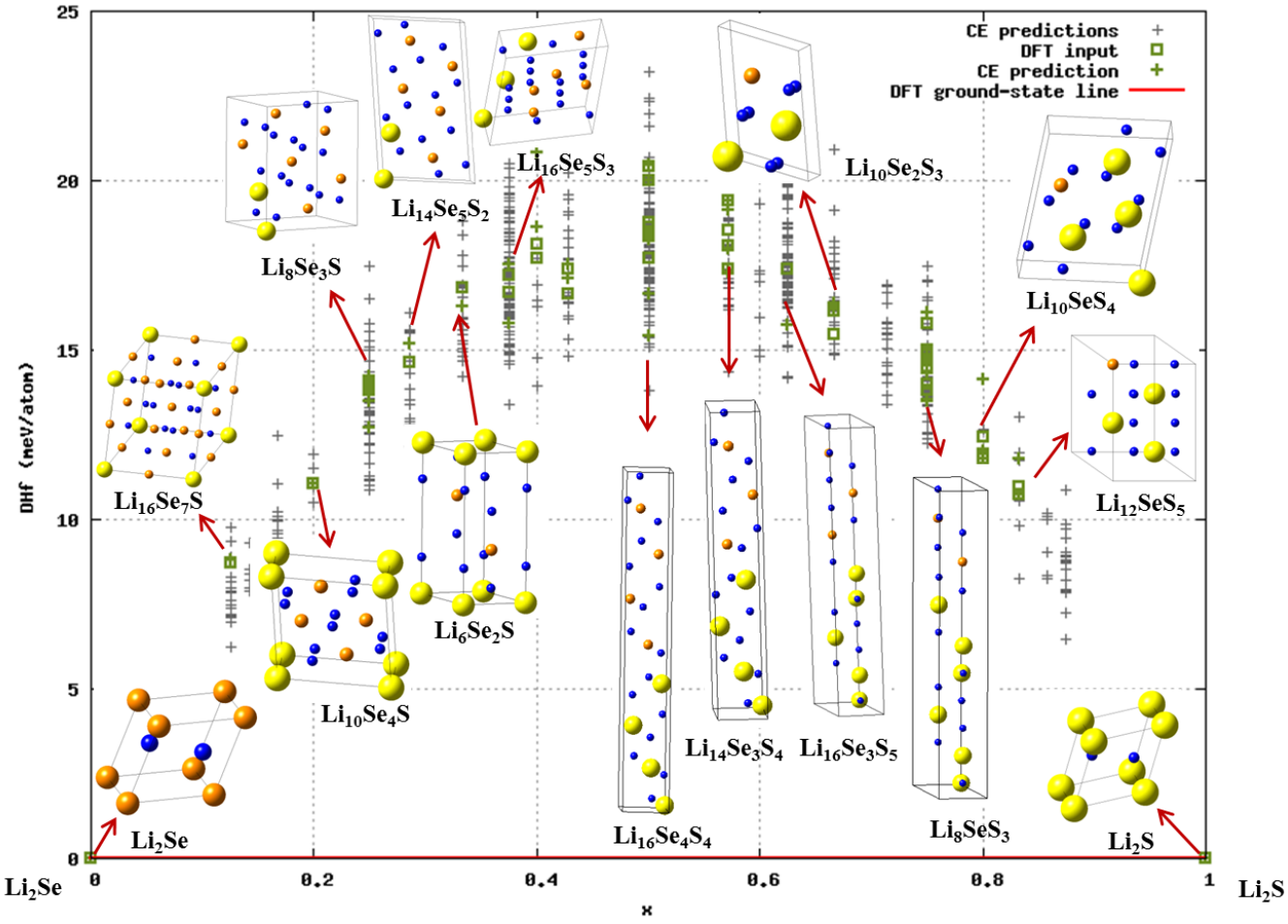

Figure 42 : Final ground state line of the Li-S-Se system: enthalpy of formation versus Se concentration and ground state structures.

Green Square represent the structures, which are the most favourable within a bcc-type lattice phases which were predicted as ground state structures in the previous CE runs and which were recalculated by DFT. The ECIs were fitted to these phases and then used for the CE to predict all the possible bcc-type structures with maximal 24 atoms per unit cell. From the averaged distance of the predicted structures from the final ground state line the preference of the system to crystalize in a bcc lattice can be estimated. In the extremal parts of the concentration range the predicted structures show formation enthalpies, which are more distant from the ground state line.

In the following, we will perform and discuss the temperature-dependent form of the CE where the additionally included vibrational free energy is, in general, important for the phase stability of alloys and compounds [134]. For this purpose, the phase separating binary Li-S-Se alloy system at the Li-S-rich side of the phase diagram is considered. For such a system, the application of CE needs particular care because no ground state line of ordered compounds exists, i.e., all formation energies are positive. All the CE and DFT calculations were made for Li-S-Se alloys with a bcc parental lattice, since the main interest is in the Li-S-rich part of the phase diagram. For pure Se, also the FCC ground state total energy was calculated as a reference. For the CE, our universal cluster expansion (UNCLE) program package was applied. Initially, a standard CE for a bcc parental lattice was made utilizing only the DFT total energies for $T = 0$ K. The results in Fig. 40 reveal that no thermodynamically stable binary phase for any composition exists, as it is expressed by the positive formation energies. As expected, the configurations with the lowest formation enthalpies (and the form of the ground-state line) correspond to phase separating atomic arrangements, which consist

of slabs of pure Li-S and Li-Se. In total, an input DFT set of 42 configurations up to eight-atoms large was taken into account resulting in a CVS of 2.0 meV/atom at T = 0 K. The input set includes the energetically favourable structures as well as configurationally excited states in order to get reliable MC results.

Table 28 : Li-S-Se system: the ground state enthalpies of formation as derived by DFT and CE.

Comparison of energies E and formation energies DHf in eV as predicted by the cluster expansion (CE)
and as calculated by the computational engine (DFT).
Energy differences to the structure at the ground state line (GSL) for each composition x are listed.

# no.	x(1:k,1:nC)		E_DFT	D(E_DFT,E_CE)	E_CE	DHf_DFT	DHf_CE	Dist to GSL DFT	title	cell formula	space group
1	0.00000	1.00000	-11.1321260000	0.0000001000	-11.1321259000	0.0000000000	0.0000000000	0.0000000000	ce2	Li2Se	Fm-3m
2	0.12500	0.87500	-11.2312507500	0.0001027632	-11.2311479868	0.0087203750	0.0088230407	0.0087203750	ce631	Li16Se7S	Fm-3m
3	0.20000	0.80000	-11.2936312000	0.0000212132	-11.2936099868	0.0110470000	0.0110681172	0.0110470000	ce57	Li10Se4S	I4/m
4	0.25000	0.75000	-11.3337940000	-0.0013281952	-11.3351221952	0.0140222500	0.0126939598	0.0140222500	ce386	Li16Se6S2	R-3m
5	0.25000	0.75000	-11.3338545000	0.0002775527	-11.3335769473	0.0139617500	0.0142392077	0.0139617500	ce609	Li16Se6S2	C2/m
6	0.25000	0.75000	-11.3339070000	-0.0004185410	-11.3343255410	0.0139092500	0.0134906140	0.0139092500	ce420	Li16Se6S2	C2/m
7	0.25000	0.75000	-11.3340235000	-0.0001199280	-11.3341434280	0.0137927500	0.0136727270	0.0137927500	ce416	Li16Se6S2	C2/m
8	0.28571	0.71429	-11.3639931429	0.0005335998	-11.3634595430	0.0146360000	0.0151695056	0.0146360000	ce207	Li14Se5S2	C2/m
9	0.33333	0.66667	-11.4028783333	-0.0005498349	-11.4034281682	0.0168346667	0.0162847384	0.0168346667	ce8	Li6Se2S	P-3m1
10	0.37500	0.62500	-11.4384793750	0.0003499977	-11.4381293773	0.0171820000	0.0175319052	0.0171820000	ce334	Li16Se5S3	C2/m
11	0.37500	0.62500	-11.4389678750	-0.0009252329	-11.4398931079	0.0166935000	0.0157681746	0.0166935000	ce337	Li16Se5S3	P-1
12	0.40000	0.60000	-11.4590934000	0.0004769301	-11.4586164699	0.0181370000	0.0186138381	0.0181370000	ce45	Li10Se3S2	I4/mmm
13	0.40000	0.60000	-11.4595274000	0.0031136561	-11.4564137439	0.0177030000	0.0208165641	0.0177030000	ce42	Li10Se3S2	R-3m
14	0.42857	0.57143	-11.4845024286	0.0001267093	-11.4843757192	0.0173782857	0.0175049036	0.0173782857	ce213	Li14Se4S3	C2/m
15	0.42857	0.57143	-11.4852287143	0.0004718661	-11.4847568482	0.0166520000	0.0171237746	0.0166520000	ce199	Li14Se4S3	Immm
16	0.50000	0.50000	-11.5430783750	0.0000169831	-11.5430613919	0.0204281250	0.0204450181	0.0204281250	ce628	Li16Se4S4	Imma
17	0.50000	0.50000	-11.5434951250	-0.0000197180	-11.5435148430	0.0200113750	0.0199915670	0.0200113750	ce626	Li16Se4S4	Fd-3m
18	0.50000	0.50000	-11.5447526667	-0.0003957904	-11.5451484571	0.0187538333	0.0183579529	0.0187538333	ce97	Li12Se3S3	Cmmm
19	0.50000	0.50000	-11.5448603333	-0.0002316233	-11.5450919566	0.0186461667	0.0184144534	0.0186461667	ce93	Li12Se3S3	P4/mmm
20	0.50000	0.50000	-11.5451260000	-0.0001446246	-11.5452706246	0.0183805000	0.0182357854	0.0183805000	ce482	Li16Se4S4	Cmmm
21	0.50000	0.50000	-11.5451390000	-0.0029527917	-11.5480917917	0.0183675000	0.0154146183	0.0183675000	ce290	Li16Se4S4	R-3m
22	0.50000	0.50000	-11.5458121667	-0.0010238807	-11.5468360474	0.0176943333	0.0166703626	0.0176943333	ce89	Li12Se3S3	Pmmm
23	0.57143	0.42857	-11.6057380000	-0.0000004797	-11.6057384797	0.0193942857	0.0193937174	0.0193942857	ce184	Li14Se3S4	I4/mmm
24	0.57143	0.42857	-11.6066200000	0.0006381805	-11.6059818195	0.0185122857	0.0191503776	0.0185122857	ce191	Li14Se3S4	C2/m
25	0.57143	0.42857	-11.6070735714	-0.0000803273	-11.6071538988	0.0180587143	0.0179782984	0.0180587143	ce156	Li14Se3S4	R-3m
26	0.57143	0.42857	-11.6077324286	-0.0001129330	-11.6078453616	0.0173998571	0.0172868356	0.0173998571	ce237	Li14Se3S4	R3
27	0.62500	0.37500	-11.6539891250	-0.0016314014	-11.6556205264	0.0173625000	0.0157310111	0.0173625000	ce266	Li16Se3S5	R-3m
28	0.66667	0.33333	-11.6911600000	0.0000733382	-11.6910866618	0.0161400000	0.0162132515	0.0161400000	ce6	Li6SeS2	Immm
29	0.66667	0.33333	-11.6918186667	0.0008813215	-11.6909373452	0.0154813333	0.0163625681	0.0154813333	ce69	Li12Se2S4	Pmmn
30	0.75000	0.25000	-11.7634167500	0.0003306131	-11.7630861369	0.0157800000	0.0161105281	0.0000000000	ce448	Li16Se2S6	I4/mmm
31	0.75000	0.25000	-11.7642180000	0.0000267651	-11.7641912349	0.0149787500	0.0150054301	0.0149787500	ce14	Li8SeS3	P4/mmm
32	0.75000	0.25000	-11.7642297500	-0.0002068809	-11.7644366309	0.0149670000	0.0147600341	0.0149670000	ce15	Li8SeS3	I4/mmm
33	0.75000	0.25000	-11.7645135000	-0.0000192751	-11.7645327751	0.0146832500	0.0146638899	0.0146832500	ce444	Li16Se2S6	Cmmm
34	0.75000	0.25000	-11.7647222500	-0.0009302994	-11.7656525494	0.0144745000	0.0135441156	0.0144745000	ce258	Li16Se2S6	R-3m
35	0.75000	0.25000	-11.7651895000	0.0003274358	-11.7648620642	0.0140072500	0.0143346008	0.0140072500	ce250	Li16Se2S6	R-3m
36	0.75000	0.25000	-11.7653815000	-0.0003429516	-11.7657244516	0.0138152500	0.0134722134	0.0138152500	ce275	Li16Se2S6	Pmmn
37	0.80000	0.20000	-11.8098998000	0.0016889807	-11.8082108193	0.0124350000	0.0141238967	0.0124350000	ce30	Li10SeS4	R-3m
38	0.80000	0.20000	-11.8104160000	0.0001105051	-11.8103054949	0.0119188000	0.0120292211	0.0119188000	ce32	Li10SeS4	C2/m
39	0.80000	0.20000	-11.8105262000	-0.0001809628	-11.8107071628	0.0118086000	0.0116275532	0.0118086000	ce31	Li10SeS4	Immm
40	0.83333	0.16667	-11.8401120000	-0.0002506986	-11.8403626986	0.0109815000	0.0107307180	0.0109815000	ce64	Li12SeS5	C2/m
41	0.83333	0.16667	-11.8403600000	0.0010364972	-11.8393235028	0.0107335000	0.0117699139	0.0107335000	ce58	Li12SeS5	P-3m1
42	1.00000	0.00000	-11.9948870000	0.0000000800	-11.9948869200	0.0000000000	0.0000000000	0.0000000000	ce1	Li2S	Fm-3m

5.3.1.1. Miscibility Gap

This indicates that the cluster expansion optimization scheme automatically switched from the miscible constituents to the miscibility gap mode in the second iteration, because Li_2-SSe is a system with a miscibility gap. As a convergence criterion in this

mode the standard deviation of 96.51% of the predicted structures has to be below 2 meV. This value was set for the variable (Convergence criterion for cluster expansion optimization in the cluster expansion (optimization) panel. Due to Li_2-SSe having a miscibility gap no stable structures with respect to the pure phases exist. The Table listing stable structures therefore only contains the two pure phases Li-S and Li-Se.

Table 29 : Listing stable structures therefore only contains the two pure phases Li-S and Li-Se.

Iteration	no. of struc.	no. of new struc.	CVS [meV]	% struc. with SD below 2 [meV]
0	0	2	-	-
0	0	10	-	-
1	10	8	0.015	-
2	18	8	0.34	8.72
3	26	8	0.3	19.02
4	34	8	0.66	51.66
5	42	0	0.91	96.51

The structures constituting the DFT ground state line, their compositions x and formation energies DHf

# x(1:k,1:nC)	DHf / atom [eV]	structure title	cell formula	space group
0.0000000000	1.0000000000	0.0000000000	ce2	Li2Se	Fm-3m
1.0000000000	0.0000000000	0.0000000000	ce1	Li2S	Fm-3m

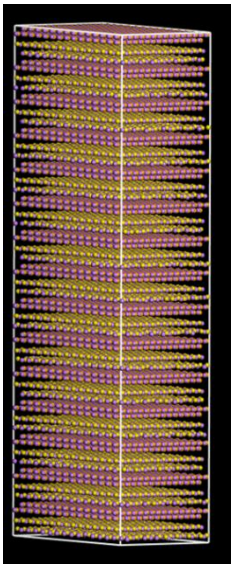

Figure 43 : Demonstration of phase separating Li_2S-Se system.

5.3.2. Monte Carlo Simulations

A canonical ensemble was chosen for the Monte Carlo (MC) simulation of the Li_2S-Se system. Periodic boxes containing 25x25x25 atoms were used. The initial setup of pure Se and Li-S blocks as shown on figure 43 is brought into thermodynamically equilibrium for a fixed temperature. The volume in the Li-S block in which the dissolved Se atoms are counted, which are three layers away from the interface. This ensures that no Se atom of the Se slab is erroneously counted as dissolved. CE and MC calculations were made for the merged figure set using averaged ECIs

$$E_{\mathrm{CE}}(\sigma) \rightarrow E_{\mathrm{CE}}(\sigma,T) = N \sum_{\mathrm{f}\in\mathbb{F}(T)} D_{\mathrm{f}} J_{\mathrm{f}}(T) \Pi_{\mathrm{f}}(\sigma).$$

According to Eq. above, different temperatures yield different F(T). However, one finds that the temperature dependence of the solubility is not as smooth a function of the temperature as expected, when only one single CE is considered for each temperature. This is a direct effect of the stochastic GA, selecting the figure set F(T), and it can indeed be likened to that kind of arbitrariness that enters even at a *single* temperature: n different runs of the GA yield n different Fi (T). All of them are equally capable to map the input data onto the CE [see Eq. above] but yield slightly different results in MC simulations. For the usual CE applications, this does not pose a problem: the precision needed for MC simulations with respect to concentration is not as strict as needed here for the Se solubility in Li-S (<1 at.%), because the overall solubility is so low that even minor deviations result in a large relative error in predictions.

5.3.2.1. Coherent Precipitates

Solid state decomposition reactions like the phase separation of an alloy into its constituents, A1−xBx _ $(1 - x)$A + xB, create so-called precipitates which define an

important part of the microstructure of many alloy systems. The early stage of these reactions typically involves the formation of *coherent precipitates* that adopt the crystallographic lattice of the alloy from which they emerge [135]. Coherent precipitates have practical relevance, as they impede dislocation motion and thus lead to 'precipitation hardening' in many alloys [136] [137]. Despite their importance, precipitate microstructures were thus far not amenable to first-principles theories, since their description requires 'unit cells' containing 103–106 atoms or more, well beyond the current capabilities of first-principles methods. The chemical and structural properties of precipitates are determined by the identity of the phases being located to the left and right of the two-phase region in the phase diagram. In the case of the phase-separating system Li_2S-Se, one of the prototype systems for studying coherent precipitates, the two-phase region corresponds to Li_2S and Se, so that coherent precipitates formed from the Li_2S fcc-based solid solution consist of only Se atoms.

To calculate equilibrium shapes of coherent precipitates we use the CE, in canonical ensemble MC simulations. In order to exclude boundary effects, unit cells containing up to 25×25×25 = 16625 atoms were needed. We used fix boundary conditions so that boundary sites are always occupied by Se atoms. These atoms are 'frozen', i.e. cannot flip their identity. This restriction has the advantage that precipitates cannot grow over the cell boundaries. The MC annealing process is initialized at a sufficiently high temperature, where the solid solution is thermodynamically stable. Using a given number NSe of Se atoms in the MC cell (hence, a given average precipitate size .R), the system is carefully annealed below the coherent fcc miscibility gap. Upon crossing this solvus, a coherent precipitate is formed.

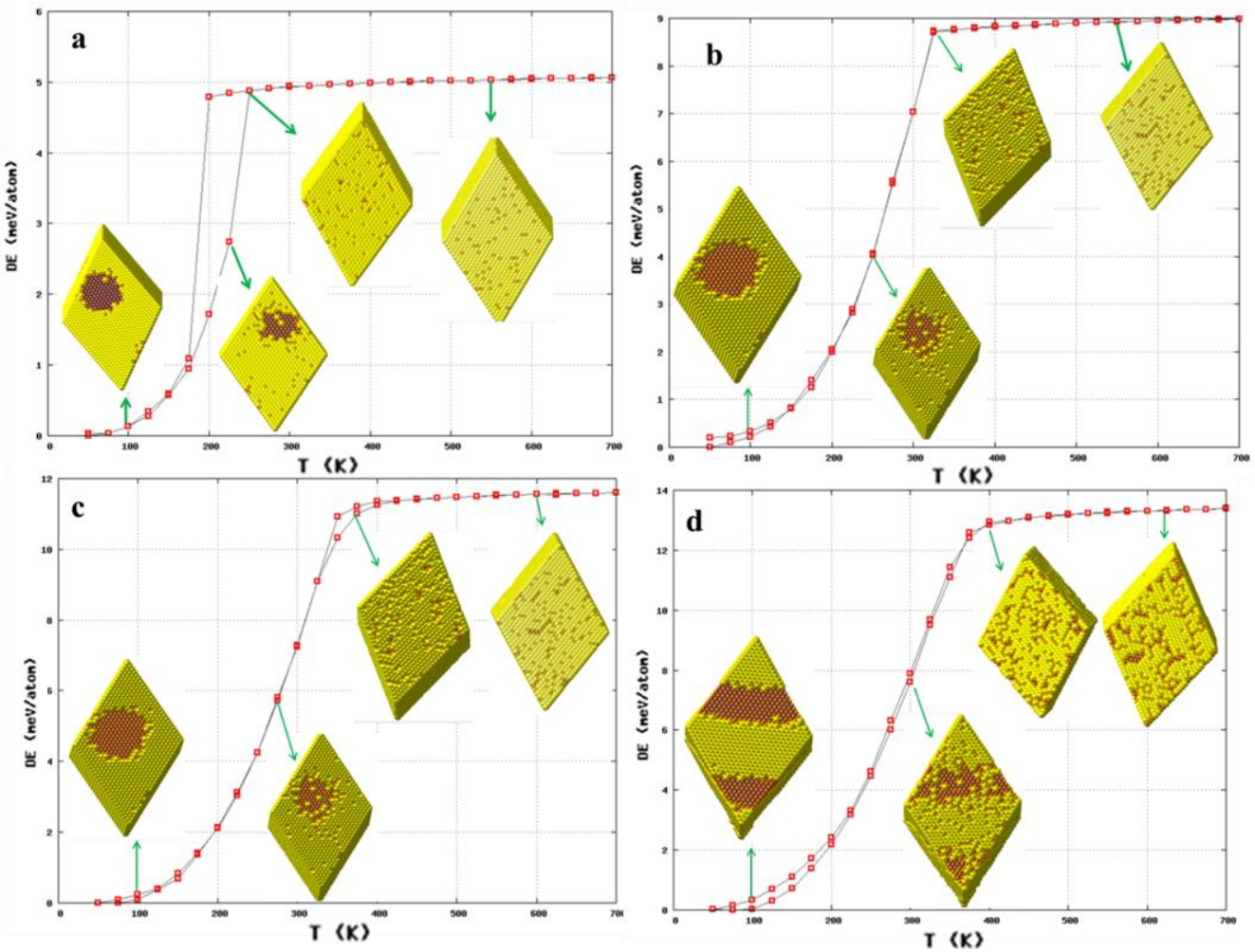

Figure 44: : Temperatures profiles cross sections through the 25 × 25 × 25 Monte Carlo simulation cells of Li-S-Se at different concentrations (a)Li- S0.9 Se0.1 , (b)Li- S0.8 Se0.2 , (c)Li- S0.7 Se0.3 , (d)Li- S0.6 Se0.4.

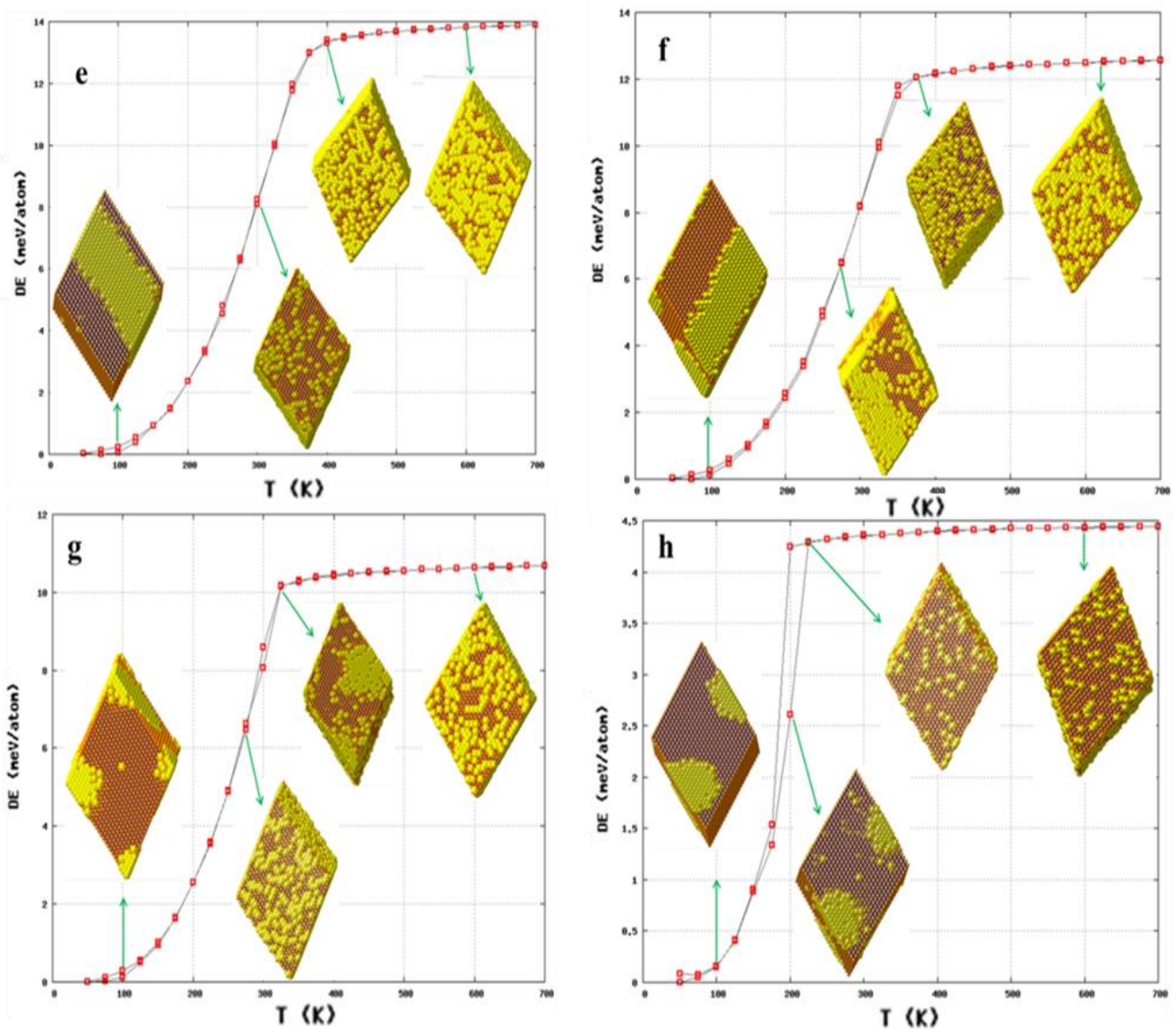

Figure 45: : Temperatures profiles cross sections through the 25 × 25 × 25 Monte Carlo simulation cells of Li-S-Se at different concentrations (e)Li- S0.5 Se0.5 , (f)Li- S0.4 Se0.6 , (g)Li- S0.3 Se0.7, (h)Li- S0.2 Se0.8.

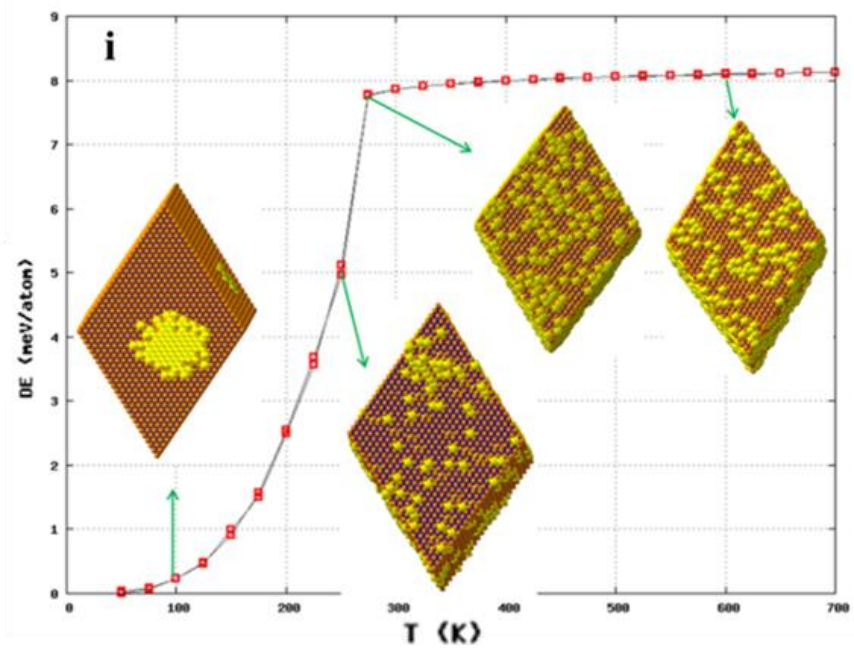

Figure 46 : Temperatures profiles cross sections through the 25 × 25 × 25 Monte Carlo simulation cells of Li-S-Se at different concentration (i)Li- $S_{0.1}$ $Se_{0.9}$

5.3.3. Constructed Phase Diagram

Below we show a table of concentrations of sulphur and selenium with critical temperatures generated from MC interactive temperature vs. energy graphs (figure 44, 45 and 46). Critical temperatures are then used to construct phase diagram in figure 45 which was found to be in great agreement and consisting same shape as Li_2S phase [138] and Li_2Se [139] phase diagram which could suggest that we are great agreement with our calculations.

The transition temperature from mixture to the phase separated regions are comparative low indicating that random mixture might be metastable at temperatures below 380K as this is a diffusion driven process. At these temperatures diffusion might be too slow (this might require a further study on diffusivity)

Table 30: Concentration of Sulphur and Selenium with respective critical temperatures

Concentrations (S,Se)	Critical Temperatures (K)
0.1	225
0.2	325
0.3	350
0.4	375
0.5	380
0.6	350
0.7	325
0.8	275
0.9	225

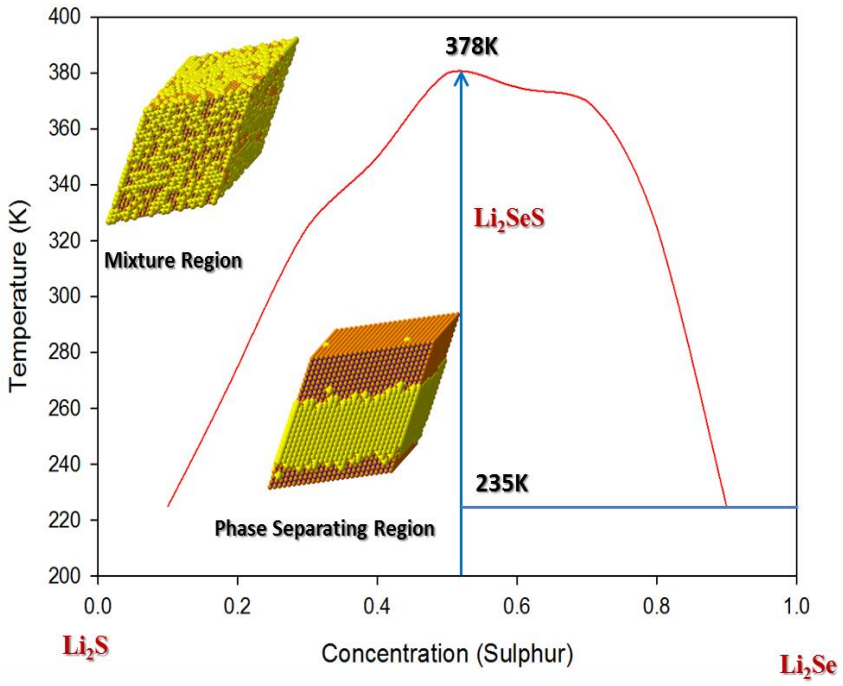

Figure 47 : Constructed phase diagram of Li-S-Se using phase transition temperature at different concentrations

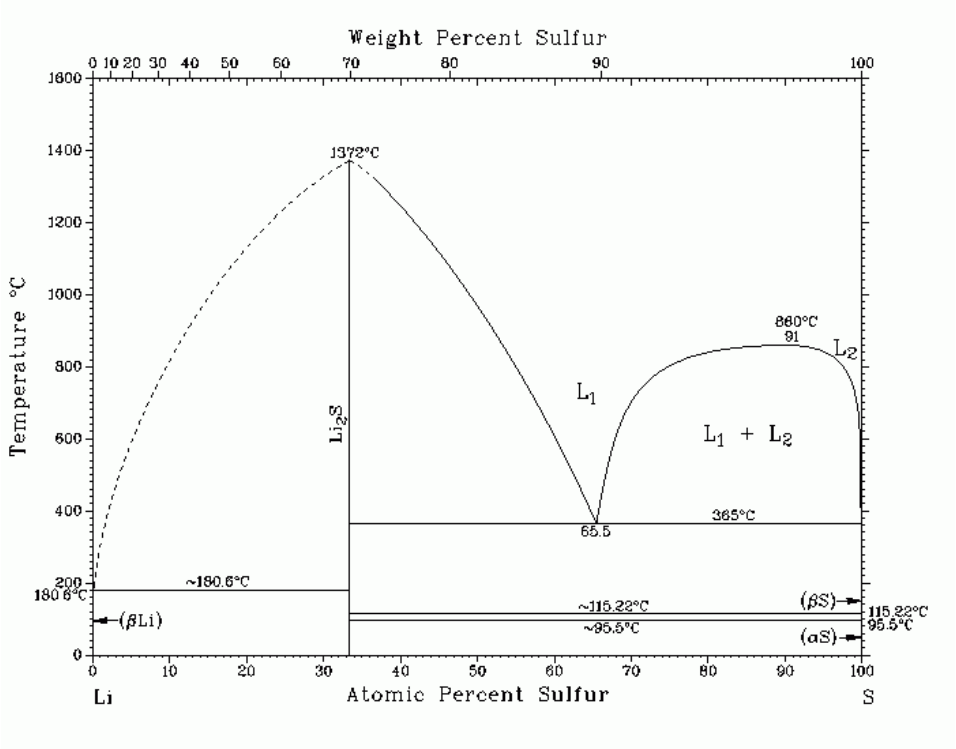

Figure 48 : Experimental phase diagram for Li-S system [139].

5.3.4. Discussions

The practical limitations on the lithium- sulphur battery, which has potential to offer high energy density, have generated significant interest in searching for possible remedies. We propose an introduction of selenium, a d–electron containing member of group 16 with high electrical conductivity, in the electrode as a viable option of addressing such challenges. Mixed S-Se is an attractive new class of cathode materials with promising electrochemical performance in reactions with lithium ions. In the current chapter, an accurate and efficient cluster expansion energy model for Li-S-Se system was developed. Monte Carlo simulations using the cluster expansion method

were performed to investigate the structure of Li-S-Se at both atomistic and nano scales. Cluster expansion method was employed to generate 42 new stable phases from a binary phase diagram. The new phases generated formed a miscibility gap due to their phase separating behaviour. Monte Carlo simulations technique was utilized to investigate thermodynamic properties of Li_2S-Se system for the entire range of Se concentrations. It was found that the system remains phase separating at 0K and a mixture occurs around 350K. We constructed a phase diagram from Monte Carlo simulations results to show how Li_2S-Se changes phases when temperature is introduced and it is in good agreement with reported experimental work on both Li_2S and Li_2Se [140]. Phase equilibrium of Li-S-Se system requires that the free energy of all the constituent phases are known as a function of composition and temperature. The techniques have been successfully employed by Nguyen *et al*. [141] on binary (NiFe)(AlFe) and Chinnappan *et al* [142] on the V–Ta alloy, where the solid solution phase has a bcc structure. Our results prove the usefulness and the suitability of a combined cluster expansion and Monte Carlo approach for studying phase transformations and thermodynamic properties occurring in Li_2S-Se system.

Chapter 6: Comparison between Monte Carlo Simulations and Molecular Dynamics for $Li_2S_{0.5}Se_{0.5}$.

In this chapter we compare two techniques used in chapter 5 and chapter 6, we specifically test validated Born Meyer potential models for a mixed Li_2S-Se at 50% each. We use the phase at 50% generated by Cluster Expansion and Monte Carlo simulations techniques to employ Molecular Dynamics to check if we could manage to produce near same results.

6.1. Cluster Expansion Ground State Search

It was noted from Chapter 6, that Li_2S-Se is a phase separating system and has miscibility gap. Hence it was crucial to perform MC for thermodynamically stability of the system. Figure below shows Li_2S-Se phase separating.

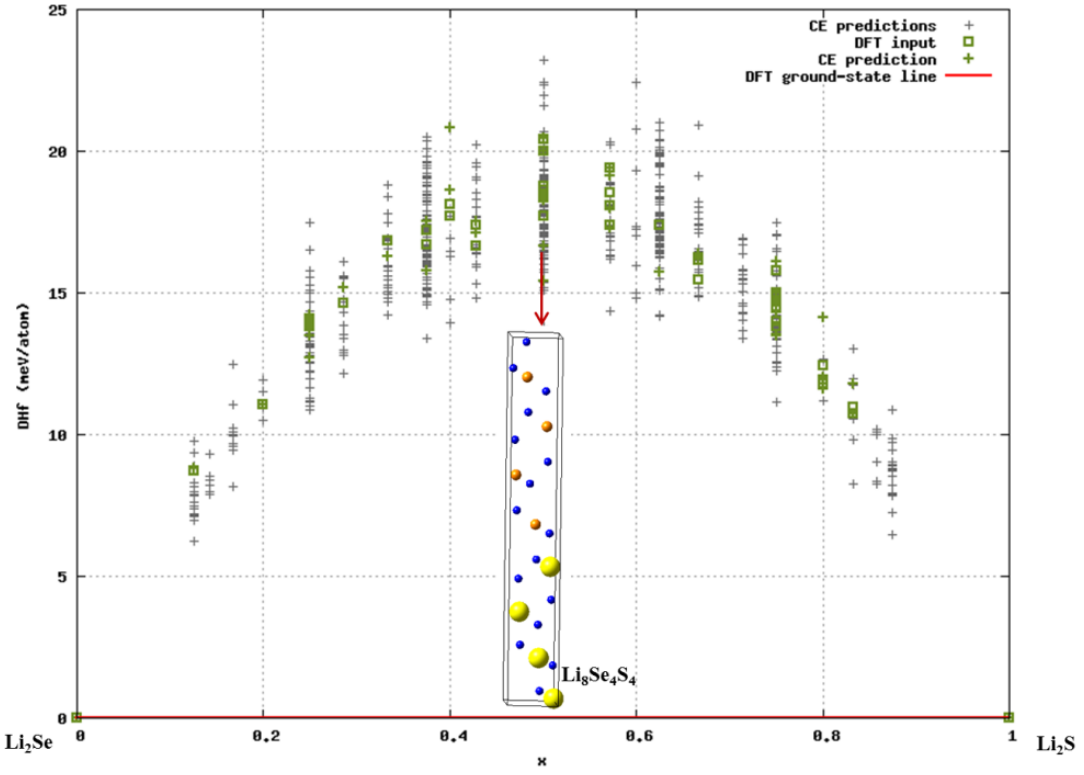

Figure 49: Binary phase diagram for $Li_2S_{50\%}$-$Se_{50\%}$

6.2. Monte Carlo Simulation: Temperature Profile at $Li_2S_{0.5}$-$Se_{0.5}$

Monte Carlo temperature profile at 50% of Sulphur and Selenium shows that there is phase transition at 380 K as seen in chapter 6. The changes from phase separating to a mixture at 380K temperature.

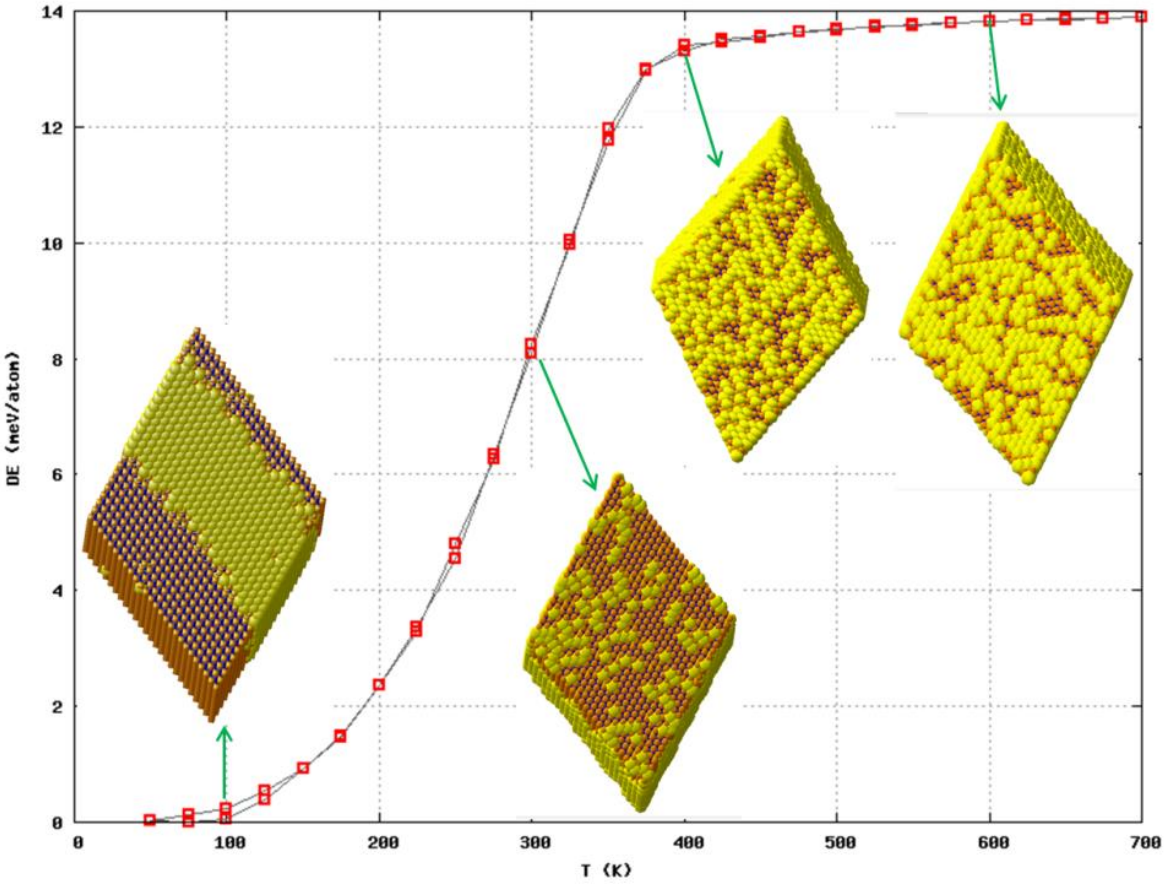

Figure 50: Monte Carlo temperature profiles for Li_2S50%-Se50%

6.3. Validation of the Atomistic Potentials Model

In this section we consider the validation of our derived interatomic potential models for Li_2S-Se. We combined the set if potentials derived and validated in chapter 5 for both Li_2S and Li_2Se systems.

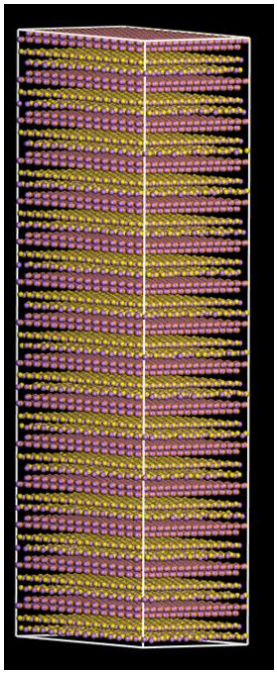

Figure 51: Cubic unit cell of bulk Li_2S-Se.

The potential models are developed to simplify the complexity of the quantum mechanical computations. For example, even a semi-qualitative force field or potential model can be used to identify the most probable surfaces, and hence reduce the number of surfaces that need to be examined using quantum mechanical methods. The elastic constants, calculated by quantum mechanics, were used as input data for the development of potentials models. The accuracy of the derived interatomic potentials was first checked by comparing the known experimental and calculated data. To validate our potential models we start by showing the properties that where obtained from our derived potentials i.e., lattice parameters, interatomic distances, and elastic properties.

Table 31 shows the calculated lattice parameters obtained from different methods. The lattice parameters obtained using energy minimisation codes GULP and METADISE are smaller than those from the literature, but still within the acceptable range of 2%.

Table 31: Comparison of the lattice parameter of Li_2S-Se, obtained from the derived interatomic potentials, with the other calculated values.

Method	Parameter *a (Å),b(Å),c(Å)*
Potential Model (This Work)	19.40, 7.77, 3.89
VASP (GGA-PBE) (This Work)	19.00, 7.30, 3.49

Table 32 shows a comparison of the elastic properties of Li_2S-Se we calculated using DFT methods (VASP code) and those calculated from our derived interatomic potentials employing the GULP and METADISE codes; experimental elastic constants are available for Li_2S. The elastic constants from the interatomic potentials are in good agreement with those from DFT calculations, together with the various moduli of elasticity, i.e. the bulk, shear and elasticity moduli.

Table 32: Calculated elastic constants and moduli of the Li_2S-Se phase.

Elastic Properties	Observable (VASP)	GULP (Fitted)
C_{11}	74.12	70.25
C_{12}	18.12	23.15
C_{44}	36.60	40.76
C_{13}	17.64	17.71
C_{33}	83.40	82.44
Bulk Modulus, *B* (GPa)	36.79	38.00
Shear Modulus, *G* (GPa)	33.16	34.09
Elasticity Modulus, *E* (GPa)	78.12	79.35

6.4. Phonon Dispersion of $Li_2S_{0.5}$-$Se_{0.5}$

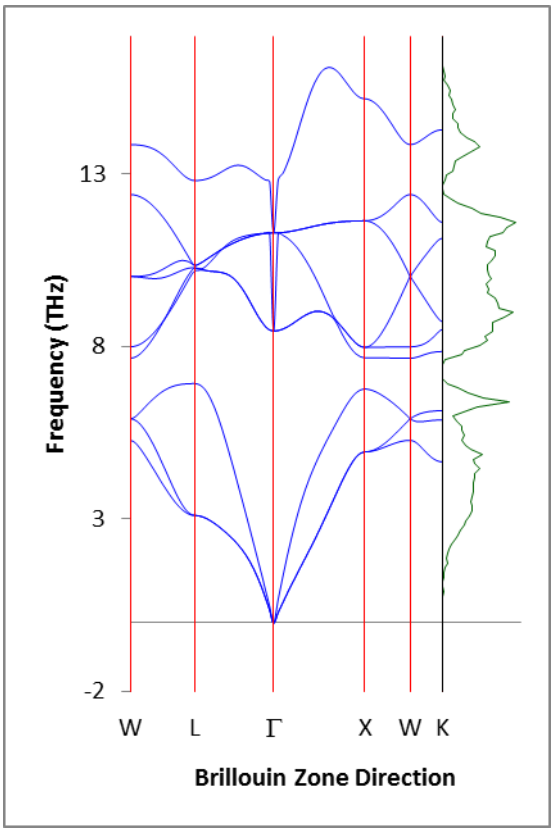

Figure 52: Phonon DOS and dispersion curve of $Li_2S_{50\%}$-$Se_{50\%}$ phase.

Figures 52 above shows the phonon dispersion curve and the total density of states (DOS) of the $Li_2S_{0.5}$-$Se_{0.5}$ phase which allude to the stability of the system. This is deduced from all phonon branches lying above 0 THz, implying that there are no soft modes encountered along high symmetry directions. This is an indication that the $Li_2S_{0.5}$-$Se_{0.5}$ phase is stable.

6.5. Molecular Dynamics of $Li_2S_{0.5}$-$Se_{0.5}$

Molecular Dynamics calculations were performed utilizing potential models derived in chapter 4 for both Li_2S and Li_2Se. The figure 53 shows RDF and structures which shows

that the $Li_2S_{0.5}$-$Se_{0.5}$ melts at 500K which is great agreement with the study on chapter 6 where Monte Carlo Simulations were utilized.

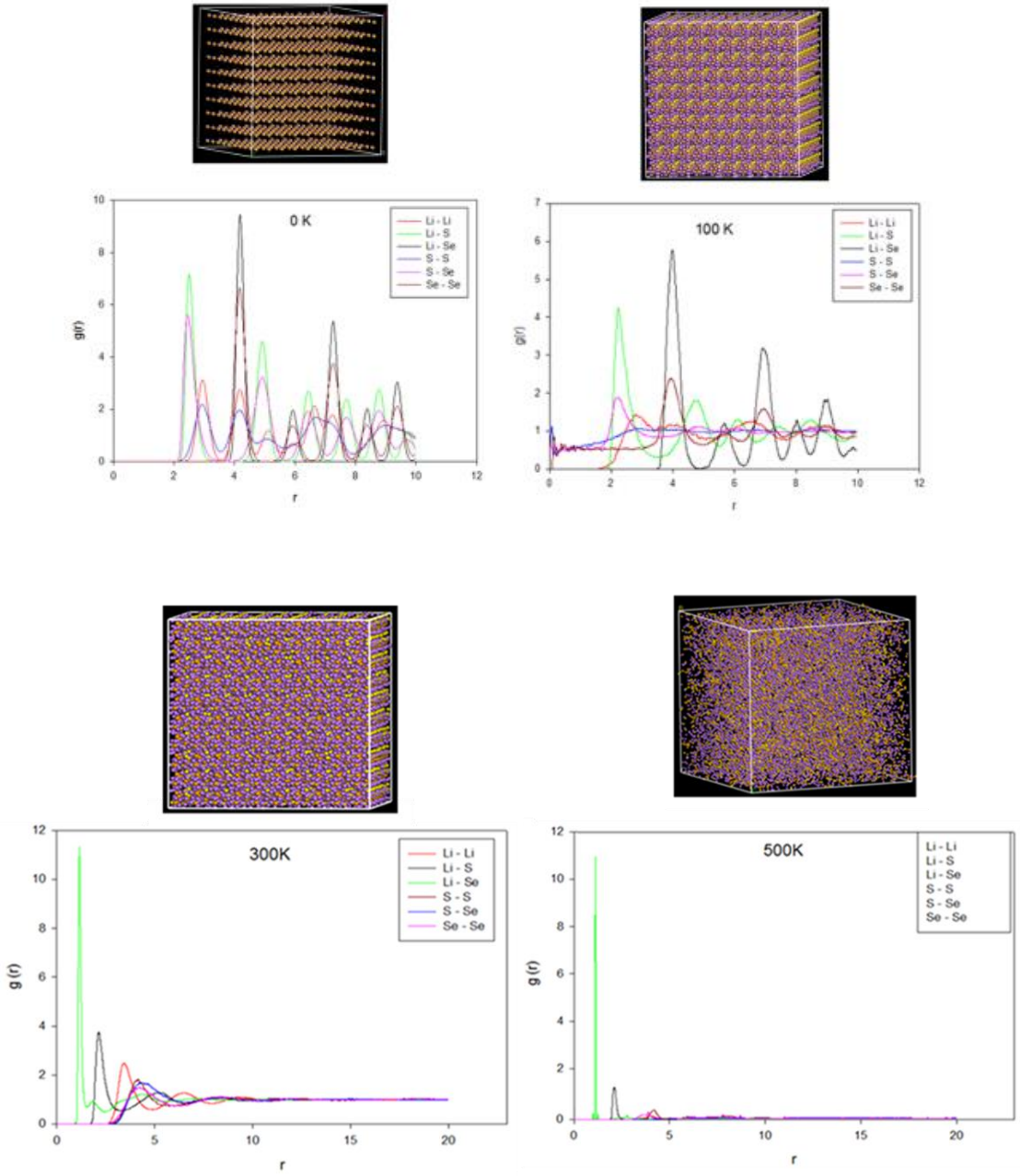

Figure 53 : Radial distribution functions of the Li_2-$S_{0.5}Se_{0.5}$ bulk structure at different temperatures. Yellow represent sulphur and purple is selenium.

6.5. Comparison between results of Monte Carlo and Molecular Dynamics Simulations.

Molecular Dynamics calculations and Monte Carlo simulation calculation implemented within MedeA-UNCLE are in great agreement with $Li_2S_{0.5}$- $Se_{0.5}$ both showing that the system experience phase transitions at low temperatures. It has been noted that the system remains phase separating at very low temperatures both techniques

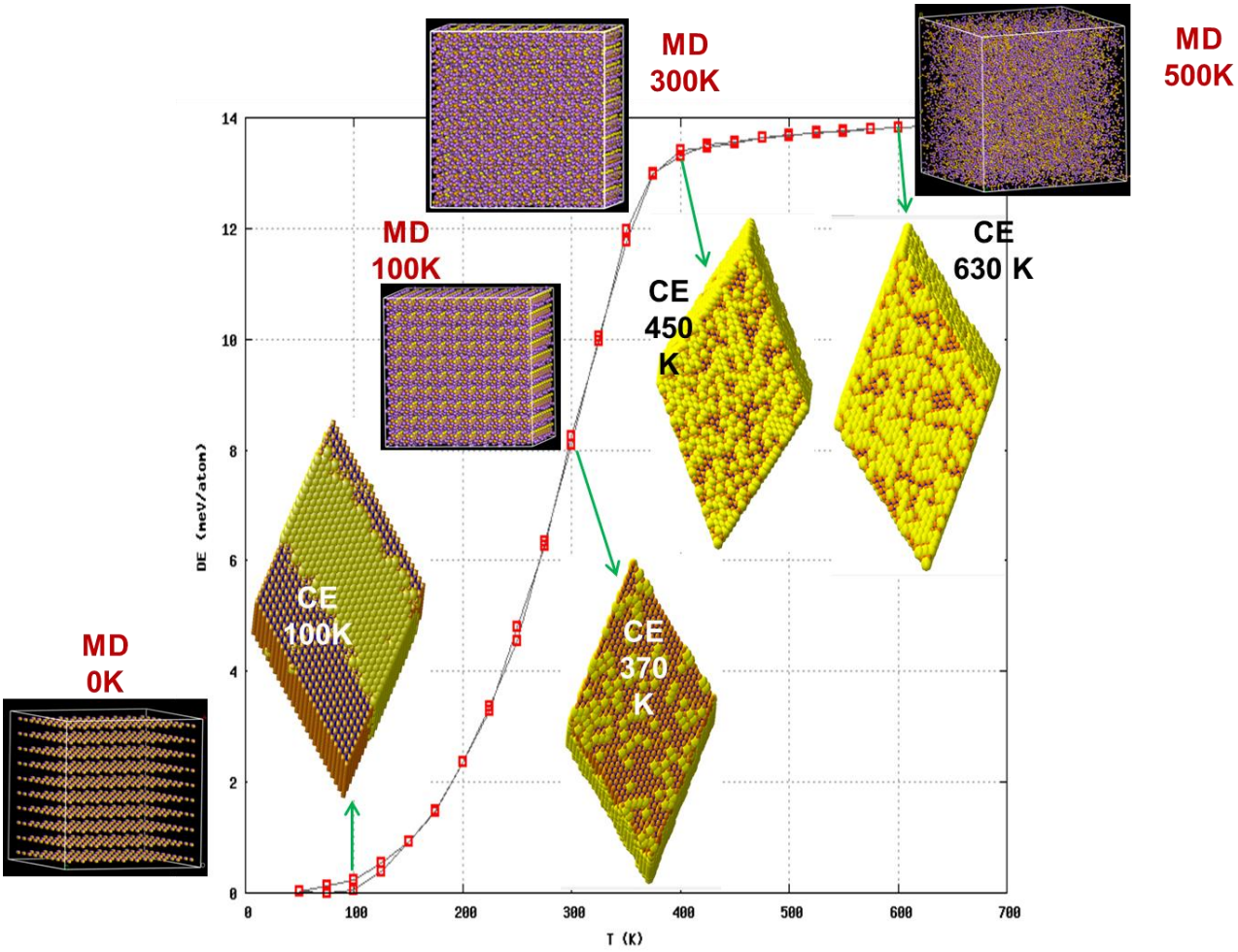

Figure 54: Comparisons of molecular dynamics and Monte Carlo simulations for $Li_2S_{0.5}Se_{0.5}$ at different temperatures.

6.6 Discussions

As mentioned in previous chapters, mixed S-Se is an attractive new class of cathode materials with promising electrochemical performance in reactions with lithium ions. Such mixture provides effective reduction of the large polysulfide formation during the cycling, normally observed in Li-S cathodes. Furthermore, battery performance is enhanced by improving the lithium ion and electron transport property and intensifying the interaction between Se and conductive matrices.

In this chapter we studied thermodynamic properties of the mixed Li-S-Se system at various temperatures, deduced from cluster expansion based Monte Carlo simulation techniques, and validated by classical molecular dynamics in the absence of experimental results. Molecular dynamics is an independent technique and associated interatomic potentials for Li-S and Li-Se were successfully derived in Chapter 4. Monte Carlo is also better suited for studying microscopic properties, such as clustering and formation of precipitates. The calculations were performed for 50% sulphur and 50% selenium, where the two independent techniques yield consistent results, clearly showing that the $Li_2S_{0.5}Se_{0.5}$ phase change occurs at a low temperature of approximately 350K by both techniques. The findings further demonstrated that selenium introduction in Li_2S reduces the melting temperature of the system from 1300K to 380 K which is a vital factor in rechargeable lithium batteries, where operation at ambient temperatures is mostly desirable.

Previous studies in binary fluorites, have clearly illustrated variations of phase change related transition temperatures when they are mixed or doped to constitute ternaries. Firstly, in mixed-cation ternaries, $Cd_xPb_{1-x}F_2$ ($0 \leqslant x \leqslant 1$), the transition temperature to a superionic phase of $Cd_{0.4}Pb_{0.6}F_2$ was reduced to 485K as compared to 600K and 1300K

for pure PbF_2 and CdF_2 respectively; a deduction from ionic conductivity and specific heat capacity investigations of Kosacki et al [143] . Furthermore, a combination of classical molecular dynamics and EXAFS experiments on mixed-cation fluorites also depicted the largest disorder at x=0.4 in $Cd_xPb_{1-x}F_2$, as shown by Netshisaulu et al. [144] . Secondly aliovalent doping of BaF_2, with a wide range of LaF_3 concentrations, was studied by a combination of both Raman and Brillouin scattering experiments as well as molecular dynamics, demonstrated by Rammutla et al. [145]. All techniques consistently attested to the transition temperature to the superionic state changing from 1200 to 950K over a concentration range of ($0 \leqslant x \leqslant 50$ mol%). Lastly, we allude to depression of the martensitic transformation temperature in shape memory alloys on formation of ternaries. A combination of semi-empirical embedded atom model molecular dynamics simulations and experimental X-ray diffractions shown by Mahlangu et al [146], indicated the reduction of the transformation temperature in $TiPt_{1-x}Co_x$ with increasing x.

Such narratives are consistent with the current reduced superionic transition and melting temperature in Li_2S-Se compounds and related changes from segregated to solid solution phases; as espoused by a combination of molecular dynamics and Monte Carlo simulations. It is of great interest that doping of fluorite ($Cd_xPb_{1-x}F_2$) and anti-fluorite ($Li_2S_{0.5}Se_{0.5}$) compounds with elements of equivalent charge depress the transition temperatures most significantly, as compared to aliovalent doping.

Monte Carlo simulation was performed by Ravi *et al.* [147] for computing the finite temperature formation enthalpies of these phases on V_2N-Fe. Phase stability of stable and metastable vanadium nitrides was studied using density functional theory DFT

based total-energy calculations combined with cluster expansion Monte Carlo simulation and supercell methods.

Computed formation enthalpies of the various stable and metastable vanadium nitride phases considering the available structural models and found that the formation enthalpies of the different phases decrease in the same order as they appear in the experimental aging sequence. As these nitrides are known to be generally nonstoichiometric due to presence of nitrogen vacancies, cluster expansion and supercell methods were used for examining the effect of nitrogen vacancies on the phase stability. Monte Carlo simulations were used for computing the finite temperature formation enthalpies of these phases as a function of nitrogen-vacancy concentration and found close agreement for NaCl_B1 phase of $VN_{1-x}Fe_x$ for which measured values are available. All such examples illustrate that a combination of cluster expansion and Monte Carlo simulation can yield reliable results in the absence of experimental results, as is the case for Li-S-Se systems.

Currently there is not much experimental evidence on phase diagrams involving a combination of Li_2S and Li_2Se, and in this chapter two separate simulation methods have been employed to predict similar phenomena. Consequently, results of calculations from classical molecular dynamics simulations based on Born Meyer interatomic potential models (from chapter 4) have been used to validate those from a combination of cluster expansion and Monte Carlo simulations (chapter 5) for $Li_2S_{0.5}Se_{0.5}$. Such validation will provide valuable insights which will guide experiments on where phase separation and mixed phases on such a system tend to occur.

Chapter 7

7.1. Conclusions

Lithium–sulphur (Li–S) batteries have regained increasing interest since the concept emerged in the 1960s, due to their high specific capacity (1675 mAh /g) and natural abundance of sulphur. However, sulphur -based cathodes face the problems of insulating properties and the dissolution of polysulfide intermediates, which lead to the low electrochemical utilization of sulphur and fast capacity fading. Many efforts and significant achievements have been made over the last few years to solve these problems. The approach commonly adopted is immobilizing sulphur in various materials to provide conductivity and alleviate the dissolution phenomenon.

We initially started by investigating the discharge products formed in Li-S and Li-O batteries which are Li_2S, Li_2O, Li_2O_2 and Li_2S_2 structures. The equilibrium lattice parameters of the Li_2S, Li_2O, Li_2O_2 and Li_2S_2 structures were performed within the generalised gradient approximations. Since the structure of Li_2S_2 is unknown, we deduced it from that of Li_2O_2, as both Li_2S and Li_2O have an anti-fluorite structure. On the whole the results were in reasonable agreement with the available experimental values. We have also calculated the electronic and elastic properties of Li_2S, Li_2O, Li_2O_2 and Li_2S_2 structures and they were mostly consistent with experimental studies. We found that Li_2S, Li_2O and Li_2O_2 and Li_2S_2 structures all have negative heats of formations values indicating that they are stable. However, it is noted that Li_2S_2 structure has negative heats of formation closer to zero, suggesting that it could be less stable compared to others. Furthermore, the calculations on the phonon dispersion and the density of states were performed and they confirm the stability of Li_2S, Li_2O and

Li_2O_2 structures, since no soft modes were observed, and consistent with the stability conditions of elastic properties. The phonon dispersion curves of the Li_2S_2 structure showed the presence of soft modes which are partly associated with the negative elastic constant C_{13} of the structure. We also performed phonon density of states for Li_2S_2 structure to check which between lithium and sulphur is responsible for instability of the structure, we have found out that the instability of Li_2S_2 structure is due to high vibrations of sulphur atoms.

We further extracted other polymorphs of Li_2S_2 structure from phonon dispersions curves of unstable Li_2S_2 structure and managed to predict stable new polymorphs of Li_2S_2 structure from heats of formation, elastic properties and phonon dispersion curves. Finally we calculated electronic density of states to check whether studied compounds are semi-conductors, metals or insulators**.** Density of states depicts that of all discharge products are metal, semi-conductors or insulators, Li_2O and Li_2S are called insulators, whereas Li_2O_2 and Li_2S_2 they are preferably called semi- conductors.

A new class of selenium and selenium−sulphur (Se_xS_y)-based cathode materials for room temperature lithium batteries is being considered as reported recently by Amine *et al* [148]. Not only does the Se electrode show promising electrochemical performance with Li anode, but the additional potential for mixed Se_xS_y systems allows for tunable electrodes, combining the high capacities of S-rich systems with the high electrical conductivity of the d-electron containing Se without failure and alleviating the dissolution phenomenon in the processes.

In order to provide the solution on Li_2S-Se system, classical simulation studies were first conducted. Interatomic potentials of Li_2S and Li_2Se were derived and adequately

validated, in the bulk form, as evidenced by their accurate determination of structure, elastic constants and moduli; which indeed compare well with to those obtained by experiment or *ab initio* methods [149]. The robustness of the interatomic potentials was further illustrated by their ability to reproduce complex high temperature transitions of the bulk Li_2S and Li_2Se which were observed experimentally, from neutron and Brilluion scattering methods [123] and from recent quantum mechanical molecular dynamics calculations of Li_2S [125]. The change of radial distribution functions and the total energy with temperature, deduced from molecular dynamics studies, clearly depicted the phase change from the normal to the high form for both Li_2S and Li_2Se above 1200K. Furthermore, the potentials of both Li_2S and Li_2Se show melting above 1300K, as demonstrated by the calculated rdfs and energy; all consistent with the experimental results.

Secondly, cluster expansion methods were employed to generate 42 new stable phases from a binary phase diagram. The new phases generated depict a miscibility gap owing to their phase separating behaviour. The Monte Carlo simulation technique was utilized to investigate thermodynamical properties of Li_2S-Se system for the entire range of Se concentrations. It was found that the system remains phase separating at 0K and a mixture occurs around 350K. Our results prove the usefulness and the suitability of a combined cluster expansion and Monte Carlo approach for studying phase transformations and thermodynamical properties occurring in Li_2S-Se system. We constructed a phase diagram from MC simulations results to show how Li_2S-Se changes phases with temperature and it was found to, in general, be consistent with the available experimental work of both Li_2S and Li_2Se.

Lastly not much experimental work is available on Li_2S-Se systems. Hence a major contribution of the current study is employing an approach involving combined molecular dynamics and Monte Carlo techniques to study associated phase separating behaviour of Li_2S-Se. The calculations were performed for 50% sulphur and 50% selenium and both methods predict Li_2S-Se phase change at a low temperatures of 350K. Such validation will provide valuable insights which will guide experiments on where phase separation and mixed phases tend to occur in Li_2S-Se systems, over an entire range of sulphur and selenium contents.

7.2. Recommendations

In light of the findings of this thesis, several recommendations for future research are listed below:

- Use molecular-dynamics calculations to study the amorphization and recrystallization (A+R) of Li_2S and Li_2Se structures utilizing the fitted interatomic potential models.
- Generate nano-architectures and related microstructures from A+R.
- Study molecular dynamics using *ab initio* methods to validate the atomistic molecular dynamics findings.
- The refitting or refinement of our potential model used in this thesis, to be able to handle the bulk structure of Li_2S and Li_2Se very “well”, such as incorporation of the shell model in the potentials.
- A further study on diffusivity using MedeA-UNCLE code.

References

[1] H. Vikstrom, S. Davidsson and M. Höök, “Lithium availability and future production outlooks,” *Appl. Energy,* vol. 110, p. 252, 2013.

[2] T. Nagaura and K. Tozawa, “Lithium ion rechargeable battery,” *Prog. Batteries Sol. Cells,* vol. 9, p. 209, 1990.

[3] J. M. Tarascon and M. Armand, “Issues and challenges facing rechargeable lithium batteries,” *Nature,* vol. 414, p. 359, 2001.

[4] GA. Nazri and G. Pistoia, “Lithium Batteries: Science and Technology,” *Springer,* 2003.

[5] W. Schalkwijk and B. Scrosati, “Advances in Lithium-Ion Batteries.,” *Kluwer Academic/Plenum,* 2002.

[6] S. Pacala and R. Socolow, “Stabilization Wedges: Solving the Climate Problem for the Next 50 Years with Current Technologies,” *Science,* vol. 305 , p. 968, 2004.

[7] PG. Bruce, “Energy storage beyond the horizon: Rechargeable lithium batteries.,” *Solid State Ionics,* vol. 179, p. 752, 2008.

[8] PG. Bruce, LJ. Hardwick and KM. Abraham, “Lithium-air and lithium-sulfur batteries.,” *Mater. Res. Soc. Bull.,* vol. 36, p. 506, 2011.

[9] “Encyclopedia of Electrochemical Power Sources,” *Elsevier,* 2009.

[10] JS. Lee, “Metal–air batteries with high energy density: Li–air versus Zn–air.,” *Adv. Energy Mater.,* vol. 1, p. 34, 2011.

[11] V. Neburchilov, HJ. Wang, JJ. Martin and W. Qu, “A review on air cathodes for zinc-air fuel cells.,” *J. Power Sources,* vol. 195, p. 1271, 2010.

[12] D. Herbert and J. Ulam, “Electric dry cells and storage batteries,” *US patent 3,043,896,* p. 1962.

[13] Abraham, K. M. & Jiang, Z., “A polymer electrolyte-based rechargeable lithium/ oxygen battery.,” *J. Electrochem. Soc. ,* vol. 143, p. 1, 1996.

[14] A. Kraytsberg and Y. Ein-Eli, “Review on Li–air batteries—opportunities, limitations and perspective.,” *J. Power Sources,* vol. 196, p. 886, 2010.

[15] EL. Littauer and KC. Tsai, “Anodic behavior of lithium in aqueous-electrolytes,” *J. Electrochem. Soc.,* vol. 123, p. 771, 1976.

[16] J. M. Tarascon, “Key challenges in future Li-battery research,” *Philos. Trans. R. Soc. London, Ser. A,* vol. 368, p. 3227, 2010.

[17] K. M. Abraham and Z. Jiang, “A polymer electrolyte-based rechargeable lithium/oxygen battery,” *J. Electrochem. Soc.,* vol. 143, p. 1, 1996.

[18] A. Abouimrane, D. Dambournet,K. W. Chapman, P.J. Chupas, W.Weng and K. Amine, “New Class of Lithium and Sodium Rechargeable Batteries Based on Selenium and Selenium−Sulfur as a Positive Electrode,” *J. Am. Chem. Soc. ,* vol. 134, p. 4505, 2012.

[19] X. Li, J. Liang, K. Zhang, Z. Hou, W. Zhang, Y. Zhu and Y. Qian, “Amorphous S-rich SxSex/C composites promise better lithium–sulfur batteries in a carbonate-based electrolyte,” *Energy Environ. Sci.,* vol. 8, p. 3181, 2015.

[20] PG. Bruce, SA. Freunberger, LJ. Hardwick and JM. Tarascon, “Li–O2 and Li–S batteries with high energy storage,” *Nature,* vol. 11, p. 19, 2012.

[21] B. Bertheville, H. Bill and H. Hagemann, “Experimental Raman scattering investigation of phonon anharmocity effects in Li_2S,” *J. Phys.: Condens. Matter,* vol. 10, p. 2155, 1998.

[22] E. Ruckenstein and Y.H. Hu, “High effective Li_2O/ Li_3N with ultrafast kinetics for H_2 storage,,” *Ind. Eng. Chem. Res.,* vol. 43, p. 2464, 2004.

[23] Y. Duan and DC. Sorescu, “Density functional theory studies of the structural, electronic, and phonon properties of Li_2O and Li_2CO_3: Application to CO2 capture reaction,” *Phys. Rev. B,* vol. 79, p. 014301, 2009.

[24] L. G. Cota and P. de la Mora, “On the structure of lithium peroxide,” *Acta Cryst. B,* vol. 61, p. 133, 2005.

[25] KY. Chan,EL. Shirley,K. Karan, M. Balasubramanian, Y. Ren, JP. Greeley and TT. Fister, “Structure of Lithium Peroxide,” *J. Phys. Chem. Lett.,* vol. 2, p. 2483, 2011.

[26] F. Fe´her, I. von Wilucki and G. Dost, “Structure of Lithium Peroxide,” *J. Phys. Chem. Lett.,* vol. 86, no. 1953, p. 2483, 2011.

[27] H. Fo¨ppl, “On the structure of lithium peroxide,” *Acta Cryst. B,* vol. 291, p. 133, 1957.

[28] P. Goel, N. Choudhury and S.L. Chaplot, “Superionic behavior of lithium oxide: A lattice dynamics and moleculer dynamics,” *Phys. Rev. B,* vol. 70, p. 174307, 2004.

[29] S Chandra, “Superionic Solids; Principles and Applications,” *North Holland,* p. 20, 1981.

[30] W Hayes and M T Hutchings, “Ionic Solids at High Temperatures,” *Edition A M Stoneham,* p. 247, 1989.

[31] B. Bertheville, H. Bill and H. Hagemann, “Experimental Raman scattering investigation of phonon anharmocity effects in Li_2S,” *J. Phys.: Condens. Matter,* vol. 10, p. 2155, 1998.

[32] A.K. Koh, “Systematic Variation between Cohesive Energy and a Lattice Ratio in Alkali Chalcogenide Crystals,” *Phys. Stat. Sol.* , vol. 210, p. 31, 1999.

[33] V.K. Jain and J. Shanker, “Relative Stability and Structural Phase Transitions in Alkaline Earth Chalcogenide Crystals,” *Phys. Stat. Sol.,* vol. 111, p. 519, 1982.

[34] R.D. Eighitaj, G. Jaiganesh and G. Kalpana, “First principles study of electronic structure and ground state of alkali metal selenides and tellurides,” *Int. J. Mod. Phys. B,* vol. 23, p. 5027, 2009.

[35] P M Mjwara, J D Comins, P E Ngoepe, W Buhrer and H Bill, “Brillouin scattering investigation of the high temperature diffuse phase transition in Li_2S,” *J. Phys.: Condens. Matter,* vol. 3, p. 4289, 1992.

[36] SF. Pugh, “Relations between the elastic moduli and the plastic properties of polycrystalline pure metals,” *Phil. Magazine,* vol. 45, p. 823, 1954.

[37] S. Kazanc and S. Ozgen, “An Investigation of Temperature Effect on Phonon Dispersion Spectra of Ni by Molecular Dynamics Simulation,” *Turk. J. Phys,* vol. 32, p. 315 , 2008.

[38] AA. Klein and BM. Quong , “Linear-response calculation of electron-phonon coupling parameters,” *Phys. Rev. B,* vol. 53, p. R7575, 1996.

[39] P. Palacios, P. Wahnon and C. Tablero, “Ab initio phonon dispersion calculations for TixGanAsm and TixGanPm compounds,” *Comp. Mat. Science,* vol. 33, p. 118, 2005.

[40] P. Gironcoli and S. Giannozzi, “Ab initio calculation of phonon dispersions in semiconductors,” *Phys. Rev. B,* vol. 43, p. 7231, 1991.

[41] S. Shabalovskaya, A. Narmonev, O. Ivanova and A. Dementjev, “Electronic structure and stability of Ti-based B2 shape-memory compounds: X-ray and ultraviolet photoelectron spectra,” *Phys. Rev. B,* vol. 48, p. 13296, 1993.

[42] M. Sundareswari and M. Rajagopalan, “Ab initio study of the electronic structure of rhodium based intermetallic compounds under pressure,” *J. Alloys and Comp.,* vol. 379, p. 8, 2004.

[43] S. Ghosh, “Ab initio calculation of lattice dynamics in FePd intermetallics,” *J. Phys. Condens. Matter,* vol. 20, p. 275208 , 2008.

[44] S. Müller, “Bulk and Surface Ordering Phenomena in Binary Metal Alloys,” *J. Phys: Condens. Matter,* vol. 34, p. R1429, 2003.

[45] C. Ravi, H. K. Sahu, and M. C. Valsakumar, “Cluster expansion Monte Carlo study of phase stability of vanadium nitrides,” *Phys. Rev. B,* vol. 81, p. 104111, 2010.

[46] M. Yu. Lavrenti R. Drautz, D. Nguyen-Manh, T. P. C. Klaver, and S. L. Dudarev, “Monte Carlo study of thermodynamic properties and clustering in the bcc Fe-Cr system,” *Phys.Rev. B,* vol. 75, p. 014208, 2007.

[47] K.J. W. Atkinson , Atomic scale simulation of defects in bulk materials and monolayer surfaces, PhD Thesis, University of London, 2002.

[48] M. Matsui and M. Akaogi, “Molecular dynamics simulation of the structural and physical properties of the four polymorphs of TiO_2,” *Mol. Simul,* vol. 6, p. 244, 1991.

[49] N. H. de Leeuw, S. C. Parker, H. M. Sithole, and P. E. Ngoepe, “Modeling the surface structure and reactivity of pyrite: Introducing a Potential Model for FeS_2,” *J. Phys. Chem. B,* vol. 104, p. 7976, 2000.

[50] S.D. Fleming, J.R. Morton, A.L. Rohl and C.B. Ward, “Interatomic potentials for simulating MnO2 polymorphs,” *Mol. Simul.,* vol. 31, p. 32, 2005.

[51] M.C. Payne, M.P. Teter, D.C. Allan, T.A. Ariar and J.D. Joannopoulos, “Iterative minimization techniques for ab initio total-energy calculations: molecular dynamics and conjugate gradients,” *Rev. Mod. Phys,* vol. 64, p. 1045, 1992.

[52] A. Jayaraman, “Diamond anvil cell and high-pressure physical investigations,” *Rev. Mod. Phys.,* vol. 55, p. 65, 1983.

[53] M.R. Levy , “ Crystal structure and defect property predictions in ceramic materials,” University Of London, PhD Thesis, 2005., 2005.

[54] E. Wimmer, “The growing importance of computations in materials science: Current capabilities and perspectives,” *Mat. Science,* vol. 23, p. 325, 2005.

[55] W. Kohn and P. Hohenberg, “Inhomogeneous Electron Gas,” *Phys. Rev. B,* vol. 136, p. B864, 1964.

[56] E. Fermi, “Quantum Theory of Radiation,” *Rev. Mod. Phys.* , vol. 4, p. 87, 19832.

[57] DR. Hartree, “The Wave Mechanics of an Atom with a Non-Coulomb Central Field. Part I. Theory and Methods,” *Proc. Camb. Phil. Soc.,* vol. 24, pp. 89-110, 1928.

[58] JC. Slater, “A Generalized Self-Consistent Field Method,” *Phys. Rev. B,* vol. 81, p. 385, 1951.

[59] DM. Alder and BJ. Ceperley, “Ground State of the Electron Gas by a Stochastic Method,” *Phys. Rev. Lett.,* vol. 45, p. 566, 1980.

[60] JP. Perdew, “Density-functional approximation for the correlation energy of the inhomogeneous electron gas,” *Phys. Rev. B,* vol. 33, p. 8822, 1986.

[61] AD. Becke, “Density-functional exchange-energy approximation with correct asymptotic behavior,” *Phys. Rev. A,* vol. 38, p. 3098, 1988.

[62] Y. Wang and J.P. Perdew, “Accurate and simple analytic representation of the electron-gas correlation energy,” *Phys. Rev. B,* vol. 45, p. 13244, 1992.

[63] J.P. Perdew, K. Burke and M. Ernzerhof, “Generalized Gradient Approximation Made Simple,” *Phys. Rev. Lett.* , vol. 77, p. 3865, 1996.

[64] E. Wimmer and J. Andzelm , “Density functional Gaussian-type-orbital approach to molecular geometries, vibrations, and reaction energies,” *J. Chem. Phys.,* vol. 96, p. 1280, 1992.

[65] J.C. Philips, “Energy-Band Interpolation Scheme Based on a Pseudopotential,” *Phys. Rev.* , vol. 112, p. 685, 1958.

[66] M. T. Yin and M. L. Cohen, “Theory of ab initio pseudopotential calculations,” *Phys. Rev. B* , vol. 25, p. 7403, 1982.

[67] D. J. Chadi and M.L. Cohen, “Special Points in the Brillouin Zone,” *Phys. Rev. B* , vol. 8, p. 5747, 1973.

[68] H.J. Monkhorst and J. D. Pack, “Special points for Brillouin-zone integrations,” *Phys. Rev. B* , vol. 13, p. 5188, 1976.

[69] G. Kresse, J. Furthmüller and J. Hafner, “Theory of the crystal structures of selenium and tellurium: The effect of generalized-gradient corrections to the local-density approximation,” *Phys. Rev. B,* vol. 50, p. 13181, 1994.

[70] P. E. Blöchl, “Projector augmented-wave method,” *Phys. Rev. B,* vol. 50, p. 17953, 1994.

[71] M.J. Mehl, B.M. Klein and D.A. Papaconstantopoulos, “Intermetallic Compounds, Principles. Edited by J.H. Westbrook and R.L. Fleischer,” 1994.

[72] L.L Boyer and M.J. Mehl, “Getting off the Bain path: Are there any metastable states of cubic elements?,” *Phys. Rev. B,* vol. 43, p. 9498 , 1991.

[73] P. Saxe and Y. Le Page, “Ab initio vs literature stiffness values for Ga: a caveat about crystal settings,” *Physica B,* vol. 63, p. 191, 2001.

[74] H. Chauke, “The first principle approach energrtics and phase stability modelling of $PtPt_3$,” *PhD Thesis, University of Limpopo,* 2005.

[75] A. Rahman, “Correlations in the Motions of Atoms in Liquid Argon.,” *Phys. Rev. B,* vol. 136, p. 405, 1964.

[76] R. M. Martin and K. Kunc, “Ab Initio Force Constants of GaAs: A New Approach to Calculation of Phonons and Dielectric Properties,” *Phys. Rev. Lett.,* vol. 48, p. 406, 1982.

[77] W. Frank, C. Elsässer and M. Fähnle, “Ab initio Force-Constant Method for Phonon Dispersions in Alkali Metals,” *Phys. Rev. Lett.,* vol. 74, p. 1791, 1995.

[78] GJ. Ackland, “Embrittlement and the bistable crystal structure of zirconium hydride,” *Phys .Rev. Letters,* vol. 80, p. 2233, 1998.

[79] C.R.A Catlow, “Computer modelling as a technique in solid state chemistry,” *Faraday Discussion,* vol. 106, p. 1, 1997.

[80] N.H. de Leeuw and S.C. Parker, “Molecular-dynamics simulation of MgO surfaces in liquid water using a shell-model potential for water,” *Phys. Rev. B,* vol. 58, p. 13901, 1998.

[81] S.C. Parker, N.H. de Leeuw and S.E. Redfern, “ Atomistic simulation of oxide surfaces and their reactivity with water,” *Faraday Discussion,* vol. 114, p. 381, 1999.

[82] M. Born and K. Huang , “Dynamical Theory of Crystal Lattices 1st edition,” University Press, Oxford, 1954.

[83] D.K. Fisler, J.D. Gale and R.T.A. Cygan, “Shell model for the simulation of rhombohedral carbonate minerals and their point defects,” *Am. Mineralogist,* vol. 85, p. 217, 2000.

[84] G.W. Watson, E. T. Kelsey, N. H. de Leeuw, D. J. Harris and S. C. Parker, “Atomistic simulation of dislocations, surfaces and interfaces in MgO,” *J. Chem. Soc. Faraday Trans.,* vol. 92, p. 433, 1996.

[85] S. Kerisit, “ Atomistic simulation of calcite surfaces,” University of Bath, PhD Thesis, 2004.

[86] M.J. Norgett and R Fletcher, “Fast matrix methods for calculating relaxation about defects in crystals.,” *J. Phys. Part C: Solid State Phys.,* vol. 3, p. L190, 1970.

[87] R. Fletcher and M.J.D. Powell, “A rapidly convergent descent method for minimization,” *Comp. J.,* vol. 6, p. 163, 1963.

[88] D. Goldfarb, “A family of variable-metric methods derived by variational means.,” *Math. Comp.,* vol. 24, p. 23, 1970.

[89] D.F. Shanno, “Conditioning of quasi-Newton methods for function minimization,” *Math. Comp.,* vol. 24, p. 647, 1970.

[90] H.Z. Zhang and J.F. Banfield, “Aggregation, coarsening, and phase transformation in ZnS nanoparticles studied by molecular dynamics simulations,” *Nano Lett.,* vol. 4, p. 713, 2004.

[91] D. Frenkel and B. Smit, “Understanding molecular simulations,” Algorithms to Applications Academic Press, San Diego, 1996.

[92] W. Smith and T.R. Forester, “DL_POLY_2.0: A general-purpose parallel molecular dynamics simulation package,” *J. Mol. Grap.,* vol. 14, p. 136, 1996.

[93] L. Verlet., “Computer "Experiments" on Classical Fluids. I. Thermodynamical properties of Lennard-Jones molecules,” *Phys. Rev. ,* vol. 159, p. 98, 1967.

[94] J.M. Holender, “Molecular-dynamics studies of the thermal properties of the solid and liquid fcc metals Ag, Au, Cu, and Ni using many-body interactions,” *Phys. Rev. B,* vol. 41, p. 8054, 1990.

[95] D.C. Sayle, J.A. Doig, S.A. Maicaneanu and G.W. Watson, “The atomistic structure of oxide nanoparticles supported on an oxide substrate,” *Phys. Rev. B,* vol. 65, p. 245414, 2002.

[96] W. Kob, “Computer simulations of supercooled liquids and glasses,” *J. Phys.: Condens. Matter,* vol. 11, p. 85, 1999.

[97] P.M. Oliver, G.W. Watson and S.C. Parker, “Molecular dynamics simulations of nickel oxide surfaces,” *Phys. Rev. B,* vol. 52, p. 5323, 1995.

[98] G. Kresse, J. Furthmüller and J. Hafner, “Theory of the crystal structures of selenium and tellurium: The effect of generalized-gradient corrections to the local-density approximation,” *Phys. Rev. B,* vol. 50, p. 13181, 1994.

[99] D. Vanderbilt, “Soft self-consistent pseudopotentials in a generalized eigenvalue formalism,” *Phys. Rev. B,* vol. 41, p. 7892, 1990.

[100] M. Wilson, S. Jahn and P.A Madden, “The construction and application of a fully flexible computer simulation model for lithium oxide,” *J. Phys.: Condens. Matter,* vol. 16, p. S2795, 2004.

[101] C.R.A Catlow, J.D. Gale and R.W.Grimes, “Recent computational studies in solid state chemistry,” *J. Solid State Chem.,* vol. 106, p. 13, 1993.

[102] M. Born and K. Huang, Dynamical Theory of Crystal Lattices 1st edition, University Press: Oxford, 1954.

[103] J.W. Gibbs, The collected works, volume 1, Thermodynamics. Longmans & Green, New York, 1928.

[104] P.P. Ewald, “Die Berechnung optischer und elektrostatischer Gitterpotential,” *Ann. Physik,* vol. 64, p. 440, 1921.

[105] D.E. Parry, “The electrostatic potential in the surface region of an ionic crystal,” *Surface Science,* vol. 49, p. 440, 1975.

[106] D.M. Heyes, M. Barber and J.H.R. Clarke., “Molecular dynamics computer simulation of surface properties of crystalline potassium chloride,” *J. Chem. Soc. Faraday Trans.,* vol. 73, p. 1496, 1977.

[107] A.W Dick, and B.G. Overhauser, “Theory of dielectric constants of alkali halide crystals,” *Phys. Rev.,* vol. 112, p. 103, 1958.

[108] C.R.A. Catlow, "New science from high-performance computing: an introduction," *Phil. Trans. Royal Soc.: London A,* vol. 360, p. 1078, 2002.

[109] M.D. Segall, P. J.D. Lindan, M.J. Probert, C.J. Pickard, P.J. Hasnip, S.J. Clark and M.C. Payne., "First-principles simulation: ideas, illustrations and the CASTEP code," *J. Phys: Condens. Matter,* vol. 14, p. 2744, 2002.

[110] J. D. Gale and A. L. Rohl, "The General Utility Lattice Program (GULP)," *Mol. Simul.,* vol. 5, p. 341, 2003.

[111] C.A.J. Fisher, "Molecular dynamics simulations of reconstructed NiO surfaces," *Scripta Mat.,* vol. 50, p. 1049, 2004.

[112] P. Pandit, B. Rakshit and S.P . Sanyal, "Electronic and elastic properties of alkali-metals sulphides - Li_2S and Na_2S," *Ind. J. Pure Applied Phys.,* vol. 47, p. 804, 2009.

[113] R.D. Eithiraj, G. Jaiganesh, G. Kalpana and M. Rajagopalan, "First-principles study of electronic structure and ground-state properties of alkali-metal sulfides – Li_2S, Na_2S, K2S and Rb_2S," *Phys. Status Solidi B,* vol. 244, p. 1337, 2007.

[114] X Zhang, C Ying, G Shi, Z Li and H Shi, "A first-principles study on lattice dynamics, thermodynamics and elastic properties of lithium selenide under high pressure," *J. Comp. Mat. Science,* vol. 79, p. 903, 2013.

[115] S.M. Alay-e-Abbas, N. Sabir, Y. Saeed and A. Shaukat, "Electronic and optical properties of alkali metal selenides in anti-CaF2 crystal structure from first-principles," *J. Alloy Comp.,* vol. 10, p. 503, 2010.

[116] F. Wu, JT. Lee, Y. Xiao and G. Yushin, "Nanostructured Li2Se cathodes for high perfomance Li-Se batteries," *Nano Energy,* vol. 27, p. 238, 2016.

[117] P. Pandit, B. Rakshit and S. Senyal, "Electronic and elastic properties of alkali-metal sulphides-Li_2S and Na_2S," *Ind. J. Pure Applied Phys.,* vol. 47, p. 807, 2009.

[118] M.I. Mendelev and G.J. Ackland, "Development of an interatomic potential for the simulation of phase transformations in zirconium.," *Phil. Mag. Lett.,* vol. 87, p. 349, 2007.

[119] H. Chiba, K. Nishidate, M. Baba, N. Kumagai, T. Sato and K. Nishikawa, "Molecular dynamics study of a V_2O_5 crystal.," *Solid State Comm.,* vol. 110, p. 497, 1999.

[120] W. Chen, C. Wua and H. Cheng, "Modified Nosé–Hoover thermostat for solid state for constant temperature molecular dynamics simulation," *J. Comp. Phys,* vol. 230, p. 6354, 2011.

[121] P M Mjwara, J D Comins, PE Ngoepe, W Biihrers and H Bill, "Brillouin scattering investigation of the high temperature diffuse phase transition in Li_2S," *J. Phys.: Condens. Matter,* vol. 3, p. 4289, 1991.

[122] W Buehrer, F Altorfert, J Mesott, H Bill, P Carroni and H G Smiths, "Lattice dynamics and the diffuse phase transition of lithium sulphide investigated by coherent neutron scattering," *Phys.: Condens. Matter,* vol. 3, p. 1055, 1991.

[123] P M Mjwara, J D Comins, P E Ngoepe, W Buhrer and H Bill, "Brillouin scattering investigation of the high temperature diffuse phase transition in Li_2S," *J. Phys.: Condens. Matter,* vol. 3, p. 4289, 1992.

[124] B Bertheville, H Bill and H Hagemann, “Experimental Raman scattering investigation of phonon anharmonicity effects in Li_2S,” *J. Phys.: Condens. Matter,* vol. 10, p. 2155, 1998.

[125] S P Jand, Q Zhang and P Kaghazchi, “Theoretical study of superionic phase transition in Li2S,” *Sci. Reports,* vol. 7, p. 5873, 2017.

[126] H.Z. Zhang and J.F. Banfield, “Aggregation, coarsening, and phase transformation in ZnS nanoparticles studied by molecular dynamics simulations,” *Nano Lett.,* vol. 4, p. 713, 2004.

[127] J. M. Sanchez, F. Ducastelle, and D. Gratias,, “Generalized cluster description of multicomponent systems,” *Physica A: Statistical and Theoretical Physics,* vol. 128, p. 334, 1984.

[128] A. Mark, D. de Fontaine, M. van Schilfgaarde, M. Sluiter and M. Methfessel, “First-principles phase-stability study of fcc alloys in the Ti-Al system,” *Phys. Rev. B,* vol. 46, p. 5055, 1992.

[129] C. Colinet, A. Pasturel, D. Nguyen Manh, D. G. Pettifor, and P. Miodownik, “Phase stability study of the Al-Nb system,” *Phys. Rev. B,* vol. 56, p. 552, 1997.

[130] M. Asta, R. McCormack, and D. de Fontaine, “Theoretical study of alloy phase stability in the Cd-Mg system,” *Phys. Rev. B,* vol. 48, p. 748, 1993.

[131] D. Lerch, O. Wiekhorst, G. L. W. Hart, R. W. Forcade, and S. Muller, “UNCLE: a code for constructing cluster expansions for arbitrary lattices with minimal user-input,” *Modelling Simul. Mater. Sci. Eng.,* vol. 17, p. 330, 2009.

[132] G. L. W. Hart, V. Blum, M. J. Walorski, and A. Zunger, “Evolutionary approach for determining first-principles hamiltonians,” *Nature Mat.,* vol. 4, p. 391, 2005.

[133] D. Reith, M. St¨ohr, and R. Podloucky, “First-principles modeling of temperature- and concentration-dependent solubility in the phase-separating alloy Fe_xCu_{1-x},” *Phys. Rev. B,* vol. 86, p. 020201(R), 2012.

[134] G. D. Garbulsky and G. Ceder, “Effect of lattice vibrations on the ordering tendencies in substitutional binary alloys,” *Phys. Rev. B,* vol. 49, p. 6327, 1994.

[135] A. Guinier, “Heterogeneities in Solid Solutions,” *Solid State Phys.,* vol. 9, p. 293, 1959.

[136] J.B. Cohen, “The Internal Structure of Guinier-Preston Zones in Alloys,” *Solid State Phys.,* vol. 39, p. 131, 1986.

[137] H.W Zandberger, S.J Andersen and J. Jansen, “Structure Determination of Mg_5Si_6 Particles in Al by Dynamic Electron Diffraction Studies,” *Science,* vol. 277, p. 1221, 1997.

[138] P. T. Cunningham, S. A. Johnson, and E. J. Cairns, “Phase Equilibria in Lithium-Chalcogen Systems,” *J. Electrochem. Soc.,* vol. 119, p. 1450, 1972.

[139] P. T. Cunningham, S. A. Johnson, and E. J. Cairns, “Phase Equilibria in Lithium-Chalcogen Systems,” *J. Electrochem. Soc,* vol. 118, p. 1942, 1971.

[140] P. T. Cunningham, S. A. Johnson, and E. J. Cairns, “Phase Equilibria in Lithium-Chalcogen Systems,” *J. Electrochem. Soc.,* vol. 119, p. 1450, 1972.

[141] M.Cuong Nguyen, X. Zhao, C.Wang, and K. Ho, “Cluster expansion modeling and Monte Carlo simulation of alnico 5–7 permanent magnets,” *J. Applied Phys.,* vol. 117, p. 093905, 2015.

[142] R. Chinnappan, “Phase stability of V–Ta alloy using cluster expansion and Monte Carlo techniques,” *CALPHAD:Computer Coupling of Phase Diagrams and Thermochemistry,* vol. 39, p. 33, 2012.

[143] T. S. A. L. a. M. V. I. Kosacki, “Anion disordering in Cd1−xPbxF2 superionic crystals,” *Solid State Ionics,* vol. 36, p. 227, 1989.

[144] T .T. Netshisaulu,A. V. Chadwick, P. E. Ngoepe and C. R. A. Catlow, “Spectroscopic and computer modelling studies of mixed-cation superionic fluorites,” *J. Phys.: Condens. Matter,* vol. 17, p. 6575, 2005.

[145] K.E. Rammutla, J.D. Comins, R.M. Erasmus, T.T. Netshisaulu, P.E. Ngoepe and A.V. Chadwick, “Light scattering and computer simulation studies of superionic pure and La-doped BaF2,” *Chemical Physics,* vol. 467, p. 6, 2016.

[146] PM. Mashamaite,R. Mahlangu,HR. Chauke HR and PE. Ngoepe, “Temperature dependance and martinsitic transformation of TiPt shape memory alloys,” *Advanced Mat. Research,* vol. 1019, p. 379, 2014.

[147] C. Ravi, H. K. Sahu, and M. C. Valsakumar, “Cluster expansion Monte Carlo study of phase stability of vanadium nitrides,” *Phys. Rev. B,* vol. 81, p. 104111, 2010.

[148] A. Abouimrane, D. Dambournet,K. W. Chapman, P.J. Chupas, W.Weng and K. Amine, “New Class of Lithium and Sodium Rechargeable Batteries Based on Selenium and Selenium−Sulfur as a Positive Electrode,” *J. Am. Chem. Soc.,* vol. 134, p. 2012, 4505.

[149] P. Pandit, B. Rakshit and S.P . Sanyal, “Electronic and elastic properties of alkali-metals sulphides - Li_2S and Na_2S,” *Ind. J. Pure Applied Phys.,* vol. 47, p. 804, 2009.

Appendix A

Papers Presented at Local and International Conferences

1. International Battery Association Meeting, held at One and Only Hotel (Cape Town) (2011) " *ab initio* studies on stabilities of reactive products of Li-S and Li-O_2 batteries"
2. South African Institute of Physics conference held at the UNISA (Pretoria) (2011) "*ab initio* studies on stabilities of reactive products of Li-S and Li-O_2 batteries"
3. Post-graduate research day held at the University of Limpopo (2011) "First principle studies on stabilities of reactive products of Li-S and Li-O_2 batteries" **[Award for Best MSc: School of Physical & Mineral Science]**
4. CHPC National Meeting held at CSIR ICC (Pretoria) (2011) "First principle studies on stabilities of reactive products of Li-S and Li-O_2 batteries"
5. South African Institute of Physics conference held at the University of Pretoria (2012) "First Principle Study on Stabilities of Reactive Products of Sulphur and Oxygen in Lithium- and Sodium- air Batteries**.**"
6. ASSAf Third Annual South African Young Scientists' Conference held at the CSIR ICC (Pretoria) (2012) " Advanced Power Sources for Portable electronics and Electric vehicles"
7. Post-graduate research day held by University of Limpopo at Bolivia Lodge (2012) " Advanced Power Sources for Portable electronics and Electric vehicles"
8. CHPC National Meeting held at Durban ICC (2012) Advanced Power Sources for Portable electronics and Electric Vehicles"

9. South African Institute of Physics conference held at the University of Zululand (2013) “Advanced Lithium-air, Lithium-sulfur and Zinc-air Batteries: The latest status, challenges and perspectives.”
10. Post-graduate research day held by University of Limpopo at Bolivia Lodge (2013) “Metal-air Batteries: The latest status, challenges and perspectives.” **[Award for Best MSc: School of Physical & Mineral Science]**
11. CHPC National Meeting held at Cape Town ICC (2013) “Computational Study on Advanced Lithium Batteries for Portable Electronics and Electric Vehicles.”
12. South African Institute of Physics conference held at the University of Johannesburg (2014) “Advanced Lithium-Sulphur Battery for Future Energy Storage Technologies” **[Award for Best MSc: Condensed Matter Physics & Material Science]**
13. Post-graduate research day held by University of Limpopo at Bolivia Lodge (2014) “Advanced Lithium-Sulphur Battery for Future Energy Storage Technologies”
14. CHPC National Meeting held at Kruger Park (2014) “Advanced Lithium-Sulphur Battery for Future Energy Storage Technologies” **[Award for Best Research Group: Material Science and Modelling]**
15. South African Institute of Physics conference held at the NMMU/ Rhodes University (2015) “Beyond Lithium-ion Battery: A Computational Study on Lithium-Sulphur Battery ”

16. Post-graduate research day held by University of Limpopo at Bolivia Lodge (2015) “Beyond Lithium-ion Battery: A Computational Study on Lithium-Sulphur Battery ”
17. CHPC research day held by CHPC at Cape Town (2015) “Beyond Lithium-ion Battery: A Computational Study on Lithium-Sulphur Battery ”
18. CHPC National Meeting held at CSIR ICC (2015) “Beyond Lithium-ion Battery: A Computational Study on Lithium-Sulphur Battery ”
19. AYSS held at JINR (Russia) (2016) “Beyond Lithium-ion Battery: A Computational Study on Lithium-Sulphur Battery ”
20. South African Institute of Physics conference held at the University of Cape Town (2016) “Beyond Lithium-ion Battery: A Computational Study on Lithium-Sulphur Battery ” **[Award for 2nd Prize: Physics Bowl]**
21. ICDIM held at Lyon University1 (France) (2016) “Beyond Lithium-ion Battery: A Computational Study on Lithium-Sulphur Battery ”
22. Post-graduate research day held by University of Limpopo at Bolivia Lodge (2016) “Beyond Li-ion: Computational Modelling Studies on Stability of Li-S-Se System” **[Award for Best PhD: School of Physical & Mineral Science]**
23. CHPC National Meeting held at East London ICC (2015) “Beyond Li-ion: Computational Modelling Studies on Stability of Li-S-Se System”
24. South African Institute of Physics conference held at the Stellenbosch University (2017) “Beyond Lithium-ion Battery: A Computational Study on Li-S-Se system ”
25. CHPC conference held at Pretoria (2017) “Beyond Lithium-ion Battery: A Computational Study on Li-S-Se system ”

26. African Materials Research conference held at Botswana, Gaborone (2017) "Beyond Lithium-ion Battery: A Computational Study on Li-S-Se system "

Publications to be Submitted

1. "First Principle Studies on Stabilities of Reactive Products of Li-O_2 and Li-S Batteries" MC Masedi, HM Sithole and PE Ngoepe, To be submitted
2. "Atomistic Simulation Studies of Li_2S and Li_2Se; New Interatomic Potential Models", MC Masedi, HM Sithole and PE Ngoepe.
3. "Phase Diagram Prediction of Li_2-S-Se from Cluster Expansion and Monte Carlo Simulations, Validated by Classical Molecular Dynamics", MC Masedi, HM Sithole and PE Ngoepe.